



저작자표시-비영리-변경금지 2.0 대한민국

이용자는 아래의 조건을 따르는 경우에 한하여 자유롭게

- 이 저작물을 복제, 배포, 전송, 전시, 공연 및 방송할 수 있습니다.

다음과 같은 조건을 따라야 합니다:



저작자표시. 귀하는 원저작자를 표시하여야 합니다.



비영리. 귀하는 이 저작물을 영리 목적으로 이용할 수 없습니다.



변경금지. 귀하는 이 저작물을 개작, 변형 또는 가공할 수 없습니다.

- 귀하는, 이 저작물의 재이용이나 배포의 경우, 이 저작물에 적용된 이용허락조건을 명확하게 나타내어야 합니다.
- 저작권자로부터 별도의 허가를 받으면 이러한 조건들은 적용되지 않습니다.

저작권법에 따른 이용자의 권리는 위의 내용에 의하여 영향을 받지 않습니다.

이것은 [이용허락규약\(Legal Code\)](#)을 이해하기 쉽게 요약한 것입니다.

[Disclaimer](#)

공학박사 학위논문

**Dielectric Properties of $(\text{Ca}_{1-x}\text{Sr}_x)\text{Cu}_3\text{Ti}_4\text{O}_{12}$
($0 \leq x \leq 1$) Bulks and Thin Films**

$(\text{Ca}_{1-x}\text{Sr}_x)\text{Cu}_3\text{Ti}_4\text{O}_{12}$ ($0 \leq x \leq 1$)

벌크 및 박막의 유전 특성

2012년 8월

서울대학교 대학원

재료공학부

이 성 윤

Dielectric Properties of $(\text{Ca}_{1-x}\text{Sr}_x)\text{Cu}_3\text{Ti}_4\text{O}_{12}$ ($0 \leq x \leq 1$) Bulks and Thin Films

$(\text{Ca}_{1-x}\text{Sr}_x)\text{Cu}_3\text{Ti}_4\text{O}_{12}$ ($0 \leq x \leq 1$) 벌크 및 박막의 유전 특성

지도 교수 유 상 임

이 논문을 공학박사 학위논문으로 제출함
2012년 8월

서울대학교 대학원
재료공학부
이성윤

이성윤의 공학박사 학위논문을 인준함

2012년 8월

위원장 박 병 우 (인)

부위원장 유 상 임 (인)

위 원 조 월 령 (인)

위 원 김 영 환 (인)

위 원 홍 연 우 (인)

Abstract

Dielectric Properties of $(\text{Ca}_{1-x}\text{Sr}_x)\text{Cu}_3\text{Ti}_4\text{O}_{12}$ ($0 \leq x \leq 1$) Bulks and Thin Films

Sung Yun Lee

Department of Materials Science and Engineering

The Graduate School

Seoul National University

$\text{CaCu}_3\text{Ti}_4\text{O}_{12}$ (CCTO) polycrystalline ceramics ($\epsilon_r > 10,000$) have drawn a great attention of researchers due to their temperature-independent colossal dielectric response (CDR) in a wide temperature region of 100~600 K. However, the physical origins of high- k in CCTO ceramics and single crystals have been unclarified yet. In addition, a high dielectric loss ($\tan\delta$) and a large leakage current with a low breakdown voltage in CCTO are still critical drawbacks for practical applications in the capacitor industry. In this study, we first attempted to clarify the mechanisms of high- k in CCTO ceramics and single crystals. Then, we tried to clarify the electric properties of $\text{Ca}_{1-x}\text{Sr}_x\text{Cu}_3\text{Ti}_4\text{O}_{12}$ ($\text{C}_{1-x}\text{S}_x\text{CTO}$, $0 \leq x \leq 1$) ceramics since reported literatures were not in consensus. We also investigated the subsolidus phase diagram of the SrO-CuO-TiO₂ and CaO-CuO-TiO₂ ternary systems at 950°C in air since those have not been reported yet. Finally, we fabricatred CCTO films on platinized

Si substrates by pulsed laser deposition (PLD). In order to decrease the high $\tan\delta$ and leakage current in single-layered CCTO films, we tried to deposit multi-layered CCTO films with additional CaTiO_3 (CTO) layer. The major results are summarized as the following.

First, we clarified the origins of high- k in CCTO ceramics and single crystals. For CCTO ceramics, the ϵ_r values at 1 kHz showed a strong dependence on the microstructures. The k values at 1 kHz were increased from $\sim 3,000$ to $\sim 170,000$ with increasing the sintering temperature from 980 to 1000°C for 12 h in air, which was accompanied by a very large increase in the average grain size from 5 to $300\ \mu\text{m}$ due to an abnormal grain growth. With further increasing the sintering temperature up to 1080°C , the ϵ_r value at 1 kHz was decreased to $\sim 69,000$ with relatively smaller average grain size of $150\ \mu\text{m}$. While no abnormal grain growth occurred in the CCTO ceramics sintered at 980°C for the holding time up to 24 h and thus their ϵ_r values were relatively smaller ϵ_r values ($< 4,000$ at 1 kHz), the abnormal grain growth occurred in the samples after a certain holding time at the temperature higher than 1000°C and thus their ϵ_r values were abruptly increased. The data measured by complex impedance (Z^*) and modulus (M^*) spectroscopy revealed that the variation of ϵ_r values in CCTO ceramics was exactly coincident with those of grain boundary capacitance (C_{gb}) values. Meanwhile, the ϵ_r values in CCTO single crystals showed a strong dependence on the kind of electrodes so that ϵ_r value of $\sim 200,000$ at 1 kHz in the sample with Ag electrode was much higher than that of $\sim 30,000$ in the samples with Au and InGa electrodes at the same frequency. Consequently, the CDR in CCTO ceramics and single crystals originate from the grain boundary effect with high C_{gb} values and the nonohmic contact effect at the interface between sample and electrode, respectively.

Second, the dielectric properties of $C_{1-x}S_xCTO$ ($0 \leq x \leq 1$) ceramics were systemically investigated since reported literatures were not in agreement. While the ϵ_r values in both $C_{0.4}S_{0.6}CTO$ and $C_{0.6}S_{0.4}CTO$ samples were $\sim 50,000$ at 1 kHz with relatively smaller average grain size of $\sim 80 \mu m$, extremely high ϵ_r values of $\sim 120,000$ and $\sim 180,000$ at 1 kHz were observable in the CCTO and SCTO ceramics with relatively larger average grain size of ~ 160 and $\sim 250 \mu m$, respectively. The maximum $\tan \delta$ values in the CCTO and SCTO were higher than those of other samples. The frequency-dependent Z^* and M^* spectroscopy revealed that the variation of C_{gb} values in $C_{1-x}S_xCTO$ ($0 \leq x \leq 1$) ceramics exactly coincided with that of ϵ_r values, and the C_{gb} values in all samples were much higher than those of grain capacitance (C_g). Although the second phases of $SrTiO_3$ and CuO appeared for the compositions of $x \geq 0.8$, a linear increase in the lattice parameters was observable for the full range of Sr substitution suggesting that the solubility limit of Sr substituent x , exists between $x=0.6$ and $x=0.8$ in the $C_{1-x}S_xCTO$ -type solid solutions.

Third, the subsolidus phase diagram in the $SrO(CaO)-CuO-TiO_2$ ternary systems were carefully investigated at $950^\circ C$ in air. In the $SrO-CuO-TiO_2$ ternary system, it was identified for the first time that a stoichiometric SCTO compound did not exist but $Sr_{0.9639(1-y)}Cu_{3.0361(1-3y)}Ti_{4+2y}O_{12}$ -type solid solutions with the solubility limit of $0 \leq y \leq 0.0235$ turned out to exist. The variation in the lattice parameters of these new type solid solutions was negligibly small. The ϵ_r values of all solid solutions were over $\sim 70,000$ at 1 kHz with abnormally grown large grains. On the other hand, in the $CaO-CuO-TiO_2$ ternary system, we confirmed for the first time that CCTO did not form a single compound but $Ca_{1-x}Cu_{3+x}Ti_4O_{12}$ -type solid solutions with the solubility of -

$0.0191 \leq x \leq 0.0476$ turned out to exist although their lattice parameter variation was negligibly small.

Finally, we have successfully fabricated polycrystalline CCTO films with the thickness of ~500 nm on platinized Si substrates by PLD and systemically investigated the microstructures, compositional distributions, and dielectric properties depending on the various deposition temperatures ranging from 700 to 800°C. In addition, multi-layered CCTO films of CCTO/CTO, CTO/CCTO, and CTO/CCTO/CTO were successfully deposited on platinized Si and single crystal SrTiO₃ (STO) substrates for improving the high $\tan\delta$ and leakage current of single-layered CCTO films. Referring to the dielectric properties of the single-layered polycrystalline CCTO films, with increasing the deposition temperature from 700 to 750°C, the ϵ_r values in samples were greatly enhanced from ~300 to ~2,000 at 1 kHz, respectively. However, the ϵ_r values of CCTO films were gradually decreased above 750°C, which was surely attributable to the formation of a TiO₂-rich dead layer at the interface between CCTO and Pt electrode. Compositional analyses by AES, EDS and EELS revealed that, the TiO₂-rich dead layer became thicker because of severe Cu diffusion from CCTO films to Pt electrode. The leakage current behaviors of the single-layered films were in good agreement with Poole-Frenkel conduction mechanism, where both the TiO₂-rich dead layer and rutile TiO₂ nanocrystalline particles are considered to play a role of charge trapping centers.

The high $\tan\delta$ value over ~0.1 at 1 kHz in the single-layered CCTO film was remarkably decreased to ~0.05 and ~0.04 in the multi-layered films of Pt/CTO/CCTO and Pt/CTO/CCTO/CTO, respectively. Furthermore, all the multi-layered films showed much lower leakage current compared to that of single-layered film. However, a severe drop in ϵ_r values were observable in

the multi-layered films so that the ϵ_r value of ~ 750 , $\sim 1,150$, and $\sim 1,020$ at 1 kHz were obtainable in the Pt/CTO/CCTO/CTO, Pt/CTO/CCTO, and Pt/CCTO/CTO films, respectively, and these values were relatively lower than that of $\sim 2,000$ in the single-layered film at the same frequency. Therefore, we selected the Pt/CTO/CCTO film and attempted to increase the ϵ_r values by increasing the CCTO thickness from ~ 200 nm to ~ 1.2 μm since the ϵ_r values at 1 kHz in the film were relatively higher than those of other multi-layered films and the $\tan\delta$ values were comparable to those of the Pt/CTO/CCTO/CTO film. With increasing the CCTO film thickness, the ϵ_r values at 1 kHz in both the single and multi-layered films were also increased from ~ 280 to $\sim 7,400$ and from ~ 640 to $\sim 3,800$, respectively. The $\tan\delta$ value of ~ 0.05 at 1 kHz in the Pt/CTO/CCTO film was almost unaltered with increasing CCTO film thickness from ~ 200 to ~ 800 nm but the value was abruptly increased to ~ 1 at ~ 100 kHz with further increasing the thickness up to ~ 1.2 μm . The leakage current in the multi-layered films was much lower than those of single-layered film since the trap ionization energies in the multi-layered films were relatively higher than that of single-layered film. We fabricated single and multi-layered epitaxial CCTO films with CTO buffer layer and investigated the dielectric properties by increasing the CCTO film thickness from ~ 100 to ~ 700 nm on STO (001) substrates with SrRuO₃ (SRO) bottom electrode. All samples showed a perfect *c*-axis orientation but unidentified impurity phase was observable in the multi-layered films. The ϵ_r values in all samples were not increased with increasing CCTO film thickness and no remarkable decrease in $\tan\delta$ values was observable in the multi-layered films, which are attributable to the presence of large amount of pin holes on the CCTO film surface due to a large discrepancy in lattice parameter between SRO ($a=3.930$ Å) and CCTO ($a=3.695$ Å).

Keywords: $\text{CaCu}_3\text{Ti}_4\text{O}_{12}$ (CCTO), Colossal dielectric response (CDR), Dielectric constant (ϵ_r) and loss ($\tan\delta$), Leakage current, Abnormal grain growth, Complex impedance (Z^*) and modulus (M^*) spectroscopy, $(\text{Ca}_{1-x}\text{Sr}_x)\text{Cu}_3\text{Ti}_4\text{O}_{12}$ ($0 \leq x \leq 1$) ceramics, Phase compatibility, Pulsed-laser deposition (PLD), Cu-diffusion, Polycrystalline and epitaxial CCTO films, Single and multi-layered CCTO films, CaTiO_3 (CTO), SrRuO_3 (SRO), SrTiO_3 (STO)

Student Number: 2006-20868

Contents

List of Tables and Figures.....	x
Chapter 1 General Introduction.....	1
Chapter 2 General Background.....	7
2.1 Dielectric properties of CCTO bulks and films.....	7
2.1.1 CCTO ceramics and crystals.....	7
2.1.2 Polycrystalline and epitaxial CCTO Films.....	9
2.2 The mechanisms for high- k in CCTO bulks.....	11
Chapter 3 A study on the origin of high- k in CCTO bulks.....	31
3.1 Introduction.....	31
3.2 Experimental.....	32
3.3 Results and Discussions.....	34
3.3.1 High- k mechanism for ceramics.....	34
3.3.2 High- k mechanism for single crystals.....	47
3.4 Summary.....	51
Chapter 4 Colossal dielectric response of $(\text{Ca}_{1-x}\text{Sr}_x)\text{Cu}_3\text{Ti}_4\text{O}_{12}$ ($0 \leq x \leq 1$) ceramics.....	68
4.1 Introduction.....	68
4.2 Experimental.....	69
4.3 Results and Discussions.....	71
4.4 Summary.....	76

Chapter 5 Subsolidus phase diagrams of the SrO(CaO)-CuO-TiO ₂ ternary system.....	87
5.1 Introduction.....	87
5.2 Experimental.....	89
5.3 Results and Discussions.....	90
5.3.1 The SrO-CuO-TiO ₂ ternary system.....	90
5.3.2 The CaO-CuO-TiO ₂ ternary system.....	93
5.4 Summary.....	97
 Chapter 6 Dielectric properties of CCTO thin films.....	114
6.1 Introduction.....	114
6.2 Experimental.....	116
6.3 Results and Discussions.....	118
6.3.1 Polycrystalline CCTO films on Si substrates.....	118
6.3.1.1 Single-layered films.....	118
6.3.1.2 Multi-layered films.....	129
6.3.2 Epitaxial CCTO films on single crystal substrates.....	138
6.4 Summary.....	140
 Chapter 7 Summary.....	172
 Publications.....	177
 Abstract in Korean.....	180

List of Tables

Table 2.1 Dielectric properties and lattice parameters of $ACu_3Ti_4O_{12}$ (ACTO, $A = Cd, La, Sm, Dy, Y, Bi, Nd, \text{ and } Gd$) compounds.....	17
Table 2.2 Summary of the representative studies for the effects of sintering conditions on the microstructure and dielectric properties of CCTO ceramics.....	18
Table 2.3 Summary for the detailed deposition conditions and dielectric properties of polycrystalline CCTO films by PLD.....	19
Table 2.4 Summary for the detailed deposition conditions and dielectric properties of polycrystalline CCTO films by sol-gel and sputtering.....	20
Table 2.5 Impedance characteristics at ~ 300 K for CCTO ceramics sintered at 1115°C for 1-24 h in air [3].....	21
Table 3.1 The obtained $\rho_g, C_g, \rho_{gb}, C_{gb}$ values of CCTO ceramics sintered at various temperatures ranging from 980 to 1080°C for 12 h using Z^* and M^* spectroscopy.....	55
Table 3.2 The obtained $\rho_g, C_g, \rho_{gb}, C_{gb}$ values of CCTO ceramics sintered at 1060°C with various holding times from 30 min to 24 h using Z^* and M^* spectroscopy.....	56
Table 3.3 The obtained $\rho_{\text{contact+gb}}$ and $C_{\text{contact+gb}}$ values of polycrystalline CCTO ceramics sintered at 1060°C for 12 h in air.....	56

Table 4.1 The obtained ρ_g , C_g , ρ_{gb} , and C_{gb} values of $C_{1-x}S_x$ CCTO ($0 \leq x \leq 1$) ceramics sintered at various sintering temperatures ranging from 1000 to 1060°C from the equivalent circuit with two parallel RC elements using Z^* and M^* spectroscopy.....	80
Table 5.1 The selected nominal compositions and phases observed at 950°C in air in the SrO-CuO-TiO ₂ ternary system.....	100
Table 5.2 The selected nominal compositions and phases observed at 950°C in air in the CaO-CuO-TiO ₂ ternary system.....	101
Table 6.1 Calculated values of optical dielectric constant of the CCTO films based on SE and PF conduction.....	146
Table 6.2 Measured and calculated dielectric constant of single and multi-layered polycrystalline CCTO films at 1, 10, and 100 kHz.....	147
Table 6.3 Calculated trap ionization energies in single (~800 nm) and multi-layered (~800 nm) polycrystalline CCTO films based on PF conduction....	148

List of Figures

Fig. 2.1 The crystal structures of CCTO ceramics [1,13].....	22
Fig. 2.2 The SEM images of abnormally grown large grains (a) and (d) and smaller-grains (b) and (e), and frequency-dependent ϵ_r properties of CCTO ceramics in ref 2 and 10, respectively. Fig. 2.2 (g) and (h) show the SEM image of abnormally grown large grains in CCTO ceramics sintered at 1060°C for 12 h in air and Cu-mapping image by EPMA, respectively, in ref [11].....	23
Fig. 2.3 Frequency and temperature-dependent dielectric properties of CCTO single crystals fabricated by traveling solvent zone technique [13].....	24
Fig. 2.4 Z^* plot for CCTO single crystal with Au electrode at 300 K (a), CCTO ceramic with Au electrode at 373 K (b), CCTO single crystal CCTO with InGa alloy electrodes at 300 K (c), and equivalent circuit used to model impedance spectroscopy data in CCTO single crystal and ceramic [14].....	25
Fig. 2.5 The XRD patterns and SEM images of the microstructure in polycrystalline CCTO films fabricated by PLD [18].....	26
Fig. 2.6 The thickness-dependent dielectric properties of CCTO ceramics by PLD [18].....	27
Fig. 2.7 The XRD pattern (a), surface morphology (b), and frequency-dependent dielectric properties (c) and (d) of 2 μm -thickness CCTO films by PLD. [21].....	28

Fig. 2.8 The equivalent circuit of CCTO ceramics (a), Z^* spectroscopy for smaller-grained CCTO ceramics sintered at 1110° for 3 h in air (b), and larger-grained CCTO ceramics sintered at 1110°C for 24 h in air (c) [2].....29

Fig. 2.9 SEM image of CCTO ceramic sintered at 1065°C for 20 in air (a) and TEM images of domain boundary in CCTO ceramics (b), microstructure model of CCTO ceramics (c), frequency-dependent Z'' and M'' properties of CCTO ceramics (d) in ref. [43], and domain and grain boundary activation energies (e) of CCTO ceramics in ref. [50].....30

Fig. 3.1 The ϵ_r (a) and $\tan\delta$ (b) properties of CCTO ceramics fabricated at various sintering temperatures ranging from 980 to 1060°C for 12 h as a function of frequency from 100 Hz to 15 MHz. The inset of Fig. 1(b) shows the log-log plot of $\tan\delta$ properties of the CCTO samples.....57

Fig. 3.2 SEM images of CCTO ceramics sintered at various sintering temperatures of 980°C (a), 1000°C (b), 1020°C (c), 1040°C (d), 1060°C (e) and 1080°C (f), respectively, after thermal etching process at 900°C for 1 h in air. The insets of Fig. 3.2(a) and (e) show the enlarged image of Fig. 3. 2(a) and grain boundary region of Fig. 3.2(e), respectively. The inset of Fig. 3.2(c) shows the enlarged image of the small-grained regions indicated by arrows in Fig. 3.2(c).....58

Fig. 3.3 Selected SEM images of CCTO ceramics sintered at 1060°C with various holding times of 3 h (a) and (e), 6 h (b) and (f), 9 h (c) and (g), and 12 h (d) and (h), respectively. The inset of Fig. 3.3(e) shows the enlarged image of Fig. 3.3(e).....59

Fig. 3.4 Frequency dependent ϵ_r and $\tan\delta$ properties of CCTO ceramics from 100 Hz to 15 MHz sintered at 1060°C (a) and (b) and 980°C (c) and (d), respectively, with the various holding times from 30 min to 24 h. The inset of Fig. 3.4(a) shows the frequency dependent ϵ_r properties of samples with the holding times of 30min, 3 h, and 6 h. All data are replotted from our previous report of ref. [5].....60

Fig. 3.5 The frequency dependent imaginary part of Z^* and M^* spectroscopy of CCTO ceramics sintered at 980°C (a), 1000°C (b), 1020°C (c), 1040°C (d), 1060°C (e) and 1080°C (f), respectively, for 12 h in air.....61

Fig. 3.6 The Arrhenius plots of ρ_g and ρ_{gb} values of CCTO ceramics sintered at various temperatures ranging from 980 to 1080°C for 12 h.....62

Fig. 3.7 The frequency dependent imaginary part of Z^* and M^* spectroscopy of CCTO ceramics sintered at 1060°C with the various holding times of 3 h (a), 6 h (b), 9 h (c), and 12 h (d), respectively.....63

Fig. 3.8 The frequency-dependent ϵ_r and $\tan\delta$ values of polycrystalline CCTO ceramics with various electrodes.....64

Fig. 3.9 The frequency dependent imaginary part of Z^* and M^* spectroscopy of CCTO ceramics sintered at 1060°C with various electrodes.....65

Fig. 3.10 The frequency-dependent ϵ_r and $\tan\delta$ properties (a) and (b), cole-cole plot (c), and frequency-dependent imaginary part of Z^* and M^* spectroscopy of CCTO single crystals.....66

Fig. 3.11 *I-V* characteristics of polycrystalline CCTO (a), single crystal CCTO (b), and *I-V* characteristics of single crystal CCTO with InGa electrode (c), and Ag electrode (d).....67

Fig. 4.1 Powder XRD patterns (a) and lattice parameter measurement (b) of $C_{1-x}S_x$ CTO ($0 \leq x \leq 1$) ceramics.....81

Fig. 4.2 SEM images of CCTO (a), $C_{0.8}S_{0.2}$ CTO (b), $C_{0.6}S_{0.4}$ CTO (c), $C_{0.4}S_{0.6}$ CTO (d), $C_{0.2}S_{0.8}$ CTO (e), and SCTO (f) with thermal etching process at 900°C for 1 h. The inset of Fig. 4.2 (a) shows the segregated copper-oxide at grain boundary.....82

Fig. 4.3 Frequency dependent ϵ_r (a), $\tan\delta$ (b) properties of $C_{1-x}S_x$ CTO ($0 \leq x \leq 1$) ceramics from 100 Hz to 40 MHz, and the variation of the ϵ_r values from ref. 22, 29 and 30 depending on average grain size (c). Note that all the ϵ_r values are measured at 1 kHz. All the representative average grain size was measured by an image analyzer.....83

Fig. 4.4 Frequency dependent Z'' and M'' properties of CCTO (a), $C_{0.8}S_{0.2}$ CTO (b), $C_{0.6}S_{0.4}$ CTO (c), $C_{0.4}S_{0.6}$ CTiO (d), $C_{0.2}S_{0.8}$ CTO (e), and SCTO (f) ceramics measured from 10^{-2} to 10^5 Hz.....84

Fig. 4.5 Frequency dependent Z'' (a) and M'' (b) properties of $C_{1-x}S_x$ CTO ($0 \leq x \leq 1$) ceramics measured from 10^7 to 10^9 Hz.....85

Fig. 4.6 The relationship among ϵ_r values at 1 kHz, average grain size, C_g , and C_{gb} , values of $C_{1-x}S_x$ CTO ($0 \leq x \leq 1$) ceramics.....86

Fig. 5.1 The selected compositions in the $\text{Sr}_{1-x}\text{Cu}_{3+x}\text{Ti}_4\text{O}_{12}$ ($0 \leq x \leq 0.0909$) compounds (a) and powder XRD patterns (b).....	102
Fig. 5.2 The selected compositions in the $\text{Sr}_{0.9639(1-y)}\text{Cu}_{3.0361(1-y)}\text{Ti}_{4+2y}\text{O}_{12}$ ($-0.0121 \leq y \leq 0.0386$) compounds (a) and powder XRD patterns (b).....	103
Fig. 5.3 The phase relations of the SrO-rich ($\text{SrO} > \sim 36.8\%$) region in the SrO-CuO-TiO ₂ ternary system (a), and powder XRD patterns of various samples No.15 (b), No.16 (c), No. 17 (d), No. 18 (e), No. 19 (f), No. 20 (g), and No. 21 (h).....	104
Fig. 5.4 The subsolidus phase diagram in the SrO-CuO-TiO ₂ ternary system at 950°C in air.....	105
Fig. 5.5 The variation of lattice constant in the $\text{Sr}_{0.9639(1-y)}\text{Cu}_{3.0361(1-y)}\text{Ti}_{4+2y}\text{O}_{12}$ ($-0.0121 \leq y \leq 0.0386$) solid solutions.....	106
Fig. 5.6 Frequency dependent ϵ_r and $\tan \delta$ properties of $\text{Sr}_{0.9639(1-y)}\text{Cu}_{3.0361(1-y)}\text{Ti}_{4+2y}\text{O}_{12}$ -type solid solutions.....	106
Fig. 5.7 The selected compositions in the $\text{Ca}_{1-x}\text{Cu}_{3+x}\text{Ti}_4\text{O}_{12}$ ($-0.0526 \leq x \leq 0.0698$) compounds (a) and powder XRD patterns (b) and (c).....	107
Fig. 5.8 The selected compositions in the $\text{Ca}_{1.0191(1+y)}\text{Cu}_{2.9809(1+y)}\text{Ti}_{4-2y}\text{O}_{12}$ ($0.0043 \leq y \leq 0.0397$) and $\text{Ca}_{0.952-z}\text{Cu}_{3.047-3z}\text{Ti}_{4+2z}\text{O}_{12}$ ($-0.0160 \leq z \leq 0.0454$) compounds (a) and powder XRD patterns (b) and (c).....	108

Fig. 5.9 The selected compositions in the $\text{Ca}_{1.0191(1-w)}\text{Cu}_{2.9809+9.0191w}\text{Ti}_{4-4w}\text{O}_{12}$ ($0.0021 \leq w \leq 0.0146$) compounds and the phase compatibilities of the sample No. 23, 24, 25, and 26 (a) and powder XRD patterns (b) and (c).....109

Fig. 5.10 The subsolidus phase diagram in the CaO-CuO-TiO₂ ternary system at 950°C in air.....110

Fig. 5.11 The XRD patterns of samples from No.4 to No.10 at 950°C for 24 h in air with Si powder (a) enlarged XRD patterns of Si (b) enlarged XRD patterns of CCTO main peaks (c), and the variation of lattice constants in the $\text{Ca}_{1-x}\text{Cu}_{3+x}\text{Ti}_4\text{O}_{12}$ -type ($-0.0191 \leq x \leq 0.0476$) solid solutions.....111

Fig. 5.12 The XRD patterns of samples from No.4 to No.10 at 1050°C for 24 h in air with Si powder (a) enlarged XRD patterns of Si (b) enlarged XRD patterns of CCTO main peaks (c), and the variation of lattice constants in the $\text{Ca}_{1-x}\text{Cu}_{3+x}\text{Ti}_4\text{O}_{12}$ -type ($-0.0191 \leq x \leq 0.0476$) solid solutions sintered at 1050°C for 24 h in air.....112

Fig. 5.13 The surface images of solid solutions after sintering at 1050°C for 24 h in air (a) and subsolidus phase diagram in the CaO-CuO-TiO₂ ternary system at 950°C in air (b).....113

Fig. 6.1 FESEM images of CCTO thin films deposited at 700°C (a), 725°C (b), 750°C (c), 775°C (d), 800°C (e) with slow cooling rate (3°C/min) at high oxygen pressure of 66 kPa and deposited at 700°C (f), 725°C (g), 750°C (h), 775°C (i), 800°C (j) with fast cooling rate (~20°C/min) at low oxygen pressure of 100 Pa. (White arrows in Fig. 6.1 (h)-(j) indicated not segregated copper-

oxides but out-grown large particles by PLD process.).....149

Fig. 6.2 EPMA mapping images of selected CCTO films: (a) and (b) shows secondary electron and Cu-K α edge mapping images of CCTO films, respectively, cooled down slowly (3°C/min) at high oxygen pressure of 66kPa. (c) and (d) shows secondary electron and Cu-K α edge mapping images of CCTO films, respectively, cooled down fast (~20°C /min) at lower oxygen pressure of 100Pa.....150

Fig. 6.3 XRD patterns of selected CCTO films: (a) CCTO film cooled down slowly at high oxygen pressure of 66 kPa after grown at 750°C. CCTO films cooled down fast at low oxygen pressure of 100 Pa after grown at (b) 800°C, (c) 750°C, and (d) 700°C.....151

Fig. 6.4 Dielectric constant (ϵ_r) and loss ($\tan\delta$) properties of CCTO thin films as a function of deposition conditions at the frequencies of 10 and 100 kHz. (Closed symbol is denoted by the case of slow cooling at high oxygen pressure of 66 kPa and open symbol the case of fast cooling at low oxygen pressure of 100 Pa).....152

Fig. 6.5 XRD patterns of CCTO films deposited under various substrate temperatures ranging from 700°C to 800°C on Pt/TiO₂/SiO₂/Si substrates (a) and enlarged diffraction patterns of Pt electrode (b). Notice that this is semi-logarithmic plot and all data are from our previous report of ref. [25].....153

Fig. 6.6 Cross sectional TEM images of CCTO films deposited at 700°C (a), 725°C (b), 750°C (c), 775°C (d) and 800°C (e) on platinized Si substrate, respectively. The Ti diffusion from the glue layer of TiO₂ is indicated by black arrows. The upper and lower inset of Fig. 6.6(f) shows the SADP

images of CCTO grain inside and dead layer of CCTO film deposited at 775°C, respectively.....154

Fig. 6.7 Dielectric constant (a) and loss (b) properties of CCTO films as a function of frequency from 100 Hz to 1 MHz. Note that all the measured ϵ_r and $\tan\delta$ values are from our previous report of ref. [25].....155

Fig. 6.8 The EDS mapping images of CCTO films deposited at 700°C, 750°C, and 800°C by Cu-mapping (a), (e), and (i), Pt-mapping (b), (f) and (j), Ti-mapping (c), (g) and (k), respectively. The compositional depth profiles by AES of CCTO films deposited at 700°C (d), 750°C (h), and 800°C (l), respectively. The each divided region of ①, ②, ③, and ④ indicates CCTO films, dead layer, Pt electrode and SiO₂, respectively.....156

Fig. 6.9 The low magnification TEM image of Pt electrode in the CCTO deposited at 800°C (a). The inset of (a) shows the FFT image of region 1 in Pt electrode. Fig. 6.9(b) shows the FFT image of PtCu₃ (111) in region 2 with Pt (111) electrode.....157

Fig. 6.10 The TEM-EDS Cu-mapping images of CCTO films deposited at 700°C (a), 750°C (b), 800°C (c), and EELS spectra of CCTO grain (1) and TiO₂-rich dead layer region (2) of CCTO film deposited at 800°C, respectively. (d).....158

Fig. 6.11 The *I-V* measurement of CCTO films under DC bias condition for plots of *J* vs. *E* (a) for plots of log *J* vs. *E*^{1/2} fitted by Schottky thermionic emission (b) and for plots of log (*J/E*) vs. *E*^{1/2} by Poole-Frenkel conduction mechanism (c).....159

Fig. 6.12 Cross section TEM image of CCTO film deposited at 775°C on platinized Si substrate (a), enlarged image of grain boundary (b), HR-TEM image of nanocrystallized rutile TiO₂ in grain boundary (c), and EELS spectra of grain and nanocrystallized TiO₂ in grain boundary (d). The inset of (d) shows the enlarged view of EELS spectra for Ti-L_{2,3} edge.....160

Fig. 6.13 The SEM images of single (a) & (e) and multi-layered CCTO (500nm) films of Pt/CTO/CCTO (b) & (f), Pt/CCTO/CTO (c) & (g), and Pt/CTOCCTO/CTO (d) & (h).....161

Fig. 6.14 Frequency-dependent dielectric constant (a) and loss (b) properties and *I-V* characteristics (c) of single and multi-layered CCTO (500nm) films.....162

Fig. 6.15 XRD patterns of single and multi-layered CCTO films with thickness ranging from ~200 nm to ~1.2 μm deposited on Pt/TiO₂/SiO₂/Si substrates (a) and (c), respectively, and enlarged XRD patterns of single and multi-layered films (b) and (d), respectively.....163

Fig. 6.16 Surface morphologies (a)-(d) and (i)-(l) and cross sectional SEM images (e)-(h) and (m)-(p) of single and multi-layered films, respectively.....164

Fig. 6.17 Cross sectional TEM image (a) and EDS Cu-mapping image (b) of ~750 nm multi-layered film. The compositional depth profiles of ~800 nm single-layered films (c) and ~750 nm multi-layered film (d) by AES Analysis.....165

Fig. 6.18 Dielectric constant of single and multi-layered films (a)-(d) and loss (e)-(h) properties of single and multi-layered films as a function of frequency from 100 Hz to 1 MHz.....166

Fig. 6.19 The representative measured and calculated ϵ_r (a)-(c) and $\tan\delta$ (d)-(f) values of single and multi-layered films at 1, 10, and 100 kHz.....167

Fig. 6.20 The temperature dependent I - V measurement for plots of $\log J$ vs. $1000/T$ in ~ 800 nm single (a) and ~ 750 nm multi-layered film (b) fitted by Poole-Frenkel conduction mechanism.....168

Fig. 6.21 XRD patterns of single and multi-layered epitaxial CCTO films by θ - 2θ measurement (a)-(b), and Φ -scan (c).....169

Fig. 6.22 Frequency-dependent dielectric constant (a) and loss (b) properties of single and multi-layered epitaxial CCTO films on STO single crystal substrates.....170

Fig. 6.23 Surface morphologies by SEM (a)-(d) and AFM images (e)-(h) of single-layered epitaxial CCTO films.....171

Chapter 1. General Introduction

Since the discovery of colossal dielectric response (CDR, $\epsilon_r > \sim 10,000$) of cubic perovskite $\text{CaCu}_3\text{Ti}_4\text{O}_{12}$ (CCTO) ceramics by Subramanien *et al.*[1], considerable attention has been paid in the research field for clarifying the physical origin of CDR in CCTO ceramics. In addition, the abrupt decrease in dielectric constant (ϵ_r), which frequently observable in ferroelectric materials at phase transition temperature, has not been observable in CCTO ceramics due to the absence of phase transition over a wide temperature region of 100~600 K.[1-2] However, the origin for CDR in CCTO has not been clarified yet and high dielectric loss ($\tan\delta$) and leakage current with a low breakdown voltage in CCTO have hindered a real application in the capacitor industry. Therefore, numerous mechanisms for understanding CDR in CCTO bulks and various attempts for improving the $\tan\delta$ and leakage current properties of CCTO ceramics and films have been suggested in literatures.

First of all, related to the physical origin of CDR in CCTO ceramics, numerous models such as grain boundary internal barrier layer capacitor (IBLC) model [3-7], domain boundary IBLC model [8-10], and twin boundary IBLC model [11-12] have been suggested as the mechanism for CDR. Among these mechanisms, grain boundary IBLC model is the most widely accepted model. According to this model, the ϵ_r values are proportional to the grain boundary capacitance (C_{gb}) values and the C_{gb} values are strongly dependent on the average grain size of CCTO ceramics.[5, 13] Therefore, the ϵ_r and C_{gb} values in CCTO ceramics with abnormally grown large grains are

significantly higher than those of smaller-grained samples. However, CDR is also observable in CCTO single crystals without grain boundaries so that alternative mechanisms of domain and twin boundary IBLC models have been proposed.[8-12] According to these models, CDR in CCTO ceramics and single crystals is attributable to the insulating domain or twin boundaries and these boundaries could be formed by chemical inhomogeneity and crystal defects, respectively. Recently, one research group have insisted that the origin for CDR in CCTO ceramics and single crystals should be different so that high C_{gb} values and nonohmic contact effects could be the origin for CDR in ceramics and single crystals, respectively.[14] Therefore, it can be said that the mechanism of CDR in CCTO still not in consensus.

As mentioned previously, the high $\tan\delta$ and leakage current in CCTO should be decreased for practical application. In order to overcome these problems, numerous research groups have tried to improve the dielectric and electrical properties of CCTO by adopting second phase addition [15-18] and substitution of cations [19-31] for ceramics and multi-layered structures for films [32]. Among the various attempts, somewhat decreased $\tan\delta$ and leakage current were achievable in the La-substituted $\text{Ca}_{0.8}\text{La}_{0.2}\text{Cu}_3\text{Ti}_4\text{O}_{12}$ ceramic [28] and multi-layered structure of $\text{CaTiO}_3/\text{CCTO}/\text{CaTiO}_3$ film [32]. However, the ϵ_r values in the ceramic were simultaneously decreased with $\tan\delta$ values and the $\tan\delta$ values in the films were still high for real application. On the basis of the above motivations, we tried to unveil the physical origin of high- k in CCTO ceramic and single crystals. Furthermore, we attempted to decrease high $\tan\delta$ values in both CCTO bulks and films. Finally the phase compatibilities in the $\text{SrO}(\text{CaO})\text{-CuO-TiO}_2$ ternary systems were carefully

investigated at 950°C in air. The detailed objectives and significant results in this thesis are as follow.

In chapter 3, we attempted to unveil the origin of high- k in CCTO ceramics by investigating the overall relationship among sintering conditions, microstructures and dielectric properties. In addition, we investigated the effects of various electrodes on the dielectric properties of CCTO single crystals for revealing the reason of CDR in CCTO single crystals. The extremely high ϵ_r values at 1 kHz in CCTO ceramics are surely originated from the high C_{gb} values. Especially, the ϵ_r and C_{gb} values are strongly dependent on the average grain size and density of abnormally grown large grains in CCTO ceramics. While the ϵ_r values in CCTO ceramics are almost unaltered depending on the electrodes, the values in CCTO single crystals show strong dependence on the electrodes. Therefore, the high C_{gb} values and nonohmic contact resistance (R) between sample and electrode are the origins of CDR in CCTO ceramics and single crystals, respectively,

In chapter 4, we have fabricated $\text{Ca}_{1-x}\text{Sr}_x\text{Cu}_3\text{Ti}_4\text{O}_{12}$ ($0 \leq x \leq 1$) ceramics using solid state reaction and systemically investigated the effectiveness of Sr substitution for improving the dielectric properties of CCTO ceramics. Furthermore, the relationship between microstructures and dielectric properties of $\text{Ca}_{1-x}\text{Sr}_x\text{Cu}_3\text{Ti}_4\text{O}_{12}$ ($0 \leq x \leq 1$) ceramics, which has never been investigated in the previous reports, was carefully investigated. Finally, the solubility limit of Sr substituent x for Ca site was successfully determined by investigating the lattice parameter variations.

In chapter 5, the subsolidus phase compatibilities in the SrO(CaO)-CuO-TiO₂ ternary systems were investigated at 950°C in air. Because the pure

phase $\text{SrCu}_3\text{Ti}_4\text{O}_{12}$ (SCTO) ceramic does not exist [31] and no information for the existence of solid solutions in SCTO and CCTO compounds is available in literature. The composition of single phase SCTO was successfully determined and new type of solid solutions were firstly identified in the SrO-CuO-TiO₂ ternary system. A wide range of $\text{Ca}_{1-x}\text{Cu}_{3+x}\text{Ti}_4\text{O}_{12}$ solid solutions existed in the CaO-CuO-TiO₂ ternary system.

Finally, in chapter 6, we fabricated single and multi-layered polycrystalline and epitaxial CCTO films using pulsed laser deposition (PLD) for practical application. We investigated the effects of deposition temperatures, ranging from 700 to 800°C, on the dielectric and leakage current properties of single-layered polycrystalline CCTO films by carefully investigating detailed microstructures and chemical distribution of samples using various analysis methods. Furthermore, we tried to decrease the high $\tan\delta$ values and leakage current of CCTO films by adopting the additional CaTiO_3 (CTO) layer in multi-layered structures. The severe drop of ε_r values in the multi-layered films were overcome by increasing the thickness of CCTO layer from ~200 nm to ~1.2 μm . The dielectric properties of epitaxial CCTO films with SrRuO_3 bottom electrode were also investigated on SrTiO_3 single crystal substrates.

References

- [1] M. A. Subramanian *et al.*, *J. Solid. State. Chem.*, 151, 323 (2000)
- [2] C. C. Homes *et al.*, *Science.*, 293, 673 (2001)
- [3] D. C. Sinclair *et al.*, *Appl. Phys. Lett.*, 80, 2153 (2002)
- [4] T. B. Adams *et al.*, *Adv. Mater.*, 14, 1321 (2002)
- [5] T. B. Adams *et al.*, *J. Am. Ceram. Soc.*, 89, 3129 (2006)
- [6] S. Y. Chung *et al.*, *Nat. Mater.*, 3, 774 (2004)
- [7] Y. H. Lin *et al.*, *J. Appl. Phys.*, 103, 074111 (2008)
- [8] T. T. Fang *et al.*, *Chem. Mater.*, 17, 5167 (2005)
- [9] M. A. Ramirez *et al.*, *J. Phys. D Appl. Phys.*, 42, 185503 (2009)
- [10] S. Krohns *et al.*, *Appl. Phys. Lett.*, 91, 022910 (2007)
- [11] J. Li *et al.*, *Solid State Commun.*, 135, 260 (2005)
- [12] M. H. Whangbo *et al.*, *Chem. Mater.*, 18, 3257 (2009)
- [13] S. Y. Lee *et al.*, *Electron. Mater. Lett.*, 3, 23 (2007)
- [14] M. C. Ferrarelli *et al.*, *J. Mater. Chem.*, 19, 5916 (2009)
- [15] F. Amaral *et al.*, *J. Non-Cryst Solids.*, 357, 775 (2011)
- [16] E. A. Patterson *et al.*, *Appl. Phys. Lett.*, 87, 182911 (2005)
- [17] Y. H. Lin *et al.*, *J. Appl. Phys.*, 103, 074111 (2008)
- [18] C. M. Wang *et al.*, *J. Alloy. Compd.*, 491, 423 (2010)
- [19] M. Li *et al.*, *J. Appl. Phys.*, 104, 074107 (2008)
- [20] S. Y. Chung *et al.*, *Appl. Phys. Lett.*, 89, 191907 (2006)
- [21] C. H. Mu *et al.*, *J. Alloy. Compd.*, 471, 137 (2009)
- [22] M. Li *et al.*, *Appl. Phys. Lett.*, 88, 232903, (2006)
- [23] S. F. Shao *et al.*, *Appl. Phys. Lett.*, 91, 042905 (2007)
- [24] J. Cai *et al.*, *Appl. Phys. Lett.*, 91, 252905 (2007)
- [25] S. Y. Chung *et al.*, *Appl. Phys. Lett.*, 91, 091912 (2007)

- [26] S. H. Hong et al., *J. Am. Ceram. Soc.*, 90, 2118 (2007)
- [27] S. W. Choi et al., *J. Am. Ceram. Soc.*, 90, 4009 (2007)
- [28] L. Feng et al., *Phys. Stat. Sol.*, (a), 203, R22 (2006)
- [29] H. Xue et al., *J. Alloy. Compd.*, 482, L14 (2009)
- [30] R. Schmidt et al., *Chem. Mater.*, 22, 6 (2010)
- [31] J. Li et al., *Chem. Mater.*, 16, 5223 (2004)
- [32] L. Fang et al., *J. Appl. Phys.*, 100, 104101 (2006)

Chapter 2. General Background

2.1 Dielectric properties of CCTO bulks and films

2.1.1 CCTO ceramics and crystals

Recently, the cubic perovskite CCTO ceramics showing CDR ($\epsilon_r > 10,000$) has attracted a worldwide attention. Subramanian *et al.*[1] have synthesized CCTO ceramics using solid state reaction at 1000~1200°C for 20 h in air and measured the dielectric constant (ϵ_r) of ~12,000 at 1 kHz for the first time. On the basis of their investigation, only CCTO compound shows high ϵ_r values over ~10,000 compared to those of $ACu_3Ti_4O_{12}$ (ACTO, A= Cd, La, Sm, Dy, Y, Bi, Nd, and Gd) family compounds as shown in Table 2.1. The crystal structure of CCTO compound was represented in Fig. 2.1. As shown in Fig. 2.1, the crystal structure of CCTO is included in space group of $Im\bar{3}$ (No. 204) and no ferroelectric phase transition is observable in a wide temperature range between 100 and 600 K. [1]

However, the ϵ_r values of CCTO ceramics are strongly dependent on the processing conditions such that a wide variety of ϵ_r values from ~200 to ~280,000 have been reported in literatures. Among various processing conditions, the sintering temperature and holding time are the most important processing parameters. For instance, Adams *et al.*[2-3] reported that the ϵ_r values of CCTO ceramics were increased from ~9,000 to ~280,000 at 10 kHz sintered at 1115°C with increasing the holding time from 3 to 24 h, respectively. In addition, Lee *et al.*[4] reported that the ϵ_r values

were increased from $\sim 3,000$ to $\sim 90,000$ at 1 kHz with increasing the sintering temperature from 980 to 1080°C for 12 h. The representative studies for the effects of sintering conditions on the microstructure and dielectric properties of CCTO ceramics are summarized in Table 2.2. As shown in Table. 2.2, the ϵ_r values in CCTO ceramics are strongly dependent on the sintering temperature, holding times, and microstructures so that the ϵ_r values are generally increased with increasing the average grain size. Meanwhile, an abnormal grain growth is frequently observable in CCTO ceramics due to the presence of CuO-rich liquid phase at grain boundary during sintering at temperatures higher than 1000°C. The the severe CuO segregation at grain boundary in CCTO ceramics was clearly observable after thermal etching at 900°C for 1 h in Fig. 2.2(g) and electron probe micron analyzer image of in Fig. 2.2(h). The ϵ_r values in samples with an average grain size larger than $\sim 100 \mu\text{m}$ in Fig. 2.2 (a), and (d) are remarkably higher than those of samples with relatively smaller grains in Fig. 2.2(c) and (f). The reason for the presence of CuO-rich liquid phase is unclear at this stage but it could be related to the eutectic liquid formation between CuO and TiO_2 phase. Consequently, the dielectric properties of CCTO ceramics are strongly affected by the microstructure evolution through CuO-rich liquid phase during sintering.

In contrast to the abundant investigations for CCTO ceramics, the dielectric properties of CCTO single crystals have been rarely reported in literatures. Since CCTO compound show incongruent melting behaviors at elevated temperatures of 1165°C by previously reported by Yang *et al.*[12], it is quite difficult for synthesizing stoichiometric CCTO single crystal by melt

growth method. Within the best of our knowledge, only one research group have synthesized CCTO single crystal and reported the dielectric properties. Homes *et al.*[13] have synthesized CCTO single crystal using travelling-solvent floating-zone method and observed high ϵ_r values at 1 kHz. The ϵ_r value at 1 kHz was $\sim 80,000$ at 250 K and the value was unaltered with decreasing the measuring temperature to 100 K in Fig. 2.3. According to their investigation, CDR is responsible for the existence of twin boundaries in crystal but detailed investigations on the microstructure using high resolution transmission electron microscopy (HR-TEM) are absent. Recently, Ferrarelli *et al.*[14] have reported that the dielectric properties of CCTO single crystals fabricated by the same process with Homes *et al.*[13]. Fig. 2.4 (a)-(c) shows the frequency-dependent Z'' properties of CCTO single crystals with two different electrodes of Au and InGa. As shown in Fig. 2.4(a) and (c) the contact R values between CCTO single crystal and Au electrode were much higher than those of sample with InGa electrode. More detailed investigations for clarifying the reasons for CDR in CCTO single crystal will be represented later.

2.1.2 Polycrystalline and epitaxial CCTO films

The polycrystalline and epitaxial CCTO films have been fabricated on platinized Si and single crystal substrates, respectively, by numerous deposition techniques including pulsed laser deposition (PLD) [15-28], sol-gel [29-34], sputtering [35-37], and metal organic vapor phase deposition [38-39]. While the polycrystalline CCTO films fabricated on platinized Si

substrates by PLD show ϵ_r values in the region of 1,500~2,500 at 10 kHz, relatively lower ϵ_r values than PLD-processed films are observable in the samples by the sol-gel, sputtering, and MOCVD techniques. Although most of CCTO films on platinized Si substrates by PLD are deposited at a fixed substrate temperatures[15,19-20,24,26-28], only one systematic study identifying the relationship among processing parameters, microstructure and dielectric properties of CCTO films by PLD is available in literature by Fang *et al.*[18] In their investigation, they reported the effects of deposition temperature ranging from 450 to 700°C and oxygen pressure ranging from 2.66 to 26.6 Pa on the microstructures and dielectric properties of CCTO films. Fig. 2.5 represents the XRD patterns and microstructures of polycrystalline CCTO films in ref. 18 fabricated under various deposition conditions. As shown in Fig. 2.5(a), the pure phase CCTO films without pyrochlore phase could be only formed under higher oxygen pressure over 13.3 Pa with (220)-preferential orientation. The corresponding surface morphologies under the oxygen pressures of 13.3 and 26.6 Pa are shown in Fig. 2.5(d) and (e), respectively, indicating that square shaped CCTO grains are densely packed on platinized Si substrates. Similarly, the (220)-preferential orientation and large amount of square shaped CCTO grains start to occur under relatively high deposition temperatures higher than 700°C in Fig. 2.5(f) and (i), respectively. With increasing the film thickness from 250 to 610 nm, the extent of (220)-preferred orientation and the average grain size are increased as shown in Fig. 2.5 (k) and (o). Fang *et al.*[18] concluded that CCTO films with a (220)-preferential orientation and dense morphologies are only obtainable under oxygen pressure and

deposition temperatures higher than 13.3 Pa and 700°C, respectively. The thickness dependent dielectric properties of CCTO films in their study are represented in Fig. 2.6. In Fig. 2.6, the ϵ_r values at 1 kHz are increased with increasing the film thickness.

Meanwhile, the ϵ_r values in epitaxial CCTO films are relatively higher than those of polycrystalline films. Up to date, the highest ϵ_r values of ~14,000 at 1 kHz are observable in the *c*-axis orientated epitaxial CCTO films reported by Zhao *et al.*[21]. In addition, Si *et al.*[16] and Lin *et al.*[17] have fabricated epitaxial CCTO films on LaAlO₃ (LAO) by PLD and reported the ϵ_r values of ~2,000 and ~10,000 at 1 kHz and 1 MHz, respectively. In Zhao *et al.*'s[21] study, they fabricated *c*-axis oriented epitaxial CCTO films on Ag-coated LAO substrates by PLD and varied the film thickness from 900 nm to 2 μm . The microstructure, XRD patterns and frequency-dependent dielectric properties are represented in Fig. 2.7. On the basis of these results, they argued that the ϵ_r values are proportional to the average grain size and film thickness so that the remarkably high ϵ_r value of ~14,000 at 1 kHz in the 2 μm -thickness film was attributable to the relatively larger average grain size of 2.5 μm . The detailed deposition conditions and ϵ_r values of polycrystalline and epitaxial CCTO films by various deposition methods in literatures are summarized in Table. 2.3 and 2.4.

2.2 The mechanisms for high-*k* in CCTO bulks

Many research groups have tried to unveil the physical origin of CDR in CCTO ceramics. Thus, numerous mechanisms such as grain

boundary IBLC model,[2-3, 40-42] domain boundary IBLC model[43-45], twin boundary IBLC model[46-47], and sample-electrode interface effects [14] have been suggested for the origin of CDR in CCTO ceramics. Among them, the grain boundary IBLC model is the most widely accepted one. In the grain boundary IBLC model, CCTO ceramics are consisted of two electrically heterogeneous regions of conducting grains and insulating grain boundaries connected in series as shown in Fig. 2.8(a). In this model, the dielectric properties of CCTO ceramics are dominantly affected by the grain boundary resistance (R_{gb}) and C_{gb} values. For instance, Adams *et al.*[2-3] have insisted that extremely high ϵ_r values were only observable in CCTO ceramics with abnormally grown large grains and the high ϵ_r values were attributable to the high C_{gb} values. They measured the R_{gb} and C_{gb} values in CCTO ceramics sintered at 1115°C with numerous holding times from 1 to 24 h usings Z^* spectroscopy and observed that the R_{gb} and C_{gb} values in larger-grained samples were much lower and higher than those of smaller-grained samples, respectively, in Fig. 2.8(b), (c), and Table 2.5. Consequently, they suggested that grain boundary IBLC model should be the origin for CDR in CCTO ceramics.

However, since the extremely high ϵ_r values were reported also for CCTO single crystals,[13] alternative mechanisms have been proposed for CDR in CCTO ceramics.[43-47] Fang *et al.*[43,50] have insisted that insulating domain boundaries indicated by arrows in Fig. 2.9(a)-(c) should exist in each grain of CCTO ceramics and thus CDR in CCTO ceramics was attributable to the domain boundary IBLC model. They also proposed that CDR in CCTO single crystal might originate from the domain boundary

within single crystal. However, the peaks of Z'' and M'' spectroscopy in their study were not assigned as domain boundary in Fig. 2.9(d) and the activation energy of domain boundary in Fig. 2.9(e) was quite similar to that of grains in conventional CCTO ceramics in Fig. 2.9(e). Therefore, the domain boundary IBLC model could be inappropriate as the origin for CDR in CCTO ceramics. The twin boundary IBLC model, which was suggested as the origin of CDR in CCTO single crystal by Subramanian *et al.*[1] and Li *et al.*[46], was also proposed for the origin of CDR in CCTO ceramics. However, the existence of twin boundaries in each grain of ceramics and within single crystals has not been clarified yet using high resolution transmission electron microscopy (HR-TEM).

Lukenheimer *et al.*[48], Krohns *et al.*[45], and Yang *et al.*[49] suggested that CDR in CCTO ceramics was ascribed to interface barrier layer between sample and electrode. More recently, Ferrarelli *et al.*[14] have suggested that CDR in CCTO ceramics and single crystals originated from the grain boundary IBLC model and a non-ohmic interface effect, respectively. As previously mentioned in Fig. 1.4, the contact R values at the interface between CCTO single crystal and InGa electrode were relatively lower than those of sample with Au electrode so that they argued that CDR in CCTO single crystal should be attributable to the effects of interface between sample and electrodes. Consequently, the origin of CDR in CCTO ceramics is still not in consensus.

References

- [1] M. A. Subramanian *et al.*, *J. Solid. State. Chem.*, 151, 323 (2000)
- [2] T. B. Adams *et al.*, *Adv. Mater.*, 14, 1321 (2002)
- [3] T. B. Adams *et al.*, *J. Am. Ceram. Soc.*, 89, 3129 (2006)
- [4] S. Y. Lee *et al.*, *Electron. Mater. Lett.*, 7, 287 (2011)
- [5] B. S. Prakash *et al.*, *J. Phys. Chem. Solids.*, 68, 490 (2007)
- [6] D. K. Yoo *et al.*, *Solid. State. Phenom.*, 124, 143 (2007)
- [7] G. Zhang *et al.*, *J. Phys. D : Appl. Phys.*, 38, 1824 (2005)
- [8] L. Ni *et al.*, *Solid. State. Commun.*, 139, 45 (2006)
- [9] W. Yuan *et al.*, *J. Phys. D : Appl. Phys.*, 42, 175401 (2009)
- [10] S. F. Shao *et al.*, *J. Appl. Phys.*, 99, 084106 (2006)
- [11] D. K. Yoo *et al.*, *M. A. Thesis.*, (2006)
- [12] S. D. Yang *et al.*, *M. A. Thesis.*, (2003)
- [13] C. C. Homes *et al.*, *Science.*, 293, 673 (2001)
- [14] M. C. Ferrarelli *et al.*, *J. Mater. Chem.*, 19, 5916 (2009)
- [15] L. Fang *et al.*, *Appl. Phys. A.*, 80, 1763 (2005)
- [16] W. Si *et al.*, *Appl. Phys. Lett.*, 81, 2056 (2002)
- [17] Y. Lin *et al.*, *Appl. Phys. Lett.*, 81, 631 (2002)
- [18] L. Fang *et al.*, *Thin Solid Films.*, 440, 60 (2003)
- [19] L. Fang *et al.*, *J. Appl. Phys.*, 95, 6483 (2004)
- [20] G. Deng *et al.*, *Appl. Phys. Lett.*, 91, 202903 (2007)
- [21] Y. L. Zhao *et al.*, *Thin Solid Films.*, 445, 7 (2003)
- [22] G. Deng *et al.*, *Appl. Phys. Lett.*, 92, 172909 (2008)
- [23] M. Mitsugi *et al.*, *Appl. Phys. Lett.*, 90, 242904 (2007)

- [24] L. Fang *et al.*, *Solid State Commun.*, 137, 381 (2006)
- [25] S. Y. Lee *et al.*, *Thin Solid Films.*, 518, 5711 (2010)
- [26] G. Deng *et al.*, *J. Appl. Phys.*, 105, 084106 (2009)
- [27] L. Fang *et al.*, *J. Appl. Phys.*, 100, 104101 (2006)
- [28] L. Fang *et al.*, *J. Cryst. Growth.*, 310, 3470 (2008)
- [29] Y. W. Li *et al.*, *Appl. Phys. Lett.*, 92, 042901 (2008)
- [30] D. Maurya *et al.*, *Bull. Mater. Sci.*, 31, 55 (2008)
- [31] R. Jimenez *et al.*, *J. Eur. Ceram. Soc.*, 27, 3829 (2007)
- [32] Y. W. Li *et al.*, *J. Cryst. Growth.*, 310, 378 (2008)
- [33] L. C. Chang *et al.*, *Thin Solid Films.*, 516, 454 (2007)
- [34] D. P. Singh *et al.*, *Mater. Sci. Eng. B.*, 157, 58 (2009)
- [35] E. Joanni *et al.*, *Appl. Phys. Lett.*, 92, 132110 (2008)
- [36] S. Y. Lin *et al.*, *J. Electron. Mater.*, 38, 453 (2009)
- [37] B. S. Prakash *et al.*, *Thin Solid Films.*, 516, 2874 (2008)
- [38] R. L. Nigro *et al.*, *Surf. Coat. Technol.*, 201, 9243 (2007)
- [39] R. L. Nigro *et al.*, *Thin Solid Films.*, 515, 6470 (2007)
- [40] D. C. Sinclair *et al.*, *Appl. Phys. Lett.*, 80, 2153 (2002)
- [41] S. Y. Chung *et al.*, *Nat. Mater.*, 3, 774 (2004)
- [42] Y. H. Lin *et al.*, *J. Appl. Phys.*, 103, 074111 (2008)
- [43] T. T. Fang *et al.*, *Chem. Mater.*, 17, 5167 (2005)
- [44] M. A. Ramirez *et al.*, *J. Phys. D Appl. Phys.*, 42, 185503 (2009)
- [45] S. Krohns *et al.*, *Appl. Phys. Lett.*, 91, 022910 (2007)
- [46] J. Li *et al.*, *Solid State Commun.*, 135, 260 (2005)
- [47] M. H. Whangbo *et al.*, *Chem. Mater.*, 18, 3257 (2009)
- [48] P. Lukenheimer *et al.*, *Phys. Rev. B.*, **70**, 172102 (2004)

[49] J. Yang *et al.*, *Mater. Lett.*, **59**, 3990 (2005).

[50] T. T. Fang *et al.*, *J. Am. Ceram. Soc.*, **87**, 2072 (2004)

Table 2.1 Dielectric properties and lattice parameters of $ACu_3Ti_4O_{12}$ (ACTO, A= Cd, La, Sm, Dy, Y, Bi, Nd, and Gd) compounds

Compound	Relative dielectric constant (K)	Loss tangent (D)	a (Å at 25°C)
$CaCu_3Ti_4O_{12}$	10,286	0.067	7.391
$CdCu_3Ti_4O_{12}$	409	0.093	7.384
$La_{2/3}Cu_3Ti_4O_{12}$	418	0.060	7.427
$Sm_{2/3}Cu_3Ti_4O_{12}$	1,665	0.048	7.400
$Dy_{2/3}Cu_3Ti_4O_{12}$	1,633	0.040	7.386
$Y_{2/3}Cu_3Ti_4O_{12}$	1,743	0.049	7.383
$Bi_{2/3}Cu_3Ti_4O_{12}$	1,871	0.065	7.413
$BiCu_3Ti_3FeO_{12}$	692	0.082	7.445
$LaCu_3Ti_3FeO_{12}$	44	0.339	7.454
$NdCu_3Ti_3FeO_{12}$	52	0.325	7.426
$SmCu_3Ti_3FeO_{12}$	52	0.256	7.416
$GdCu_3Ti_3FeO_{12}$	94	0.327	7.409
$YCu_3Ti_3FeO_{12}$	33	0.308	7.394

^a Measured at 100 KHz.

Table 2.2 Summary of the representative studies for the effects of sintering conditions on the microstructure and dielectric properties of CCTO ceramics

Sintering conditions (Temp & Time)	Calcination conditions (Temp & Time)	Microstructure (Average grain size)	Dielectric properties (ϵ_r)	Reference
1115°C (1 ~ 24 h)	1000°C - 24 h	1 h : ~3-5 μm 8 h : mixed with 3-5 μm and ~100 μm 24 h : 50-300 μm	1 h : C_{gb} = 0.76 nF 24 h : C_{gb} = 35.37 nF	3
1100°C (2.5 ~ 20 h)	1000°C - 10 h	2.5 h : mixed with 3-5 μm and 10-20 μm 5 h : mixed with 1-2 μm and 40-50 μm 10 - 15 h : 40~60 μm	2.5 h : ~2,500 @ 1 kHz 5 h : ~17,000 7.5 h : ~25,000 10 h : ~30,000 15 h : ~35,000	5
1100°C (3 ~ 24 h)	1000°C - 24 h	3 h : ~5 μm 24 h : >100 μm	3 h : ~9,000 @ 10 kHz 24 h : ~280,000	2
1060°C (30 min ~ 24 h)	950°C - 24 h	30 min ~ 6 h : ~2-3 μm 9 h : mixed with ~2-3 μm and ~150 μm 12 ~24 h : ~150 μm	30 min ~ 6 h : ~4,000 @ 1 kHz 9 h : ~50,000 12 h : ~78,000 24 h : ~88,000	6
1050°C (10 ~ 80 h)	800°C - 8 h	10 h : 10 μm 20 h : 26 μm 80 h : 51 μm	10 h : ~20,000 @ 1 kHz 20 h : ~40,000 80 h : ~60,000	7
980°C (30 min ~ 24 h)	950°C - 24 h	30 min ~ 24 h : ~2-3 μm	30 min : ~200 @ 1 kHz 2 h : ~1,400 6 ~ 24 h : ~2,000-3,000	6
1000 ~ 1150°C (3 h)	1000°C - 3 h	1025 ~ 1050°C (< ~10 μm) 1075 ~ 1125°C (> ~10 μm)	1025°C : ~5,000 @ 1 kHz 1050°C : ~6,000 1075°C : ~30,000 1100°C : ~28,000 1125°C : ~66,000	8
925 ~ 1150°C (10 h)	900°C - 10 h	975°C : 4.75 μm 1150°C : ~ 80 μm	975°C : ~4,000 @ 1 kHz 1000°C : ~17,000	9

Table 2.3 Summary for the detailed deposition conditions and dielectric properties of polycrystalline CCTO films by PLD

Deposition method (substrate)	Deposition temperature (°C)	Oxygen partial pressure (mTorr)	ϵ_r values (film thickness)	References
PLD (Pt/Ti/SiO ₂ /Si)	700	200	~1000~2,500 @ 10 kHz (350nm)	15
PLD (LAO,STO)	720	200	~2,000 @ 10 kHz (600nm)	16
PLD (LAO)	800~850	160~200	~10,000 @ 1MHz (200nm)	17
PLD (Pt/Ti/SiO ₂ /Si)	450~700	20~200	~2,000 @ 10 kHz (480nm) ~700 @ 10 kHz (250nm)	18
PLD (Pt/Ti/SiO ₂ /Si)	720	200	~2,000 @ 10 kHz (480nm)	19
PLD (Pt/TiO ₂ /SiO ₂ /Si)	750	200	~1,000 @ 10 kHz (620nm)	20
PLD (LAO/Ag)	750	200~400	~12,000 @ 10 kHz (2.1 μ m)	21
PLD (LAO/SRO)	800	200	~600 @ 10 kHz (500nm)	22
PLD (STO,SRO)	500~800	10	~430 (230nm)	23
PLD (Pt/Ti/SiO ₂ /Si)	700	200	~1,500 @ 10 kHz (480nm)	24
PLD (Pt/TiO ₂ /SiO ₂ /Si)	700~800	800	~300~2,000 @ 10 kHz (500nm)	25
PLD (Pt/TiO ₂ /SiO ₂ /Si)	720	200	~1,700 @ 10 kHz (410nm) ~600 @ 10 kHz (610nm)	26
PLD (Pt/Ti/SiO ₂ /Si)	650	none	~1,000 @ 10 kHz (500nm)	27
PLD (Pt/Ti/SiO ₂ /Si)	700	200	~2,400 @ 10 kHz (480nm)	28

Table 2.4 Summary for the detailed deposition conditions and dielectric properties of polycrystalline CCTO films by sol-gel and sputtering

Deposition method (substrate)	Deposition temperature (°C)	Oxygen partial pressure (mTorr)	ϵ_r values (film thickness)	Reference
Sol-gel (Pt/TiO ₂ /SiO ₂ /Si)	700	In air (RTP)	~1,300 @ 100 Hz (180nm) ¹	29
(LNO/Pt/TiO ₂ /SiO ₂ /Si)			~2,000 @ 100 Hz (180nm) ²	
Sol-gel (Pt/Ti/SiO ₂ /Si)	750	In air (RTP)	~350~900 @ 100 kHz (500nm)	30
Sol-gel (Pt/TiO ₂ /SiO ₂ /Si)	650	In air (RTP)	~300 @ 10 kHz (135nm)	31
Sol-gel (Si)	700	In air (RTP)	None	32
Sol-gel (Pt/Ti/SiO ₂ /Si)	800	In air (RTP)	~300~700 @ 100 kHz (240~480nm)	33
Sol-gel (Pt/Ti/SiO ₂ /Si)	750	In air (RTP)	~1,500 @ 10 kHz (500nm)	34
Sputtering (Pt/Ti/SiO ₂ /Si)	RT → 700	40mTorr-Ar	None	35
Sputtering (Pt/Ti/SiO ₂ /Si)	500~700	In vacuum in N ₂ and O ₂	~600 @ 10 kHz (800nm)	36
Sputtering (Pt/TiO ₂ /SiO ₂ /Si)	650	In Ar+O ₂	~1,000 @ 10 kHz (50~400nm)	37
MOCVD (LAO)	600~900	Mixed gas in 3 Torr	None	38
MOCVD (Si)	750	Mixed gas in ~2 Torr	None	39

LNO=LaNiO₃, LAO=LaAlO₃, RTP=rapid thermal annealing

Table 2.5 Impedance characteristics at ~300 K for CCTO ceramics sintered at 1115°C for 1-24 h in air [3]

Sample	R_b (Ω)	R_{gb} (k Ω)	C_{gb} (nF)	f_{max} (Hz)
1 h	79 (± 5)	2100	0.76	100
3 h	70 (± 5)	4200	0.95	40
5 h	54 (± 5)	2600	1.22	50
8 h	35 (± 5)	150	26.53	40
24 h	30 (± 5)	180	35.37	25

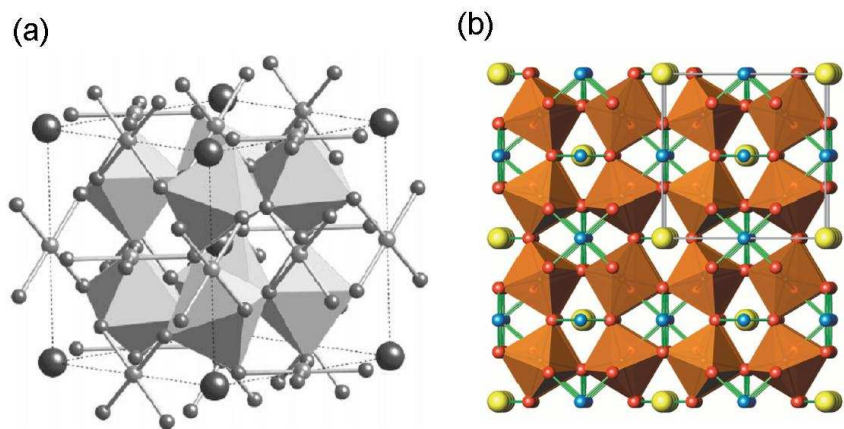


Fig. 2.1 The crystal structures of CCTO ceramics [1,13]

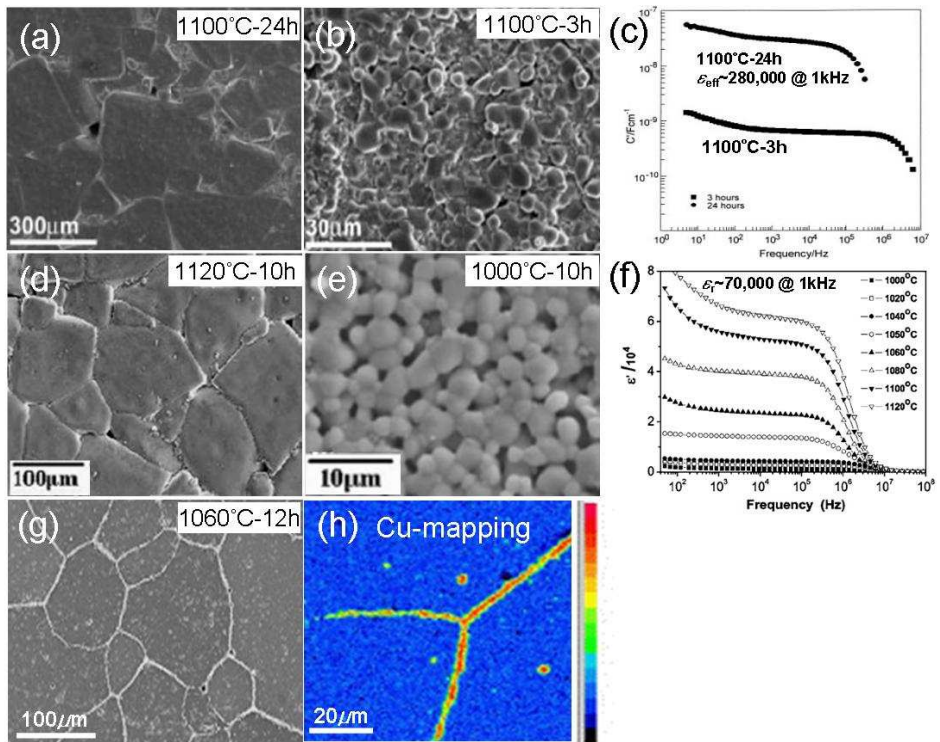


Fig. 2.2 The SEM images of abnormally grown large grains (a) and (d) and smaller-grains (b) and (e), and frequency-dependent ϵ_r properties of CCTO ceramics in ref 2 and 10, respectively. Fig. 2.2 (g) and (h) show the SEM image of abnormally grown large grains in CCTO ceramics sintered at 1060° C for 12 h in air and Cu-mapping image by EPMA, respectively, in ref [11]

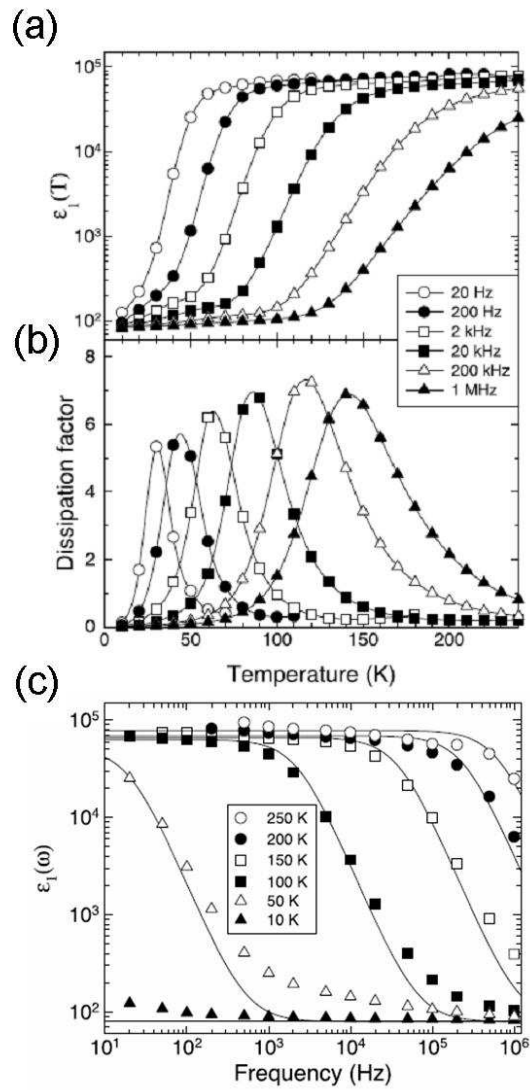


Fig. 2.3 Frequency and temperature-dependent dielectric properties of CCTO single crystals fabricated by traveling solvent zone technique [13]

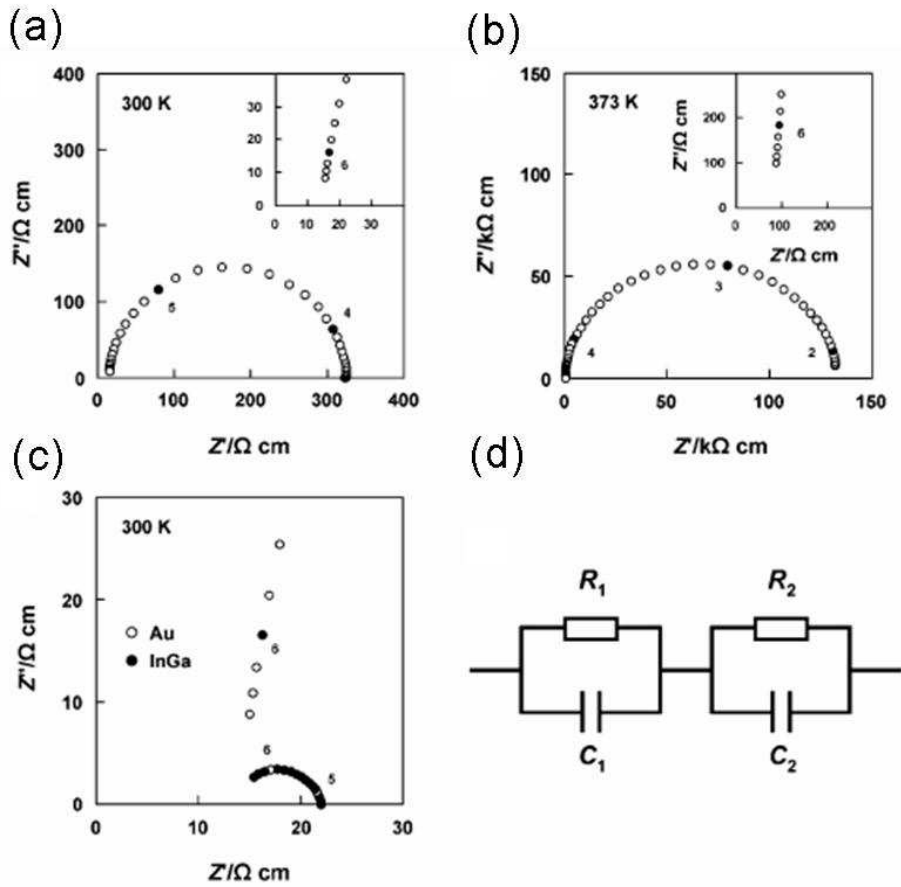


Fig. 2.4 Z^* plot for CCTO single crystal with Au electrode at 300 K (a), CCTO ceramic with Au electrode at 373 K (b), CCTO single crystal CCTO with InGa alloy electrodes at 300 K (c), and equivalent circuit used to model impedance spectroscopy data in CCTO single crystal and ceramic.[14]

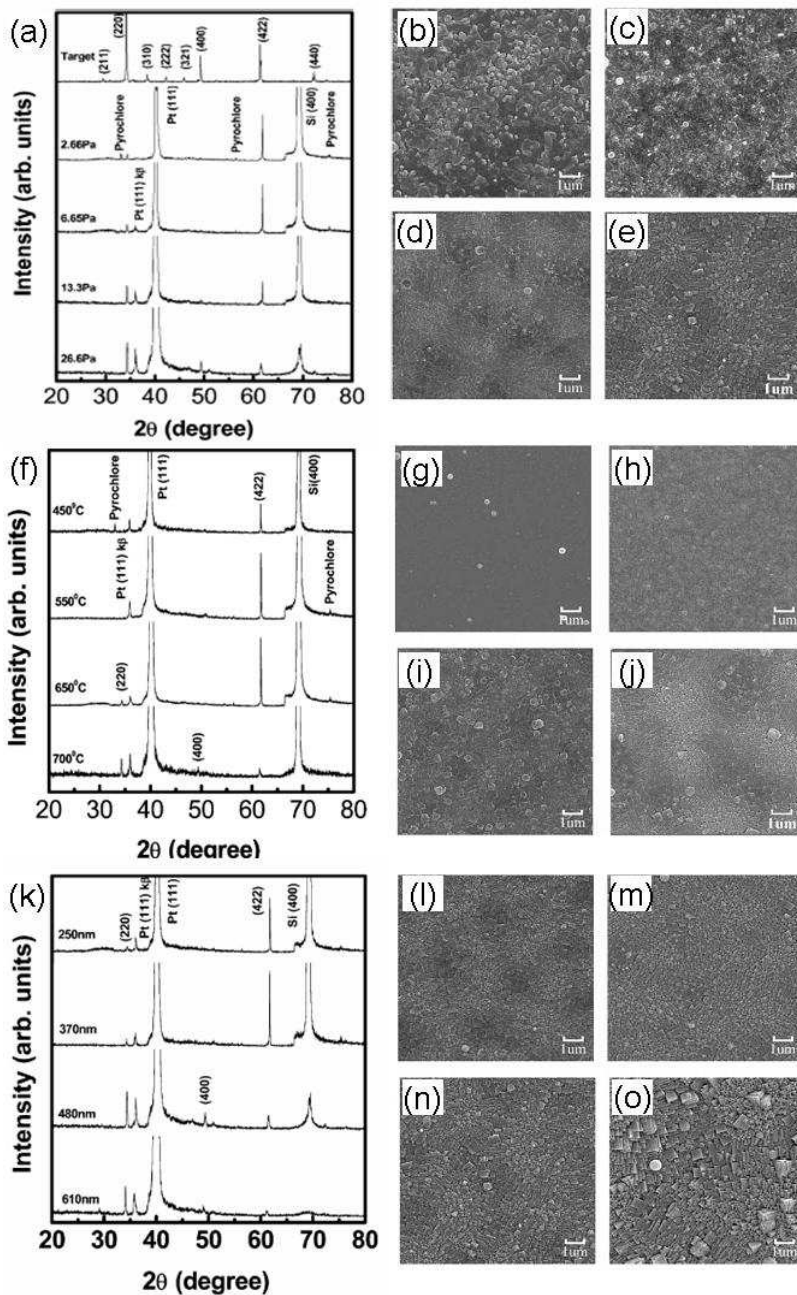


Fig. 2.5 The XRD patterns and SEM images of the microstructure in polycrystalline CCTO films fabricated by PLD. [18]

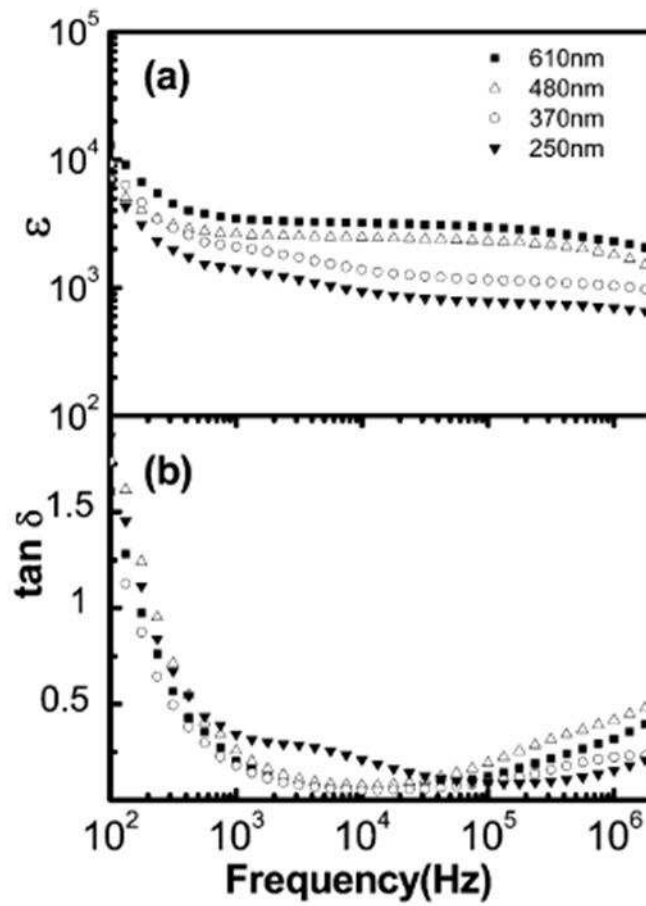


Fig. 2.6 The thickness-dependent dielectric properties of CCTO ceramics by PLD [18]

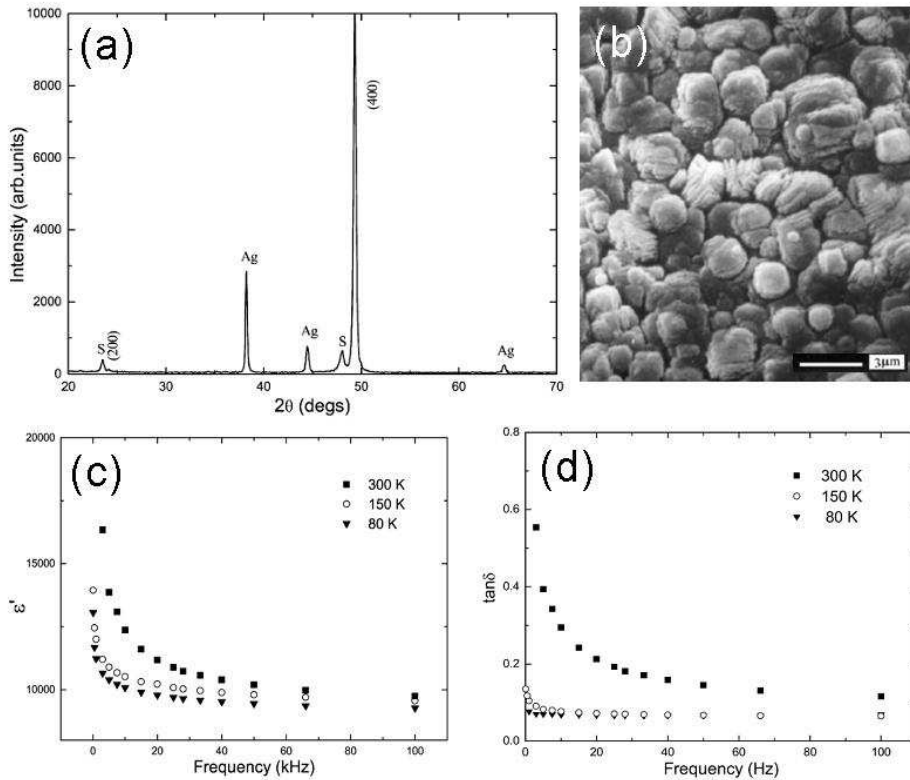


Fig. 2.7 The XRD pattern (a), surface morphology (b), and frequency-dependent dielectric properties (c) and (d) of 2 μm -thickness CCTO films by PLD. [21]

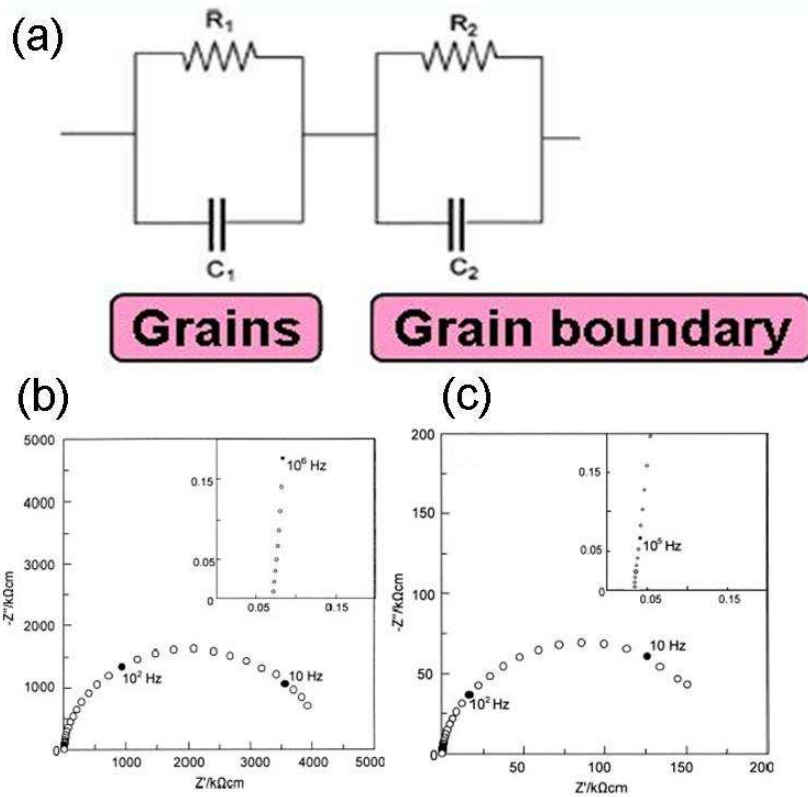


Fig. 2.8 The equivalent circuit of CCTO ceramics (a), Z^* spectroscopy for smaller-grained CCTO ceramics sintered at 1110° for 3 h in air (b), and larger-grained CCTO ceramics sintered at 1110°C for 24 h in air (c). [2]

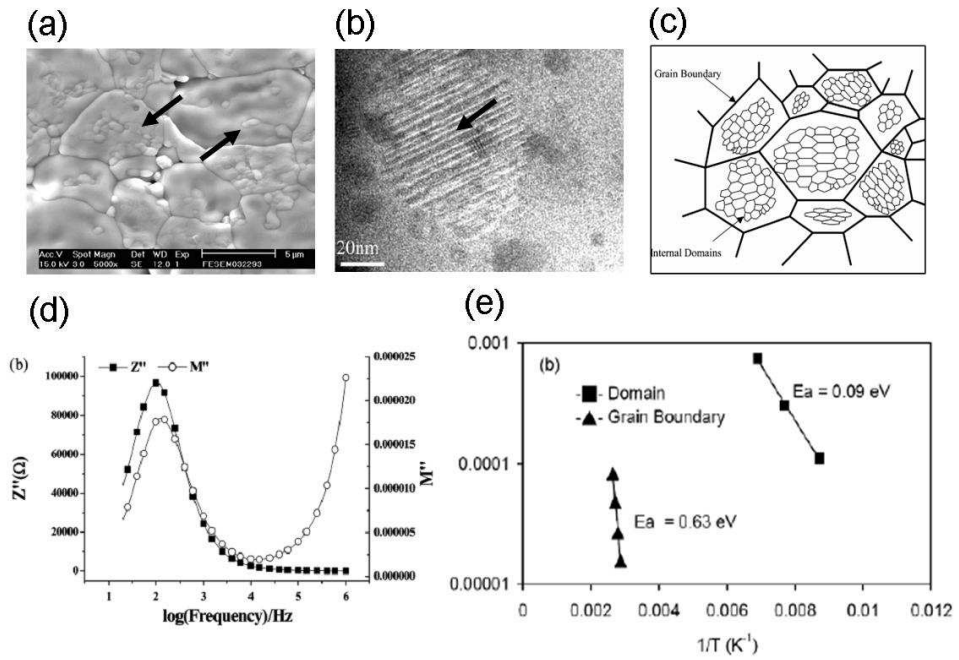


Fig. 2.9 SEM image of CCTO ceramic sintered at 1065°C for 20 in air (a) and TEM images of domain boundary in CCTO ceramics (b), microstructure model of CCTO ceramics (c), frequency-dependent Z'' and M'' properties of CCTO ceramics (d) in ref. [43], and domain and grain boundary activation energies (e) of CCTO ceramics in ref. [50]

Chapter 3. A study on the origin of high- k in $\text{CaCu}_3\text{Ti}_4\text{O}_{12}$ bulks

3.1. Introduction

Dielectric materials exhibiting high ϵ_r values and excellent temperature stability are indispensable for the electronic devices such as ceramic capacitor and dynamic random access memory. Recently, the cubic perovskite CCTO ceramics showing colossal dielectric response (CDR, $\epsilon_r > 10,000$) with no phase transition in a wide temperature range between 100-600 K has attracted a worldwide attention.[1] However, the ϵ_r values of CCTO ceramics are strongly dependent on the processing conditions such that a wide variety of ϵ_r values from ~ 200 to $\sim 280,000$ have been reported. Among various processing conditions, the sintering conditions including temperature and holding time are the most important processing parameters. For instance, Sinclair *et al.*[2] and Adams *et al.*[3-4] reported that the ϵ_r values of CCTO ceramics were increased from $\sim 9,000$ to $\sim 280,000$ at 10 kHz sintered at 1115°C with increasing the holding time from 3 to 24 h, respectively. In addition, Yoo *et al.*[5] reported that the ϵ_r values were increased from $\sim 3,000$ to $\sim 90,000$ at 1 kHz with increasing the sintering temperature from 980 to 1060°C for the same holding time of 12 h. Thus, it is quite important to understand the effects of the sintering condition on the microstructures and dielectric properties of CCTO ceramics. However, within the best of our knowledge, an overall relationship among the sintering

conditions, microstructures, and dielectric properties of CCTO ceramics has never been reported in the literature yet.

On the other hand, many research groups have tried to unveil the physical origin of CDR in CCTO ceramics. Thus, numerous mechanisms such as grain boundary IBLC model,[2-4, 6-8] domain boundary IBLC model,[9-11] sample-electrode interface effects,[12] and twin boundary effects[13-14] have been suggested for the origin of CDR in CCTO ceramics. Recently, Ferrarelli *et al.*[12] have suggested that CDR in CCTO ceramics and single crystals originated from the grain boundary IBLC model and a non-ohmic interface effect, respectively. Therefore, definite understandings for the origin of high- k in CCTO ceramics and single crystals are still in absent.

In order to understand the origin of CDR in CCTO ceramics, we have systematically investigated the effects of sintering conditions on the microstructures and dielectric properties of CCTO ceramics in this study. Furthermore, the electrical properties of grain and grain boundaries in CCTO ceramics were quantitatively identified using Z^* and M^* spectroscopy. Finally, the mechanism of CDR in CCTO single crystals was successfully clarified by investigating the effect of electrode on the dielectric properties of CCTO single crystals.

3.2 Experimental

The CCTO polycrystalline ceramics were fabricated by solid state reaction using CaCO_3 (Cerac, 99.95%), CuO (High Purity Chemicals,

99.99%) and TiO₂ (High Purity Chemicals, 99.99%). The mixed powder was ball-milled in ethyl alcohol using a polyethylene bottle with ZrO₂ balls for 24 h, and then uniaxially pressed into pellets and calcined at 950°C for 24 h in air. The as-calcined pellets were ball-milled for 24 h and further consolidated by cold isostatic pressing with 100 MPa. The samples were sintered in air at various sintering temperatures and holding times from 980 to 1080°C for 12 h and from 30 min to 24 h at 980 and 1060°C, respectively. The microstructure of CCTO ceramics was observed by scanning electron microscopy (SEM, JSM-5600) after the thermal etching process at 900°C for 1 h in air. The segregated second phase at grain boundary in CCTO ceramics was identified using energy dispersive spectroscopy (EDS) analysis attached to the SEM. For electrical measurement, Ag electrode was coated on polished CCTO ceramics using screen printing method and fired at 600°C for 1 h in air. The frequency-dependent dielectric constant, ϵ_r and dielectric loss, $\tan\delta$ were measured by an impedance/gain-phase analyzer (HP 4194a) in the frequency range of 10² Hz to 15 MHz with an oscillation voltage of 500 mV. The Z^* and M^* spectroscopy analyses for identifying the resistivity (ρ) and C values of grain and grain boundary were performed using Solatron 1260 and Agilent E4991a at relatively low frequency region (10⁻² ~ 10⁵ Hz) and high frequency (10⁶ Hz ~ 1 GHz) region, respectively. All data from Z^* and M^* spectroscopy were obtained using the equivalent circuit with two parallel R and C elements of grain and grain boundary. The activation energies of grain and grain boundary were obtainable by measuring the real and imaginary part of Z^* under the various measuring temperatures ranging from RT to 300°C.

3.3 Results and discussion

3.3.1 High- k mechanisms for CCTO ceramics

As previously reported by many research groups, the ϵ_r values in CCTO ceramics are strongly dependent on the microstructures and sintering conditions. Prior to clarify the mechanism for high- k in CCTO ceramics, the overall relationship among sintering conditions, microstructures, and dielectric properties of CCTO ceramic should be identified. Fig. 3.1 shows the frequency-dependent ϵ_r and $\tan\delta$ properties of CCTO ceramics sintered at various temperatures ranging from 980 to 1080°C for 12 h. An abrupt increase in ϵ_r values from ~3,000 to ~170,000 below 1 kHz is clearly observable in samples sintered at 980 and 1000°C, respectively. Then the ϵ_r values are systemically decreased to ~150,000, ~77,000, ~76,000, and ~69,000 at 1020, 1040, 1060, and 1080°C at the same frequency, respectively. The SEM micrographs for these samples are shown in Fig. 3.2. It can be seen that the ϵ_r values are strongly related to their microstructures. While only the sintered density of the CCTO ceramics is increased without a significant increase in the average grain size at the sintering temperature of 980°C with increasing holding time from 30 min to 24 h,[5] an abnormal grain growth occurs at the sintering temperature of 1000°C as shown in Fig. 3.2(b), which is accompanied by the abrupt increase in the ϵ_r values (Fig. 3.1). However, the ϵ_r values are slightly decreased from ~170,000 to ~150,000 at 1 kHz with further increasing the sintering temperature from 1000 to 1020°C, which might be due to the presence of small-grained regions indicated by arrows in Fig. 3.2(c) because their sintered densities

(~98 %) and average grain sizes (~300 μm) was almost identical. Compared with the average grain size of the samples sintered at 1000 and 1020°C, those of the samples sintered at the region of 1040 ~1080°C were greatly reduced to ~150 μm , which might originate from a reduced number of abnormal grain sites at relatively higher sintering temperatures. From Fig. 3.1(b), one can observe that the maximum $\tan\delta$ value near 10 MHz in CCTO ceramic sintered at 980°C is relatively lower than those of samples sintered at higher temperatures. The variation of $\tan\delta$ values in our samples are in good agreement with previous reports by other research groups. For instance, Yuan *et al.*[15] and Ni *et al.*[16] reported that the $\tan\delta$ values of CCTO ceramic sintered at 975 and 1025°C were ~1.5 at 10 MHz and ~0.2 at 1 MHz, respectively, and these values were lower than those of samples sintered at relatively higher temperatures. In our samples, the abrupt increase in $\tan\delta$ values at the frequency near 10 MHz are obviously related to a severe drop in the ϵ_r values.

Meanwhile, the abnormal grain growth in the CCTO ceramics was also observable when the holding time was varied at a fixed sintering temperature higher than 1000°C. As a representative, the microstructure variation in the CCTO samples is displayed as a function of the holding time at 1060°C in Fig. 3.3. As shown in Fig. 3.3 (a) and (e), the CCTO ceramic sintered at 1060°C for 3 h consists of small grains (< ~5 μm) with a segregated second phase at grain boundary after a thermal etching at 900°C for 1 h. The segregated second phase is regarded as a copper-oxide phase according to the EDS analyses for the grain boundary region. As shown in Fig. 3.3 (b) and (f), a small amount of abnormally grown large CCTO grains

appears in the sample sintered for 6 h, of which grains show a flat interface structure. Then, both the population density and the average size of these grains are significantly increased, and some large grains start to interconnect in Fig. 3.3 (c) and (g). Finally, the CCTO samples sintered for 12 h consist of abnormally grown large grains ($\sim 150 \mu\text{m}$) with segregated copper-oxide at the grain boundary as shown in Fig. 3.3 (d) and (h). Longer holding time than 12 h shows no apparent variation in the microstructure. In accordance with this microstructure evolution, Kim *et al.*[17] insisted that the flat interface of grains played the key role for inducing the abnormal grain growth in the CCTO ceramics. Since relatively higher energy is required for a nucleation of faceted grains compared with spherical grains, a limited number of large grains might grow rapidly. The dielectric properties of these CCTO samples are represented in Fig. 3.4 (a) and (b). For a comparison, the dielectric properties of the CCTO samples sintered at 980°C are also presented as a function of the holding time in Fig. 3.4(c) and (d). In Fig. 3.4 (a), while the ϵ_r values of samples sintered for the holding time up to 6 h are almost unaltered ($\sim 3,000$ at 1 kHz), the ϵ_r values are abruptly increased to $\sim 42,000$ for 9 h and further increase up to $\sim 88,000$ for 24 h. In addition, the maximum $\tan\delta$ values near 10 MHz are increased with increasing the holding time in Fig. 3.4 (b). In contrast to these results, the CCTO ceramics sintered at 980°C with various holding times ranging from 30 min to 24 h shows no abnormal grain growth (see Fig. 3.3(a) and (b) in ref.[5]). The samples sintered at 980°C consisted of uniformly distributed small grains (average grain size $< \sim 5 \mu\text{m}$) irrespective of the holding time, whereas the relative sintered density was highly increased from ~ 82 to ~ 98 % with

increasing the holding time (see Fig. 2 in ref.[5]). Although the high relative sintered density of ~98 % was obtainable at lower sintering temperature of 980°C, the average grain size was much smaller than those of the samples sintered at 1060°C for the holding time longer than 9 h, and thus led to relatively lower ϵ_r values ($< \sim 4,000$ at 1 kHz) in Fig. 3.4 (c) and (d).

On the basis of the above results, we could understand an overall relationship among sintering condition, microstructure, and dielectric property of the CCTO ceramics as follows; First, while the abnormal grain growth in CCTO ceramics is not observable at the sintering temperature lower than 980°C with the holding times up to 24 h, the abnormally grown large grains start to occur at the sintering temperature higher than 1000°C after a certain holding time. Second, the CCTO ceramics with no abnormal grain growth show the relatively low ϵ_r values ($< \sim 5,000$) at 1 kHz irrespective of their relative sintered density. Finally, the CCTO ceramics consisting of a large population density of abnormally grown large grains show very high ϵ_r values over 10,000 at 1 kHz. In accordance with our results from the CCTO samples sintered at 1060°C with various holding times ranging from 30 min to 24 h, Adams *et al.*[4] reported that the CCTO ceramics fabricated at sintering temperature of 1115°C with holding times from 1 to 24 h showed the abnormal grain growth with the flat interface structure from the holding times of 5 h, and then the sample sintered for 24 h was composed of almost fully abnormally grown large grains with the average grain size of $\sim 300 \mu\text{m}$. The abrupt increase in grain boundary C values of 26.53 nF were obtainable from the holding times of 8 h and the values were increased up to 35.37 nF with the holding time of 24 h. The

abnormal grain growth and abrupt increase in grain boundary C values start to occur with the somewhat shorter holding time of 5 h and 8 h compared to those of our 6 h and 9 h, respectively. These discrepancies could be originated from their relatively higher sintering temperature of 1115°C compared with 1060°C.

Several research groups have investigated the effect of the sintering temperatures ranging from 1000 to 1150°C on the microstructures and dielectric properties of CCTO ceramics. For instance, Shao *et al.*[18] fabricated the CCTO ceramics at the various sintering temperatures between 1000 and 1130°C for 10 h and observed that the average grain size was increased from several μm to $\sim 100 \mu\text{m}$. They reported that the ϵ_r values systemically increased from $\sim 1,200$ to $\sim 70,000$ at 1 kHz with increasing the sintering temperatures. However, no abnormal grain growth was observable at the sintering temperature of 1000°C. Instead, the abnormally grown large grains ($\sim 100 \mu\text{m}$) appeared at the sintering temperature of 1060°C so that the abruptly increased ϵ_r value from $\sim 1,200$ to $\sim 25,000$ at 1 kHz was achievable at the sintering temperature of 1060°C. These discrepancies with our results might be due to their lower calcination temperature of 650°C and shorter holding time of 8 h compared with those of our calcination temperature of 950°C and holding time of 24 h, respectively. In addition, Ni *et al.*[16] employed the sintering temperatures ranging from 1000 to 1150°C with the holding time of 3 h for fabricating the CCTO ceramics and obtained the ϵ_r values of $\sim 5,000$ at 1 kHz between 1025 and 1060°C. These ϵ_r values are quite similar to those of our ϵ_r values ($< \sim 5,000$ at 1 kHz) obtained at 1060°C with the same holding time of 3 h. Moreover, the ϵ_r values of $\sim 30,000$ at 1

kHz in sample sintered at 1075°C are smaller than those of ~69,000 in our sample sintered at 1080°C at the same frequency, of which result is attributable to incomplete abnormal grain growth due to shorter holding time of 3 h compared with 12 h in our study. Therefore, referring to the effects of the holding time on the microstructures and dielectric properties of the CCTO ceramics fabricated at 1060°C in our investigation, the relatively lower ϵ_r values of ~30,000 at 1 kHz could be increased if the holding time is prolonged over 3 h.

Contrary to our results, remarkably smaller grain size and lower ϵ_r values in CCTO ceramics were reported by some research groups. For instance, Cao *et al.*[19] fabricated the CCTO ceramics at the sintering temperatures ranging from 1000 to 1100°C for 24 h and reported significantly smaller grain size (3 to 16 μm) and lower ϵ_r values (~1,000 to ~14,000 at 1 kHz) compared to those of our samples sintered at the region of 980 ~ 1080°C for 12 h. In addition, Fang *et al.*[20] reported that the CCTO ceramics sintered at 1035 and 1065°C with various holding times from 0 to 20 h showed the average grain size from ~5 to ~20 μm with ϵ_r values from ~4,000 to ~20,000. Although, the samples sintered at 1035 and 1065°C with the holding times up to 8 and 2 h, respectively, showed the ϵ_r values comparable to that of our sample (~3,000 at 1 kHz) sintered at 1060°C for 3 h, the samples with increasing holding times up to 20 h showed relatively lower ϵ_r value (~20,000 at 1 kHz) compared to that of our sample (~88,000 at 1 kHz) sintered at 1060°C for 24 h. At this stage, the reasons for the remarkably smaller average grain size and lower ϵ_r values in CCTO ceramics fabricated by the above two research groups are unclear. We simply

speculate that these results might be related to a difference in the calcination process since Cao *et al.*[19] performed the calcination process for three times at 1000°C for 12 h and Fang *et al.*[20] adopted somewhat short holding time of 2 h at 950°C for the calcination. Since the Z^* and M^* spectroscopy are useful techniques for separating grain from grain boundary properties of materials[12, 21] many groups[2-4, 6, 9, 13, 20] have analyzed the CCTO ceramics by these techniques. For instance, on the basis of the C_g and C_{gb} values in CCTO ceramics measured by Z^* spectroscopy, Sinclair *et al.*[2] argued that extremely high ϵ_r values of ~280,000 at 10 kHz in CCTO ceramics with abnormally grown large grains originated from a high C_{gb} values. Adams *et al.*[3-4] also reported the Z^* analysis data of CCTO ceramics which revealed that the C_{gb} values of CCTO ceramics sintered at 1115°C monotonously increased from 0.76 to 35.37 nF with increasing the holding time from 1 to 24 h. These results commonly suggest that CDR in CCTO ceramics originates from the two different extrinsic sources of grain boundary and/or intragranular resistive regions such as domain boundary and twin boundary.

The grain boundary IBLC model is the most widely accepted for the explanation of the CDR origin in CCTO ceramics.[2-4, 6-8] According to this model, CCTO ceramics are electrically heterogeneous and consist of conducting grains and insulating grain boundaries, and hence the grain boundary of CCTO ceramics showing high R and C values can act as an extrinsic source for high ϵ_r values.[22] Although there have been numerous reports on CCTO ceramics supporting the validity of grain boundary IBLC model, more supplemental analyses are still required. Therefore, in order to

identify the origin of various ε_r values in CCTO ceramics, we also performed Z^* and M^* spectroscopy analyses to evaluate the R and C values of both grain and grain boundary using the following equations,

$$M^* = j\omega C_0 Z^* = M' + jM'' \quad (1)$$

$$Z''_{\max} = \frac{R}{2}, \quad M''_{\max} = \frac{C_0}{2C} \quad (2)$$

$$\omega\tau = \omega RC = 2\pi f_{\max} RC = 1 \quad (3)$$

,where Z''_{\max} and M''_{\max} is the peak of imaginary part of Z^* and M^* spectroscopy, respectively, $C_0 = \varepsilon_0(A/t)$, where ε_0 is the permittivity of free space (8.854×10^{-14} [F/cm]), A is the area of electrode, t is the sample thickness, f_{\max} is the top of arc in Z^* spectroscopy and ω is the angular frequency. The Z^* and M^* spectroscopy data for the CCTO samples sintered at various temperatures ranging from 980 to 1080°C for 12 h are represented in Fig. 3.5. As shown in Fig. 3.5 (b) and (c), the frequency dependent imaginary parts of Z^* and M^* spectroscopy data for the CCTO samples with relatively higher ε_r values exhibit lower M'' peaks near 10^1 Hz than other samples with lower ε_r values, representing that their C_{gb} values are relatively higher than those of other samples. However, except the sample sintered at 1080°C, the ρ_{gb} values in small-grained sample sintered at 980°C are higher than those of large-grained samples as shown in Fig. 3.5(a) ~ (e). The ρ_g , ρ_{gb} , C_g , and C_{gb} values were evaluated from these data by using equations (1)-(3) and summarized in Table 3.1. The ρ_g and C_g values of all CCTO samples are obtainable from the peaks of imaginary parts in Z^* and M^* spectroscopy

data at ~ 1 GHz region (not shown). In Table 3.1, an abrupt increase in C_{gb} values with increasing the sintering temperature from 980 to 1020°C is clearly observable. Moreover, the two samples sintered at 1000 and 1020°C show the relatively higher C_{gb} values of 944,562 and 1,131,869 pF/cm, respectively, compared with those of other samples sintered at the region of 1040~1080°C.

As previously mentioned, larger ϵ_r values were achieved from the CCTO samples with larger average grain size of CCTO. Interestingly, larger-grained CCTO samples possess larger C_{gb} values, which are also in good agreement with previous reports.[2-4] In contrast, the ρ_{gb} values of larger-grained CCTO ceramics are lower than those of smaller-grained samples less than 20 %. The ρ_g values are decreased from 365 to 42.8 Ωcm while the C_g values are increased from 177 to 333 pF/cm, respectively, with increasing the sintering temperature from 980 to 1080°C. The origin of remarkably higher electrical conductivity in larger-grained CCTO samples compared with those of smaller-grained is unclear at the moment, and thus further investigation is under progress.

Fig. 3.6 shows the Arrhenius plots of ρ_g and ρ_{gb} of CCTO ceramics sintered at various temperatures ranging from 980 to 1080°C for 12 h. It is shown that the ρ_{gb} values are larger than those of grains at a given measuring temperature. It is also shown that the ρ_{gb} values are more rigorously decreased with measuring temperature compared with the ρ_g values, and thus their differences become negligibly small at ~ 600 K. As shown in Fig. 3.6, all the ρ_g and ρ_{gb} values obey the Arrhenius law, and the activation energies from grain and grain boundary show the similar values of ~ 0.1 and ~ 0.8 eV,

respectively, which is irrespective of the sintering temperatures. The activation energies were obtained from the equation of $\rho \sim \exp(-E_a/k_B T)$, where E_a , k_B , and T are the activation energy, the Boltzmann constant, and the absolute temperature, respectively. These results show a strong consistency with previous reports by Adams *et al.*[4] but the activation energies of grain and grain boundary in our samples are slightly higher than their values of ~ 0.06 and ~ 0.6 eV for grain and grain boundary, respectively. This discrepancy might be due to a difference in sintering conditions. The C_g values at room temperature are remarkably smaller than those of C_{gb} and much less temperature dependent as shown in Table 1 and Fig. 3.6. Similarly, the ε_r values in CCTO ceramics sintered at 1060°C for various holding times from 30 min to 24 h show also a strong dependency on the electrical properties of grain boundary as shown in Fig. 3.7. In Fig. 3.7, the CCTO samples sintered for 3 to 6 h show relatively high M'' values, implying that the C_{gb} values in smaller-grained samples in Fig. 3.7 (a) and (b) are relatively smaller than those of larger-grained samples in Fig. 3.7 (c) and (d), whereas the ρ_g values in smaller-grained samples are relatively higher than those of larger-grained samples. The quantitative ρ_g , ρ_{gb} , C_g , and C_{gb} values in CCTO ceramics are represented in Table 3.2. In this table, the C_{gb} values of the samples sintered at 1060°C for 3 and 6 h are almost identical to those of the sample sintered at 980°C for 12 h in Table 3.1, which might be due to the similar ε_r values in both samples. However, the C_g values of samples sintered at 1060°C for 3 and 6 h are about two times higher than that of sample sintered at 980°C for 12 h. This discrepancy might originate from the different electrical properties of intragranular resistive regions in each grain

of samples. Detailed investigations using admittance spectroscopy and high resolution transmission electron microscopy are required for further identification. Like the CCTO samples sintered at various temperatures ranging from 980 to 1080°C for 12 h, the C_{gb} values are increased from ~15,000 to ~324,000 pF/cm with increasing holding time from 3 to 12 h at 1060°C, implying that the relatively high ϵ_r values in samples with abnormally grown large grains were attributable to the high C_{gb} values. In addition, the CCTO ceramics with abnormal grain growth over the holding time of 9 h show relatively lower $\rho_{g,b}$ values than those of small-grained CCTO samples. The ρ_g values and C_g values are gradually decreased from 342 to 36 Ωcm and from 340 to 168 pF/cm, respectively, with increasing holding time.

In accordance with our results, Adams *et al.*[3] suggested that the impedance data of CCTO ceramics could be analyzed using a simplified equivalent circuit consisting of two parallel RC elements of conducting grains, R_gC_g and insulating grain boundary, $R_{gb}C_{gb}$ connected in series. In their study, large-grained CCTO ceramics sintered at 1100°C for 24 h showed relatively higher ϵ_r and C_{gb} values of 280,000 and ~25 nF/cm, respectively, compared to those of ~9,000 and ~0.8 nF/cm for small-grained sample sintered at 1100°C for 3 h. In contrast, large-grained CCTO sample showed relatively lower R_{gb} value of 0.18 $M\Omega\text{cm}$ compared to the value of ~4.2 $M\Omega\text{cm}$ in small-grained sample. Although, the origin for this variation in R_g values with increasing holding time and conducting behaviors in each grain are absent in their study, it can be suggested that their ϵ_r values might be dominantly affected by the electrical properties of grain boundary.

Meanwhile, the grain boundary IBLC model has been doubted because of the CDR in a CCTO single crystal without grain boundary. Therefore, an alternative mechanism for supporting the CDR in both CCTO ceramics and single crystal has been introduced by several research groups.[9,18,20,23-27] According to these research groups, the extremely high ϵ_r values appeared in single crystal CCTO are not originated from the high capacitive grain boundary but from the presence of domain boundaries or twin boundaries within CCTO grains and single crystals. Fang *et al.*[9,20] have investigated the effects of sintering conditions on the microstructures and dielectric properties of CCTO ceramics. In their reports, the abnormal grain growth was also observable in the samples sintered at 1065°C with holding times from 3 to 20 h. However, additional subgrains with the size of less than 2 μm appeared inside of each grain after thermal etching process at 960°C for 72 min. They insisted that these subgrains were more apparently observable within abnormally grown large grains. Based on the data obtained by the Z^* spectroscopy, they suggested that the CCTO ceramics should consist of three different regions of domains, domain boundaries, and grain boundaries, and thus the CDR was dominantly originated from the resistive domain boundary. However, we argue that the assignment of these three different regions should be modified due to the following reasons. First, the activation energies of domain (0.09 eV) and grain boundary (0.47~0.63 eV) are quite similar to those of previously reported values of grain (0.06 eV) and grain boundary (~0.6 eV) by several research groups. [2,4,19,22,28-29] Second, the activation energy of domain boundary is absent in Fig. 9 of ref.20 due to the high impedance of domain boundary under the measuring

temperature region ranging from RT to 100°C. However, measurement should be performed in wider measuring temperature region to support that the dielectric relaxation behavior of domain boundary is responsible for the CDR in CCTO ceramics. Finally, they should assign the peaks of Z^* and M^* observed at $\sim 10^2$ Hz in Fig. 5 of ref.[9] as the domain boundary response because the most resistive region is generally presented at relatively lower frequency region in the Z^* and M^* spectroscopy analyses. Therefore, the CDR could not be dominantly originated from these subgrains due to above three reasons. In addition, the subgrains have not been frequently observable in other research groups, and the calcination time for 2 h in their study could be somewhat shorter than compared other research groups so that the abnormal grain growth of CCTO might not be fully developed. Shao *et al.* [18,25] also insisted that CCTO ceramic could be consisted by the same three regions but the activation energy of 0.66 eV observed at middle-frequency region in Fig. 7 of ref.[18] was quite similar to that of conventionally reported activation energies of grain boundary.[4,6]

Contrary to the grain boundary and domain boundary IBLC model, Li *et al.*[13] stressed that CDR in both CCTO ceramics and single crystal could be attributed to the presence of internal resistive layer such as twin boundary. For a CCTO single crystal, they reported two different activation energies of 0.24 and 0.087 eV for the crystal defects of twin boundaries and grains, respectively. However, referring to the quantitative C_g values in Table 3.1 and 3.2 from our CCTO samples, one can observe that these values are significantly lower than the C_{gb} values. Thus, it must be

inappropriate to designate the twin boundaries as the origin of CDR in the CCTO single crystal.

3.3.2 High- k mechanism for CCTO single crystals

Ferrarelli *et al.*[12] have suggested, the origin for CDR in CCTO ceramics and single crystals may be unidentical so that high capacitive grain boundary and non-ohmic contact effect between sample and electrode are responsible for CDR in ceramics and single crystals, respectively. As previously mentioned, the origin for CDR in CCTO ceramics is attributable to the high C values of grain boundary so that we fabricated a CCTO single crystals by the flux method and measured its dielectric properties for clarifying the mechanism for CDR in CCTO single crystal. The detailed processing conditions for synthesizing CCTO single crystals are reported in elsewhere.[30] We adopted various electrodes of Ag, Au, and InGa for investigating the effects of electrodes on the dielectric properties of both CCTO ceramics and single crystals. As shown in Fig. 3.8, no remarkable variations of the ϵ_r and $\tan\delta$ values are observable depending on the electrodes in CCTO ceramics although slightly higher ϵ_r and $\tan\delta$ values are observed in the sample with InGa electrode due to the relatively lower contact resistance at the interface between sample and electrode. For identifying the quantitative ρ_{gb} and C_{gb} values in the CCTO ceramics with various electrodes, we investigated the frequency-dependent Z'' and M'' properties and obtained the values using the equation (2). Figure 3.9 and Table 3.3 show the frequency-dependent Z'' and M'' spectroscopy and calculated ρ_{gb} and C_{gb}

values using equation (2). As shown in Fig. 3.9, the frequencies for Z''_{\max} and M''_{\max} are almost same but the maximum Z'' and M'' values are different in all samples. These results imply that the contact resistance should exist at the interface between samples and electrodes so that relatively higher ρ_{gb} and C_{gb} values are observed in the samples with Ag and Au electrodes compared to that of sample with InGa electrode in Table 3.3.

Meanwhile, frequency-dependent dielectric properties of CCTO single crystals with numerous electrodes of Ag, Au, and InGa are also investigated and presented in Fig. 3.10. In Fig. 3.10(a), the ϵ_r and $\tan\delta$ values in CCTO single crystal with Ag electrode are comparable to those of CCTO ceramics. However, the two values in the samples with Au and InGa electrodes show peculiar phenomena at relatively lower frequency region of $< \sim 1$ kHz, and the ϵ_r values of $\sim 20,000$ at 1 kHz in the two samples are much lower than those of CCTO ceramic at the same frequency. At this stage, the reason for the presence of peculiar ϵ_r and $\tan\delta$ values are unclear but it could be related to the contact resistance at interface between samples and electrodes since no grain boundaries are observable in single crystals and low frequency response is strongly dependent on the interface state between sample and electrodes. The contact resistance of sample with Ag electrode is about 80 k Ω because the non-zero intercept on the Z' axis at low frequency indicated by arrow is ~ 81 k Ω in the cole-cole plot of Fig. 3.10(c). In addition, the peak of Z'' value at $\sim 10^3$ Hz are ~ 37 k Ω in the frequency-dependent Z'' properties in Fig. 3.10(d), implying that the contact R value between sample and Ag electrode is about ~ 74 k Ω by equation (2). In contrast to these results, the contact R values between CCTO single crystals and electrodes of Au &

InGa should be remarkably lower than that of sample with Ag electrode. Because the semi-circles in the Fig. 3.10(c) indicated by blue and red arrows are negligibly small compared to that of Ag electrode and no peaks are observable in the frequency-dependent Z'' properties in Fig. 3.10 (e) and (f). Therefore, ohmic contact could be formed at the interface between CCTO single crystal and Au & InGa electrodes.

On the basis of the above results in Fig. 3.10, the high- k in CCTO single crystals with Ag electrode is attributable to the high contact R value of ~ 80 k Ω between samples and electrodes. We tried to reconfirm the mechanisms for high- k in CCTO ceramics and single crystals by investigating the I - V characteristics under DC bias condition. As shown in Fig. 3.11(a) and (b), non-linear I - V characteristics are obtainable in the CCTO ceramics irrespective of electrodes and CCTO single crystal with InGa electrode. The non-linear behaviors in the above samples are originated from the high C_{gb} values and contact R values, respectively, as previously confirmed in Fig. 3.9 and 3.10, respectively. However, ohmic conduction is observed in the CCTO single crystal with InGa electrode, implying that the mechanism for CDR in CCTO ceramics and single crystals should be different. The bulk resistivity of CCTO single crystal is obtained to 26.64 Ω by measuring the slope of I - V behavior in the sample with InGa electrode and sample geometries using two probe method in Fig. 3.11(c). Moreover, the value could be also calculated by the slope of I - V characteristics in the sample with Ag electrode using four probe measurement in Fig. 3.11(d) since the effects of contact resistance could be ignored in four probe technique.

Consequently, it could be concluded that the high C_{gb} values and high contact R values between samples and electrode are the origin for high- k in CCTO ceramics and single crystals, respectively.

3.4 Summary

In the present study, we tried to unveil the mechanisms for high- k in CCTO ceramics and single crystals. For this purpose, we carefully investigated the effects of sintering temperatures and holding times on the microstructures and dielectric properties of CCTO ceramics. In addition, we tried to identify the effects of various electrodes (Ag, Au, and InGa) on the dielectric properties of CCTO single crystals. The homogeneously distributed small grains ($\sim 5 \mu\text{m}$) in the sample sintered at 980°C for 12 h were changed into abnormally grown large grains ($\sim 300 \mu\text{m}$) in the sample sintered at 1000°C . However, the average grain size of samples was decreased to $\sim 150 \mu\text{m}$ with further increase in sintering temperatures up to 1080°C . The ϵ_r values in the samples showed strong dependence on the microstructure. The remarkably increased ϵ_r values from $\sim 1,200$ to $\sim 170,000$ below 1 kHz in CCTO samples were observable with increasing sintering temperatures from 980 to 1000°C but the values were systemically decreased up to $\sim 69,000$ at the same frequency regions with further increasing the sintering temperatures up to 1080°C . The abnormal grain growth was also observable when the holding times were increased from 30 min to 24 h at sintering temperatures higher than 1000°C . The CCTO ceramic sintered at 1060°C with the holding times up to 3 h consisted only small grains ($< \sim 5 \mu\text{m}$) but small amount of abnormally grown large grains appeared in the sample for 6 h. Then, the population density and the average grain size of these grains were significantly increased in sample for 9 h. Finally, the abnormally grown large CCTO grains ($\sim 150 \mu\text{m}$) appeared in sample for 12

h and no apparent variation in microstructure existed with further increase in holding times up to 24 h. While the ϵ_r values of samples sintered for the holding time up to 6 h were almost unaltered ($\sim 3,000$ at 1 kHz), the ϵ_r values were abruptly increased to $\sim 42,000$ for 9 h and further increase up to $\sim 88,000$ for 24 h. On the other hand, according to the Z^* and M^* spectroscopy analyses, the improvement of the ϵ_r values in the CCTO ceramics fabricated at various sintering conditions was surely attributable to the high C_{gb} values. Consequently, the high capacitive grain boundary must be the origin of CDR in CCTO ceramics, supporting the grain boundary IBLC model.

Meanwhile, the ϵ_r values in CCTO single crystals were strongly dependent on the electrodes, indicating that relatively higher ϵ_r values of $\sim 200,000$ at 1 kHz were observable in the CCTO single crystals with Ag electrode due to the high contact R value of ~ 80 k Ω . However, the ϵ_r values in CCTO single crystals with Au and InGa electrodes were remarkably lower than that of sample with Ag electrode at the same frequency and ohmic conduction was observable in the I - V characteristics. These results implied that high contact R value is indispensable for inducing CDR in CCTO single crystals.

In conclusion, the CDR in CCTO ceramics and single crystals originate from the grain boundary effect with high C_{gb} values and the nonohmic contact effect at the interface between sample and electrode, respectively.

References

- [1] M. A. Subramanian *et al.*, *J. Solid. State. Chem.*, 151, 323 (2000)
- [2] D. C. Sinclair *et al.*, *Appl. Phys. Lett.*, 80, 2153 (2002)
- [3] T. B. Adams *et al.*, *Adv. Mater.*, 14, 1321 (2002)
- [4] T. B. Adams *et al.*, *J. Am. Ceram. Soc.*, 89, 3129 (2006)
- [5] D. K. Yoo *et al.*, *Solid. State. Phenom.*, 124, 143 (2007)
- [6] D. C. Sinclair *et al.*, *Appl. Phys. Lett.*, 80, 2153 (2002)
- [7] S. Y. Chung *et al.*, *Nat. Mater.*, 3, 774 (2004)
- [8] Y. H. Lin *et al.*, *J. Appl. Phys.*, 103, 074111 (2008)
- [9] T. T. Fang *et al.*, *Chem. Mater.*, 17, 5167 (2005)
- [10] M. A. Ramirez *et al.*, *J. Phys. D Appl. Phys.*, 42, 185503 (2009)
- [11] S. Krohns *et al.*, *Appl. Phys. Lett.*, 91, 022910 (2007)
- [12] M. C. Ferrarelli *et al.*, *J. Mater. Chem.*, 19, 5916 (2009)
- [13] J. Li *et al.*, *Solid State Commun.*, 135, 260 (2005)
- [14] M. H. Whangbo *et al.*, *Chem. Mater.*, 18, 3257 (2009)
- [15] W. Yuan *et al.*, *J. Phys. D: Appl. Phys.*, 42, 175401 (2009)
- [16] L. Ni *et al.*, *Solid. State. Commun.*, 139, 45 (2006).
- [17] K. M. Kim *et al.*, *J. Eur. Ceram. Soc.*, 27, 3991 (2007).
- [18] S. F. Shao *et al.*, *J. Appl. Phys.*, 99, 084106 (2006).
- [19] G. Cao *et al.*, *J. Phys. D: Appl. Phys.*, 40, 2899 (2007).
- [20] T. T. Fang *et al.*, *J. Am. Ceram. Soc.*, 87, 2072 (2004).
- [21] E. J. Abram *et al.*, *J. Electroceram.* 10, 165 (2003).
- [22] T. B. Adams *et al.*, *Phys. Rev. B.* 73, 094124 (2006).
- [23] W. Li *et al.*, *Phys. Rev. B.*, 75, 012104 (2007).

- [24] W. Li *et al.*, *Appl. Phys. Lett.*, 89, 242906 (2006).
- [25] S. F. Shao *et al.*, *Solid. State. Commun.*, 142, 281 (2007).
- [26] P. R. Bueno *et al.*, *Appl. Phys. Lett.*, 89, 191117 (2006).
- [27] P. R. Bueno *et al.*, *Appl. Phys. Lett.*, 90, 142912 (2007).
- [28] J. L. Zhang *et al.*, *Appl. Phys. Lett.*, **87**, 142901 (2005).
- [29] B. S. Prakash *et al.*, *J. Phys. Chem. Solids.*, **68**, 490 (2007).
- [30] S. D. Yang *et al.*, *M.A. Thesis.*, (2003)

Table 3.1 The obtained ρ_g , C_g , ρ_{gb} , C_{gb} values of CCTO ceramics sintered at various temperatures ranging from 980 to 1080°C for 12 h using Z^* and M^* spectroscopy.

Sintering Temp (°C)	ρ_g (Ωcm)	C_g (pF/cm)	ρ_{gb} ($M\Omega\text{cm}$)	C_{gb} (pF/cm)
980	365	177	169	13,296
1000	93.3	369	42	944,562
1020	54.3	490	71	1,131,869
1040	54.2	384	92	473,591
1060	36.0	168	50	323,935
1080	42.8	333	36	366,850

Table 3.2 The obtained ρ_g , C_g , ρ_{gb} , C_{gb} values of CCTO ceramics sintered at 1060°C with various holding times from 30 min to 24 h using Z^* and M^* spectroscopy

Holding Time (h)	ρ_g (Ωcm)	C_g (pF/cm)	ρ_{gb} ($M\Omega\text{cm}$)	C_{gb} (pF/cm)
3	342	340	162	15,143
6	263	321	185	14,532
9	54	214	41	207,117
12	36	168	50	323,935

Table 3.3 The obtained $\rho_{\text{contact+gb}}$ and $C_{\text{contact+gb}}$ values of polycrystalline CCTO ceramics sintered at 1060°C for 12 h in air

	Ag-screen	Au-Evap	Ag-sputter	InGa
$\rho_{\text{contact+gb}}$ ($M\Omega\text{cm}$)	51.26	45.39	39.18	28.27
$C_{\text{contact+gb}}$ (nF/cm)	216.78	222.35	191.07	235.06

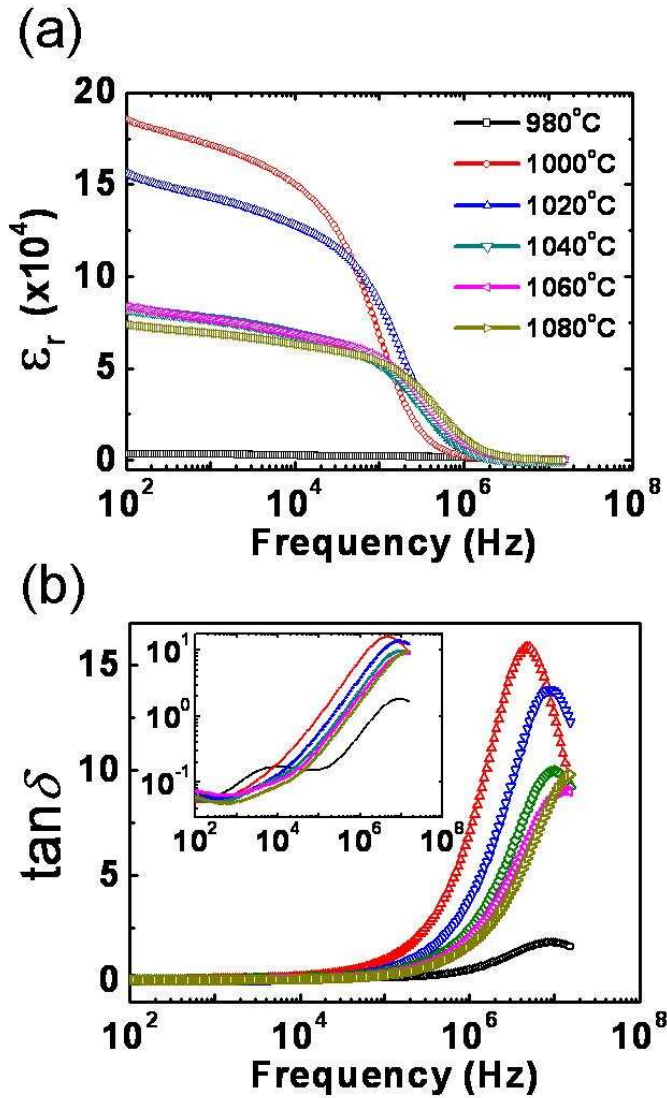


Fig. 3.1 The ϵ_r (a) and $\tan \delta$ (b) properties of CCTO ceramics fabricated at various sintering temperatures ranging from 980 to 1060°C for 12 h as a function of frequency from 100 Hz to 15 MHz. The inset of Fig. 1(b) shows the log-log plot of $\tan \delta$ properties of the CCTO samples

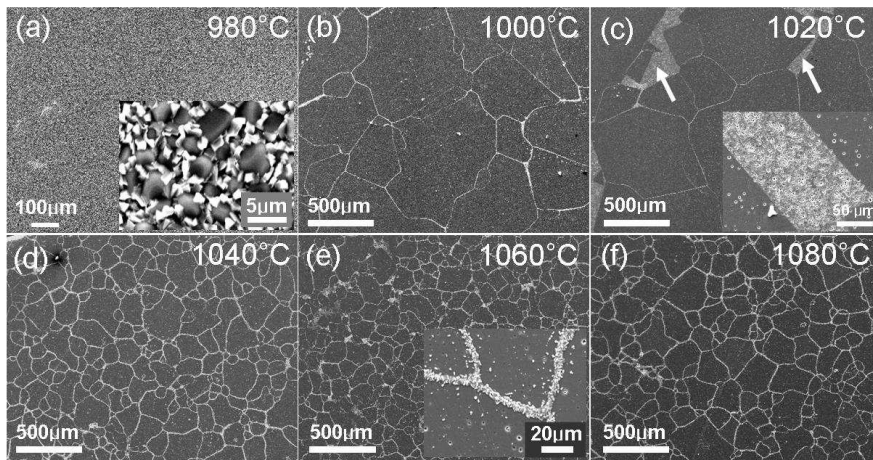


Fig. 3.2 SEM images of CCTO ceramics sintered at various sintering temperatures of 980°C (a), 1000°C (b), 1020°C (c), 1040°C (d), 1060°C (e) and 1080°C (f), respectively, after thermal etching process at 900°C for 1 h in air. The insets of Fig. 3.2(a) and (e) show the enlarged image of Fig. 3.2(a) and grain boundary region of Fig. 3.2(e), respectively. The inset of Fig. 3.2(c) shows the enlarged image of the small-grained regions indicated by arrows in Fig. 3.2(c)

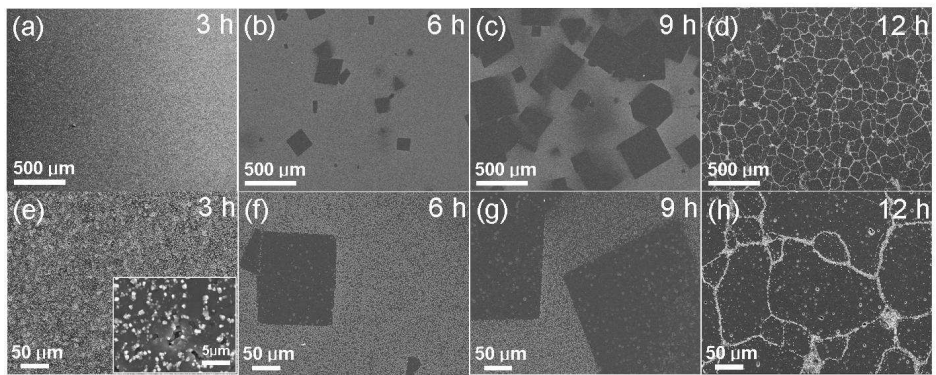


Fig. 3.3 Selected SEM images of CCTO ceramics sintered at 1060°C with various holding times of 3 h (a) and (e), 6 h (b) and (f), 9 h (c) and (g), and 12 h (d) and (h), respectively. The inset of Fig. 3.3(e) shows the enlarged image of Fig. 3.3(e)

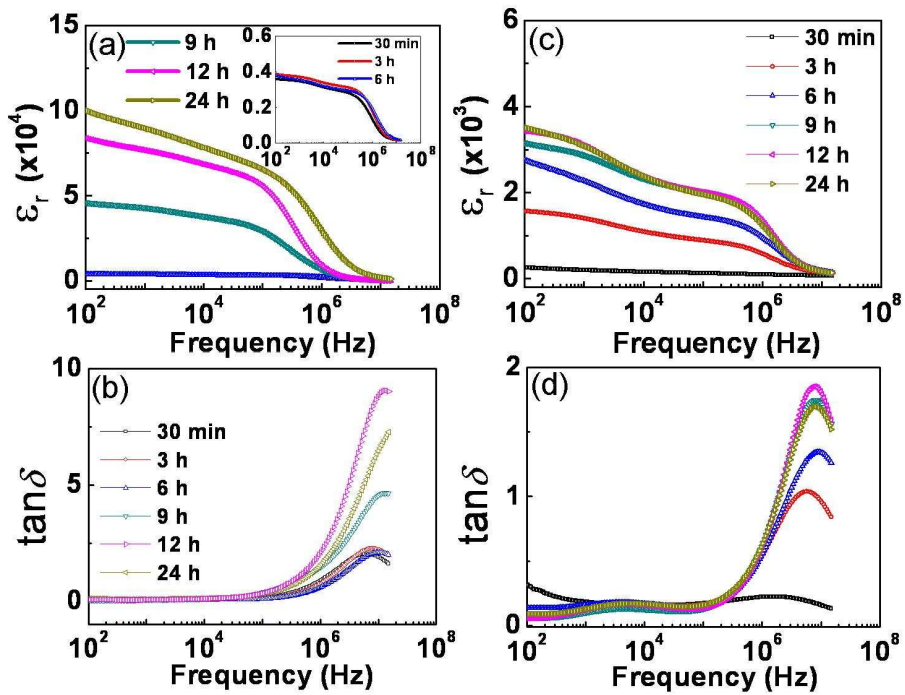


Fig. 3.4 Frequency dependent ϵ_r and $\tan\delta$ properties of CCTO ceramics from 100 Hz to 15 MHz sintered at 1060°C (a) and (b) and 980°C (c) and (d), respectively, with the various holding times from 30 min to 24 h. The inset of Fig. 3.4(a) shows the frequency dependent ϵ_r properties of samples with the holding times of 30min, 3 h, and 6 h. All data are replotted from our previous report of ref. [5]

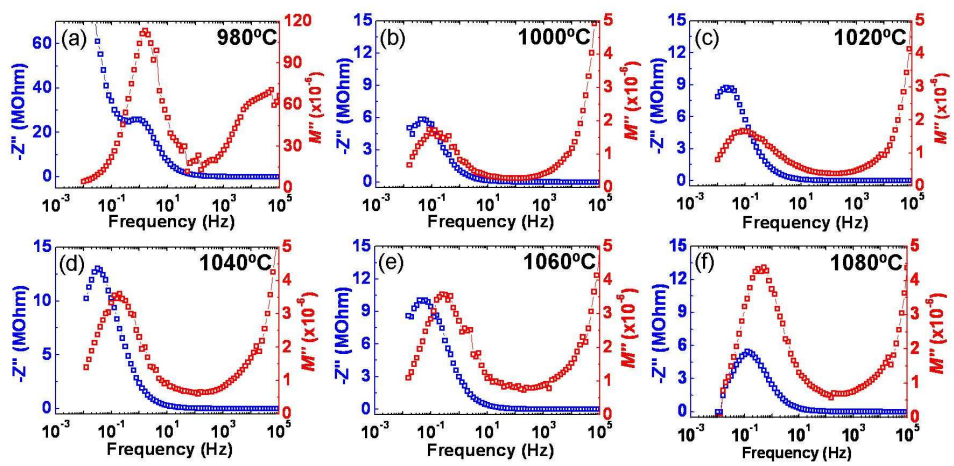


Fig. 3.5 The frequency dependent imaginary part of Z^* and M^* spectroscopy of CCTO ceramics sintered at 980°C (a), 1000°C (b), 1020°C (c), 1040°C (d), 1060°C (e) and 1080°C (f), respectively, for 12 h in air.

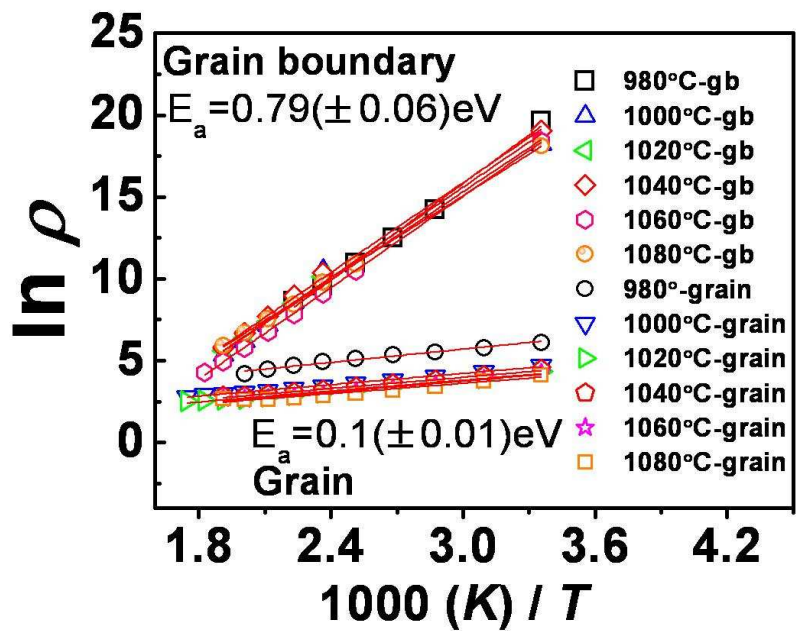


Fig. 3.6 The Arrhenius plots of ρ_g and ρ_{gb} values of CCTO ceramics sintered at various temperatures ranging from 980 to 1080°C for 12 h

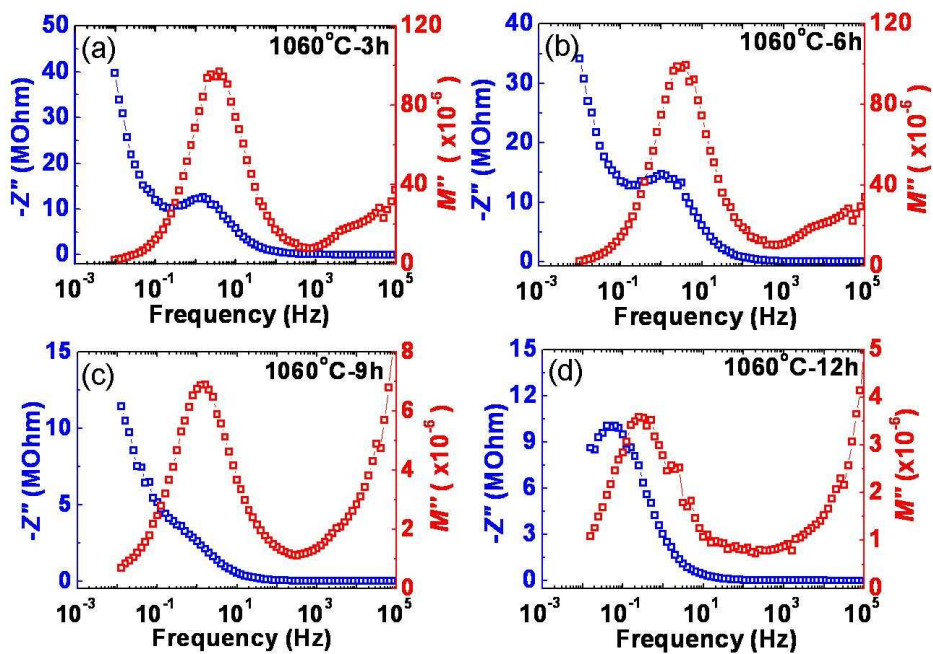


Fig. 3.7 The frequency dependent imaginary part of Z^* and M^* spectroscopy of CCTO ceramics sintered at 1060°C with the various holding times of 3 h (a), 6 h (b), 9 h (c), and 12 h (d), respectively

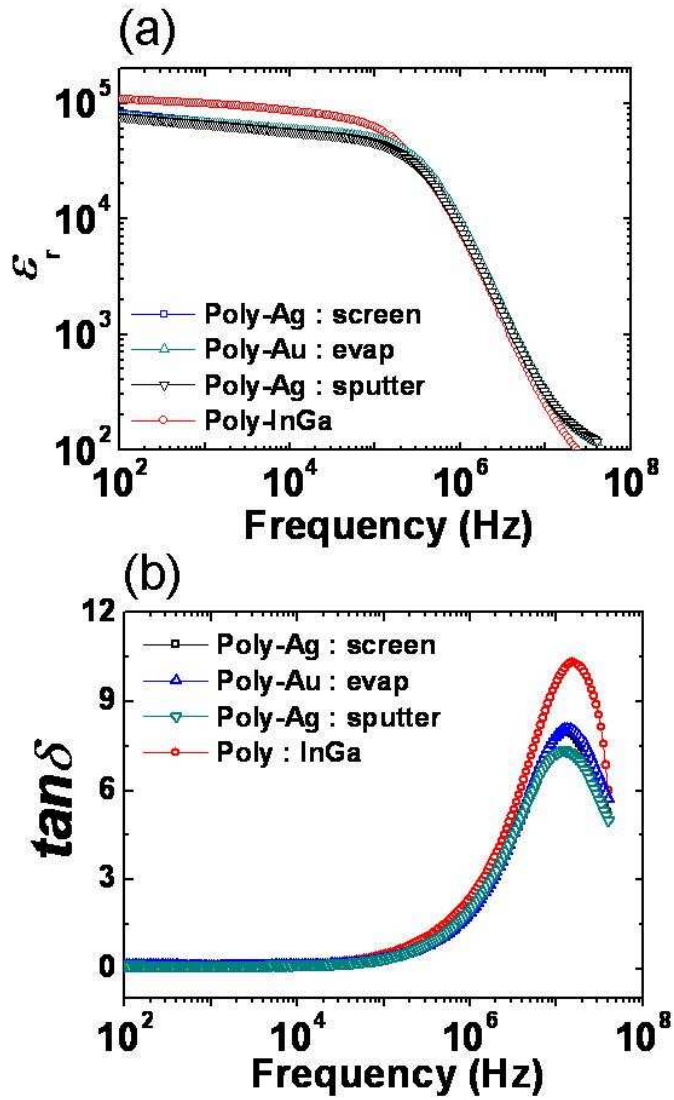


Fig. 3.8 The frequency-dependent ϵ_r and $\tan\delta$ values of polycrystalline CCTO ceramics with various electrodes

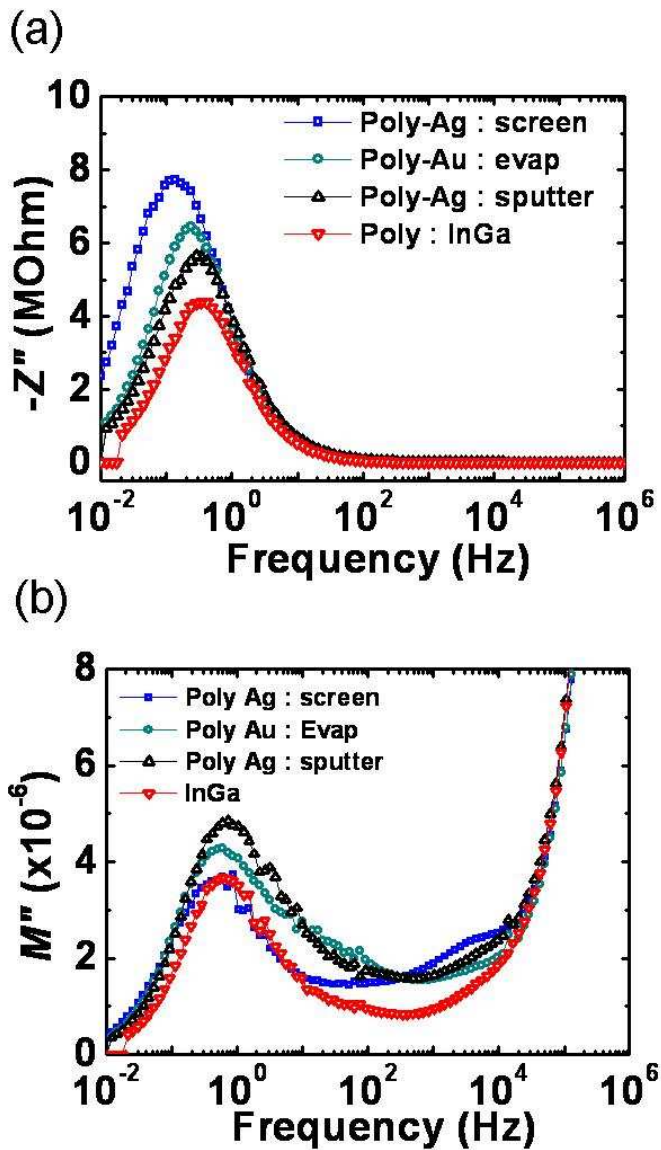


Fig. 3.9 The frequency dependent imaginary part of Z^* and M^* spectroscopy of CCTO ceramics sintered at 1060°C with various electrodes

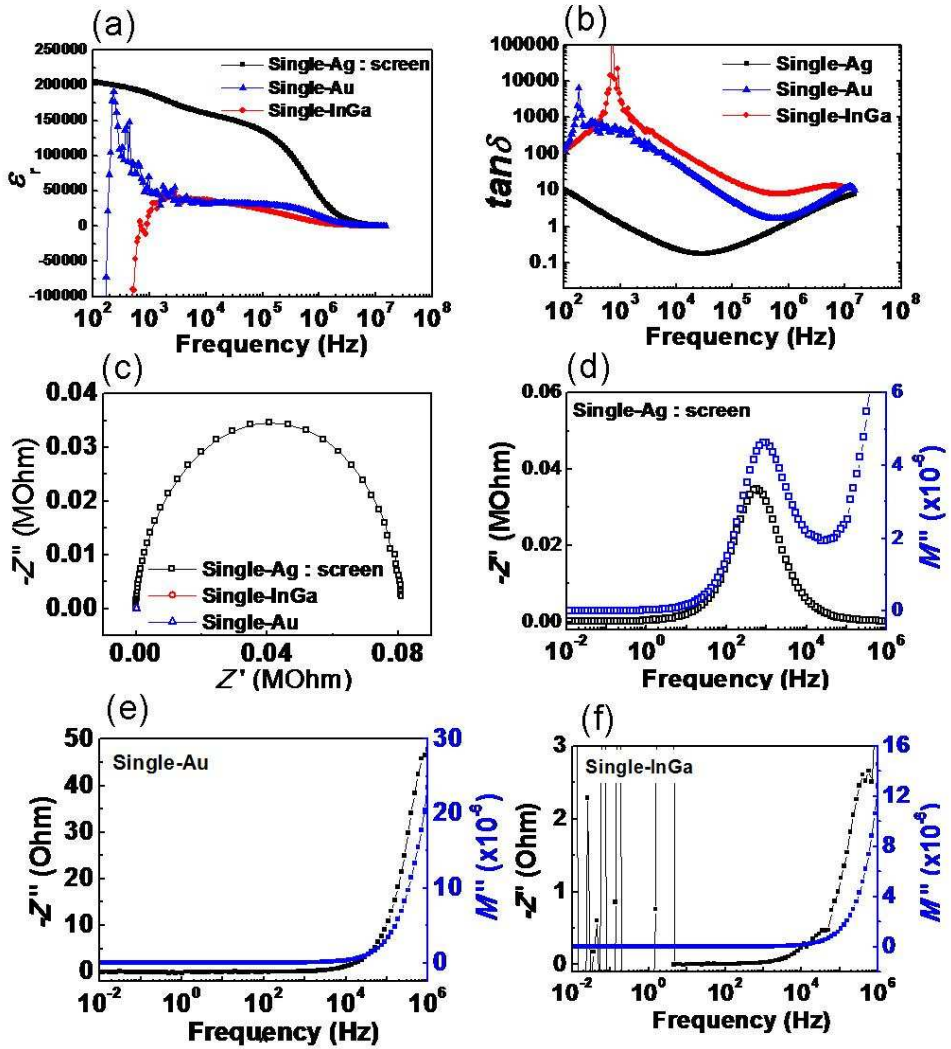


Fig. 3.10 The frequency-dependent ϵ_r and $\tan\delta$ properties (a) and (b), cole-cole plot (c), and frequency-dependent imaginary part of Z^* and M^* spectroscopy of CCTO single crystals

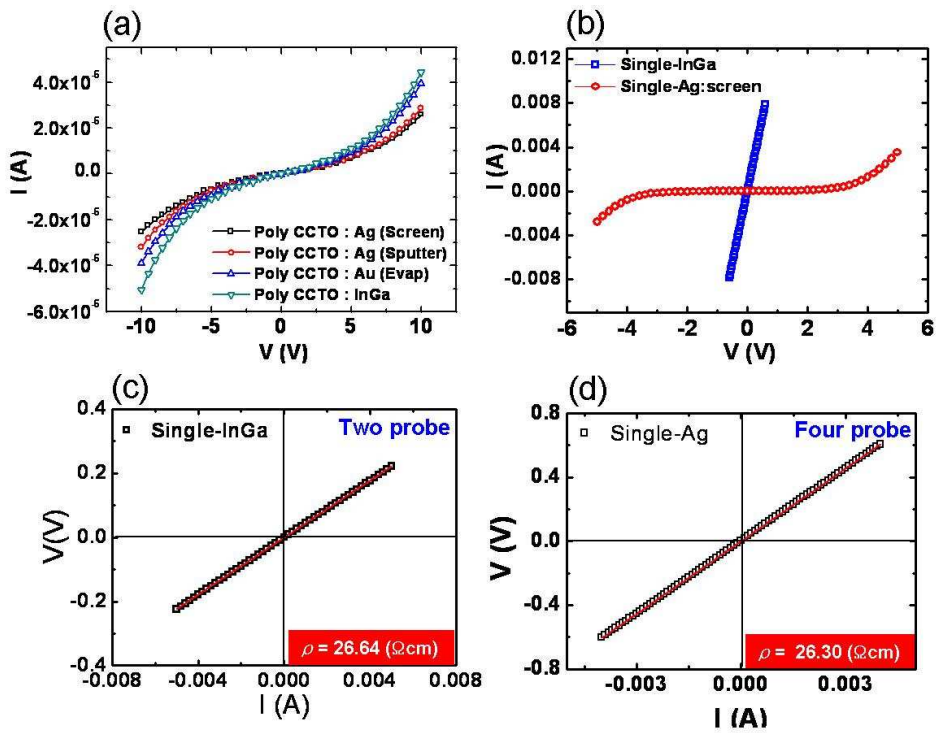


Fig. 3.11 *I-V* characteristics of polycrystalline CCTO (a), single crystal CCTO (b), and *I-V* characteristics of single crystal CCTO with InGa electrode (c), and Ag electrode (d)

Chapter 4. Colossal dielectric responses of

$(\text{Ca}_{1-x}\text{Sr}_x)\text{Cu}_3\text{Ti}_4\text{O}_{12}$ ($0 \leq x \leq 1$) ceramics

4.1. Introduction

CCTO polycrystalline ceramic ($\epsilon_r > 10,000$) has drawn a great attention of researchers due to their temperature-independent colossal dielectric response (CDR) in a wide temperature region of 100~600 K.[1] However, high $\tan\delta$ values (> 0.1 at 1 kHz) and large leakage currents with a low breakdown voltage hindered a real application of CCTO ceramics in the capacitor industry.[2-3] In order to overcome these problems, there have been many efforts including the second phase addition and substitution of cations. For instance, numerous metal oxides such as TeO_2 [2], ZrO_2 [4], TiO_2 [5] and CaTiO_3 [6] have been employed as the second phase, and various elements including Mg [7], Sc [8], Sr [9], Mn [10], and La [11] for the Cu sites and Sc [8], Mn [12], Ta [13], Nb [13-14], and Al [15] for the Ti sites have been tried for a partial substitution of the cation sites in CCTO. In contrast to the above attempts, the substitution for the Ca site has not been widely investigated and limited to only a few elements of La [16] and Sr [17-19]. Feng *et al.* [16] reported that remarkably decreased $\tan\delta$ value of ~ 0.015 at 1 kHz was achievable from La-substituted CCTO ceramics having the composition of $\text{Ca}_{0.8}\text{La}_{0.2}\text{Cu}_3\text{Ti}_4\text{O}_{12}$, which was however accompanied by a significant decrease in the ϵ_r value of $\sim 3,000$ at 1 kHz. According to Xue *et al.* [17], the solubility limit of Sr for the Ca site was $x=0.1$ in $\text{Ca}_{1-x}\text{Sr}_x\text{CTiO}$, and both ϵ_r and

$\tan\delta$ values were simultaneously increased from ~16,000 to ~35,000 and from 0.04 to 0.08, respectively, up to $x=0.1$ due to increased C values and electrical conductance ($1/R$) of grain boundary. On the contrary to this report, Schmidt *et al.* [18] reported that the solubility limit of Sr was $x=0.2$ in $C_{1-x}S_x$ CTO and the Sr substitution affected their grain boundary ε_r values. In addition, Li *et al.* [19] synthesized the $C_{1-x}S_x$ CTO ($x=1$) ceramic and insisted that the ε_r values (~200) of the compound were much lower than those of conventional CCTO ceramic at room temperature.

Within the best of our knowledge, the dielectric and electrical properties of $C_{1-x}S_x$ CTO ceramics have never been investigated for the full composition range of $0\leq x\leq 1$ yet. Moreover, in previous reports, [17-19] the relationship between the microstructure and dielectric properties was not carefully studied. Therefore, in this study, we have systematically investigated the relationship between microstructures and dielectric properties for $C_{1-x}S_x$ CTO ($0\leq x\leq 1$) ceramics. In addition, the electrical properties of grain and grain boundary were quantitatively analyzed using Z^* and M^* spectroscopy for clarifying the origin for CDR in $C_{1-x}S_x$ CTO ($0\leq x\leq 1$) ceramics.

4.2. Experimental

The $C_{1-x}S_x$ CTO ($0\leq x\leq 1$) ceramics with the Sr substituent $x=0, 0.2, 0.4, 0.6, 0.8,$ and 1.0 were fabricated by solid state reaction process with the high purity powders of CaCO_3 , SrCO_3 (Cerac, 99.95%), CuO (High Purity Chemicals, 99.99%) and TiO_2 (High Purity Chemicals, 99.99%). The mixed-powder was weighted and ball-milled in ethyl alcohol using a polyethylene

bottle with ZrO₂ balls for 24 h. The ball-milled powder was uniaxially pressed into pellets and calcined at 950°C for 24 h in air. Then, as-calcined pellets were ball-milled for 24 h and consolidated by cold isostatic pressing with the pressure of 100 MPa. The samples were sintered at various high temperatures of 1060°C ($x=0$ and $x=0.2$), 1040°C ($x=0.4$ and $x=0.6$), 1020°C ($x=0.8$) and 1000°C ($x=1$) in air for 24 h. The sintering temperatures were determined by the differential thermal analysis for obtaining relatively high sintered density. All samples showed the relative sintered density over ~98% by Archimedes' method. The phase analysis and lattice parameter determination were performed by high-resolution X-ray diffraction pattern (XRD, BRUKER, D8 advance) with TREOR (Trial and Error program for indexing of unknown powder patterns) program, respectively [20]. The microstructure was observed by scanning electron microscopy (SEM, JSM-5600) and the second phase segregated at grain boundary in C_{1-x}S_xCTO ($0 \leq x \leq 1$) samples was identified by energy dispersive spectroscopy attached to SEM. The average grain size was analyzed by an image analyzer. For the electrical measurement, Ag paste was screen printed and fired at 600°C for 1h in air. The frequency dependent ϵ_r and $\tan\delta$ values were measured by an impedance/gain-phase analyzer (HP 4194a) in the frequency range of 10² to 40 MHz with an oscillation voltage of 500 mV. The Z^* and M^* spectroscopy analyses for identifying the ρ and C values of grain and grain boundary were performed using Solatron 1260 and Agilent E4991a at low frequency region (10⁻² ~ 10⁵ Hz) and high frequency (10⁷ ~ 10⁹ Hz) region, respectively.

4.3 Results and discussions

Fig. 4.1 (a) and (b) show the XRD patterns and lattice parameters of $C_{1-x}S_x$ CTO ($0 \leq x \leq 1$), respectively. As shown in the inset of Fig. 4.1(b), the main peak of CCTO at $2\theta \sim 34^\circ$ is shifted to lower diffraction angle with increasing the Sr substituent x for the Ca site, indicating that relatively large size of Sr^{2+} ($a=1.44\text{\AA}$) ions can successfully substitute the Ca^{2+} ($a=1.35\text{\AA}$) sites for the full range of substitution. A linear increase in the lattice parameters with increasing x is in good agreement with the well-known Vegard rule. However, the second phases of $SrTiO_3$ (STO) and CuO are observed for the composition of $x \geq 0.8$ in Fig. 4.1(a), of which results imply that the solubility limit of Sr substituent x exists between 0.6 and 0.8 in $C_{1-x}S_x$ CTO-type solid solutions. Our observations are inconsistent with previous studies by Xue *et al.*[17] and Schmidt *et al.* [18] since they reported the solubility limit of Sr in $C_{1-x}S_x$ CTO ceramics was $x=0.1$ and $x=0.2$, respectively. The $C_{1-x}S_x$ CTO-type solid solutions do not exist for the composition of $x \geq 0.8$ due to the presence of the second phases but our independent study on SCTO reveals that although a single phase SCTO compound without the second phases of STO and CuO could not be prepared as reported by Li *et al.* [19], $Sr_{0.9639(1-y)}Cu_{3.0361(1-y)}Ti_{4+2y}O_{12}$ -type solid solutions exist for the composition of $x \geq 0.8$ at 950°C in air, which will be reported elsewhere.

A wide variety of average grain size in the $C_{1-x}S_x$ CTO ($0 \leq x \leq 1$) is shown in Fig. 4.2. All samples show the abnormal grain growth. Compared to the relatively larger average grain size of ~ 160 , ~ 150 and $\sim 250\ \mu\text{m}$ in samples of $x=0$, 0.2 , and 1 in Fig. 4.2(a), (b), and (f), respectively, the samples of $x=0.4$

and 0.6 show the smaller average grain size of $\sim 80 \mu\text{m}$ in Fig. 4.2 (c) and (d), respectively. Since a large amount of copper-oxide is segregated at grain boundaries in all samples after thermal etching at 900°C for 1 h in air as shown in the inset of Fig. 4.2 (a), the abnormal grain growth is surely related to the copper-oxide liquid phase during sintering. [21-25] Moreover, compared to the samples of $x=0$, 0.2, and 1.0, large amount of copper-oxide lumps indicated by white arrows is observable in the samples of $x=0.4$, 0.6, and 0.8. On the basis of these observations, one can simply speculate that the average grain size of samples is strongly dependent on the amount of Sr substituent x in $\text{C}_{1-x}\text{S}_x\text{CTO}$ ($0 \leq x \leq 1$) ceramics. However, according to the previous study, the microstructure of CCTO ceramics showed a strong dependence on the sintering temperatures and holding times. [22] Similarly, various sintering temperatures ranging from 1000 to 1060°C in the present study play the key role for determining the average grain size of $\text{C}_{1-x}\text{S}_x\text{CTO}$ ($0 \leq x \leq 1$) ceramics so that wide variety of average grain size may be achievable in each composition of $\text{C}_{1-x}\text{S}_x\text{CTO}$ ($0 \leq x \leq 1$) ceramics by adopting numerous sintering temperatures.

The frequency-dependent ϵ_r values in Fig. 4.3(a) indicate that the ϵ_r values in $\text{C}_{1-x}\text{S}_x\text{CTO}$ ($0 \leq x \leq 1$) ceramics are strongly dependent on the microstructures. As the average grain size is decreased from ~ 160 to $\sim 80 \mu\text{m}$ in the samples of $x=0$ and $x=0.4$, respectively, the ϵ_r values at 1 kHz are decreased also from $\epsilon_r \sim 120,000$ to $\sim 50,000$, and then the ϵ_r values are increased up to $\sim 180,000$ at the same frequency with increasing average grain size ($\sim 250 \mu\text{m}$) in $x=1$. The ϵ_r values are proportional to the average grain size and our results are in good agreement with previous studies by

many research groups.[21-22, 26-29] For instance, Sinclair *et al.* [26] have fabricated CCTO ceramics at 1100°C with the various holding times from 3 to 24 h and observed that the ϵ_r values were increased from ~9,000 to ~280,000 at 10 kHz with increasing the average grain size from ~5 to ~300 μm . In addition, Shao *et al.* [29] have observed that the ϵ_r values in CCTO ceramics fabricated at various sintering temperatures ranging from 1000 to 1130°C for 10 h were systemically increased from ~1,200 to ~70,000 with increasing the average grain size from several μm to ~100 μm . Figure 4.3(c) represents that the variation of ϵ_r values from ref. 22, 29, and 30 depends on the microstructure, implying that the ϵ_r values show the strong dependence on the average grain size. Contrary to our results, Li *et al.* [19] insisted that the ϵ_r value in SCTO ceramic was ~200 at 300 K, of which value was remarkably lower than that of our ~180,000 at 1 kHz in SCTO ceramic. The reason for the large discrepancy in the ϵ_r values is ambiguous since the sintering temperatures and holding times in their study are quite similar to our sintering conditions. However, the calcination temperature and holding time of 900°C and 10 h, respectively, are somewhat lower and shorter than those of our 950°C and 24 h, respectively, so that abnormal grain growth may not be developed in their samples due to an incomplete decomposition of SrCO_3 , and thus led to remarkably lower ϵ_r values. As shown in Fig. 4.3(b), the maximum $\tan\delta$ values near $\sim 10^7$ Hz are decreased from ~12 to ~6 with increasing the Sr substituent from $x=0$ to $x=0.6$ and then the values are increased to ~14 with further increasing x up to 1. Moreover, the peaks of $\tan\delta$ values in the $\text{C}_{1-x}\text{S}_x\text{CTO}$ ($0 \leq x \leq 1$) ceramics are shifted to lower frequency region as the Sr substituent x is increased from $x=0$ to $x=1$.

According to the frequency dependent ε_r values in Fig. 4.3(a), the dielectric relaxation in $C_{1-x}S_x$ CTO ($0 \leq x \leq 1$) ceramics starts to occur at relatively lower frequency region with increasing Sr substituent x , resulting the $\tan\delta$ peaks shift to the lower frequency region. In addition, the relatively higher maximum $\tan\delta$ values in CCTO and SCTO ceramics compared to those of other samples are attributable to the higher drop in ε_r values from $\sim 120,000$ (at 1 kHz) to ~ 380 (at 10^7 Hz) and from $\sim 200,000$ (at 1 kHz) to ~ 130 (at 10^7 Hz), respectively. Consequently, the wide variety of ε_r values, maximum $\tan\delta$ values, and frequency for $\tan\delta$ peaks in each sample are strongly dependent on the variation of average grain size.

For understanding the electrical properties of grain and grain boundary in $C_{1-x}S_x$ CTO ($0 \leq x \leq 1$) ceramics, we adopted Z^* and M^* spectroscopy for obtaining the quantitative ρ and C values of the two different regions. All the data are calculated using the equivalent circuit of two parallel RC elements of grain and grain boundary connected in series.

Fig. 4.4 and 4.5 show the frequency dependence of the Z'' and M'' values of grain boundary and grain in $C_{1-x}S_x$ CTO ($0 \leq x \leq 1$) ceramics, respectively. Compared with the higher M''_{\max} values of grains (~ 0.004) at $\sim 10^8$ Hz in Fig. 4.5(b), the M''_{\max} values of grain boundary at $\sim 10^{-1}$ Hz in Fig. 4.4 are remarkably small implying that the C_{gb} values in all samples are much higher than those of C_{g} values because the C values are inversely proportion to the M''_{\max} values as shown in the equation (2) of Chapter 3. In contrast to the M''_{\max} values, the Z''_{\max} values of grain boundary in all samples at $\sim 10^{-2}$ Hz in Fig. 4.4 are higher than those of the Z''_{\max} values in Fig. 4.5(a) so that the ρ_{gb} values are higher than those of ρ_{g} values. The

evaluated ρ_g , ρ_{gb} , C_g , and C_{gb} values in $C_{1-x}S_xCTO$ ($0 \leq x \leq 1$) ceramics are summarized in Table 4.1. As shown in Table 4.1, the ρ_g and C_g values are much smaller than those of ρ_{gb} and C_{gb} values, indicating that the ε_r values in $C_{1-x}S_xCTO$ ($0 \leq x \leq 1$) ceramics should be dominantly affected by the electrical properties of grain boundary. The ρ_g values of samples are systemically increased with increasing the Sr substituent x from 0 to 1 in Table. 4.1. At this stage, the reason for the high conductance of each grain is unclear but the increased ρ_g values with Sr substituent x are surely responsible for the effects of Sr substitution. Meanwhile, except the peaks of M'' values at $\sim 10^{-1}$ Hz in all samples, the two additional peaks of M'' values at ~ 10 Hz are clearly observable in the samples of $x=0.8$ and 1 indicated by arrows in Fig. 4.4(e) and (f), respectively, but the corresponding Z'' peaks at the same frequency are invisible. The obtained C values from these two additional peaks of M'' values using the equation (2) are 390,860 and 1,411,783 pF/cm and the corresponding ρ values from the equation (3) are 915 and 150 k Ω cm, respectively. These two C values are similar to those of C_{gb} values in the samples of $x=0.8$ and 1.0 in Table 4.1, but the ρ values are remarkably smaller than those of ρ_{gb} values in $x=0.8$ and 1.0. The presence of these additional C and ρ values could be due to the presence of STO as shown in Fig. 4.1(a) so that further investigations for the chemical composition of grain boundary using high resolution transmission electron microscopy are required.

Figure 4.6 shows the overall relationship among the ε_r values, average grain size, C_g , and C_{gb} values in $C_{1-x}S_xCTO$ ($0 \leq x \leq 1$) ceramics. As shown in Fig. 4.6, it is obvious that the ε_r values at 1 kHz in all samples are proportional to

the average grain size and C_{gb} values. Consequently, we could summarize our results as the following. First, the linear increase of the lattice parameters from $x=0$ ($a=7.392 \text{ \AA}$) to $x=1$ ($a=7.426 \text{ \AA}$) and XRD peak shift is surely originated from the effects of Sr substituent x for the Ca sites. However, the solubility limit of Sr substituent x exist between 0.6 and 0.8 in the $C_{1-x}S_x$ CTO-type solid solutions and different type of $Sr_{0.9639(1-y)}Cu_{3.0361(1-y)}Ti_{4+2y}O_{12}$ solid solutions exist for the composition of $x \geq 0.8$ at 950°C in air. Second, the increased ρ_g values with increasing x are also attributable to the Sr substitution effects. Third, the remarkable variation of the average grain size in $C_{1-x}S_x$ CTO ($0 \leq x \leq 1$) ceramics is responsible for the sintering temperatures rather than Sr substitution effects. Finally, the ε_r values in all samples show strong dependence on the microstructures so that larger-grained samples show relatively higher ε_r values at 1 kHz compared to those of smaller-grained samples since the larger-grained samples exhibit higher C_{gb} values than those of smaller-grained samples. Further investigations for identifying the reason of high conductance in each grain of $C_{1-x}S_x$ CTO ($0 \leq x \leq 1$) ceramics using admittance spectroscopy are under progress.

4.4 Summary

We have fabricated $C_{1-x}S_x$ CTO ($0 \leq x \leq 1$) ceramics using the solid state reaction at various sintering temperatures ranging from 1000 to 1060 We fabricated $C_{1-x}S_x$ CTO ($0 \leq x \leq 1$) ceramics using the solid state reaction at various sintering temperatures ranging from 1000 to 1060°C for 12 h in air. The linear increase in the lattice parameters with increasing Sr substitution

was observable. The second phases of STO and CuO were, however, unavoidable for the composition $x \geq 0.8$. All samples were composed of abnormally grown large grains. The ϵ_r values at 1 kHz in $C_{1-x}S_xCTO$ ($0 \leq x \leq 1$) ceramics were strongly dependent on the average grain size. The relatively higher ϵ_r values of $\sim 120,000$ and $\sim 180,000$ at 1 kHz were obtainable from the samples of $x=0$ and 1, respectively, due to the larger average grain size of ~ 160 and $\sim 250 \mu\text{m}$, respectively, with higher C_{gb} values compared with those of other samples. However, the ϵ_r values at 1 kHz were decreased with increasing x so that the lowest ϵ_r values of $\sim 40,000$ at 1 kHz in the samples of $x=0.4$ and 0.6 were observable with average grain sizes of $\sim 80 \mu\text{m}$. The maximum $\tan\delta$ values in all samples were shifted to lower frequency region with increasing Sr substituent x . Relatively higher $\tan\delta$ values in the samples of $x=0$ and 1 at $\sim 10^7$ Hz were observed compared to those of other samples. The frequency dependent Z^* and M^* spectroscopy indicated that the ρ_{gb} and C_{gb} values were significantly higher than those of ρ_g and C_g values in each sample so that the electrical properties of grain boundary were responsible for the colossal dielectric responses of $C_{1-x}S_xCTO$ ($0 \leq x \leq 1$) ceramics.

References

- [1] M. A. Subramanian *et al.*, *J. Solid State Chem.* 151, 323 (2000)
- [2] F. Amaral *et al.*, *J. Non-Cryst Solids.* 357, 775 (2011)
- [3] M. Li *et al.*, *J. Appl. Phys.* 104, 074107 (2008)
- [4] E. A. Patterson *et al.*, *Appl. Phys. Lett.* 87, 182911 (2005)
- [5] Y. H. Lin *et al.*, *J. Appl. Phys.* 103, 074111 (2008)
- [6] C. M. Wang *et al.*, *J. Alloy. Compd.* 491, 423 (2010)
- [7] M. Li *et al.*, *J. Appl. Phys.* 104, 074107 (2008)
- [8] S. Y. Chung *et al.*, *Appl. Phys. Lett.* 89, 191907 (2006)
- [9] C. H. Mu *et al.*, *J. Alloy. Compd.* 471, 137 (2009)
- [10] M. Li *et al.*, *Appl. Phys. Lett.* 88, 232903, (2006)
- [11] S. F. Shao *et al.*, *Appl. Phys. Lett.* 91, 042905 (2007)
- [12] J. Cai *et al.*, *Appl. Phys. Lett.* 91, 252905 (2007)
- [13] S. Y. Chung *et al.*, *Appl. Phys. Lett.* 91, 091912 (2007)
- [14] S. H. Hong *et al.*, *J. Am. Ceram. Soc.* 90, 2118 (2007)
- [15] S. W. Choi *et al.*, *J. Am. Ceram. Soc.* 90, 4009 (2007)
- [16] L. Feng *et al.*, *Phys. Stat. Sol. (a)*, 203, R22 (2006)
- [17] H. Xue *et al.*, *J. Alloy. Compd.* 482, L14 (2009)
- [18] R. Schmidt *et al.*, *Chem. Mater.* 22, 6 (2010)
- [19] J. Li *et al.*, *Chem. Mater.* 16, 5223 (2004)
- [20] P. E. Werner *et al.*, *J. Appl. Cryst.* 18, 367 (1985)
- [21] S. Y. Lee *et al.*, *Electron. Mater. Lett.* 3, 23 (2007)
- [22] S. Y. Lee *et al.*, *Electron. Mater. Lett.* 7, 287 (2011)
- [23] T. T. Fang *et al.*, *Acta. Mater.* 54, 2867 (2006)
- [24] T. T. Fang *et al.*, *J. Am. Ceram. Soc.* 87, 2072 (2004)
- [25] K. M. Kim *et al.*, *J. Eur. Ceram. Soc.* 27, 3991 (2007)
- [26] T. B. Adams *et al.*, *Adv. Mater.* 14, 1321 (2002)
- [27] T. B. Adams *et al.*, *J. Am. Ceram. Soc.* 89, 3129 (2006)

- [28] T. B. Adams *et al.*, *Phys. Rev. B.* 73, 094124 (2006)
- [29] S. F. Shao *et al.*, *J. Appl. Phys.* 99, 084106 (2006)
- [30] G. Zhang *et al.*, *J. Phys. D: Appl. Phys.* 38, 1824 (2005)

Table 4.1 The obtained ρ_g , C_g , ρ_{gb} , and C_{gb} values of $C_{1-x}S_xCTO$ ($0 \leq x \leq 1$) ceramics sintered at various sintering temperatures ranging from 1000 to 1060°C from the equivalent circuit with two parallel RC elements using Z^* and M^* spectroscopy

Compositions	ρ_g (Ωcm)	C_g (pF/cm)	ρ_{gb} ($M\Omega\text{cm}$)	C_{gb} (nF/cm)
$x=0$	31	349	13.8	560
$x=0.2$	32	331	76.9	266
$x=0.4$	47	369	115.7	217
$x=0.6$	72	388	147.8	283
$x=0.8$	103	379	18.7	999
$x=1.0$	114	346	49.6	1,315

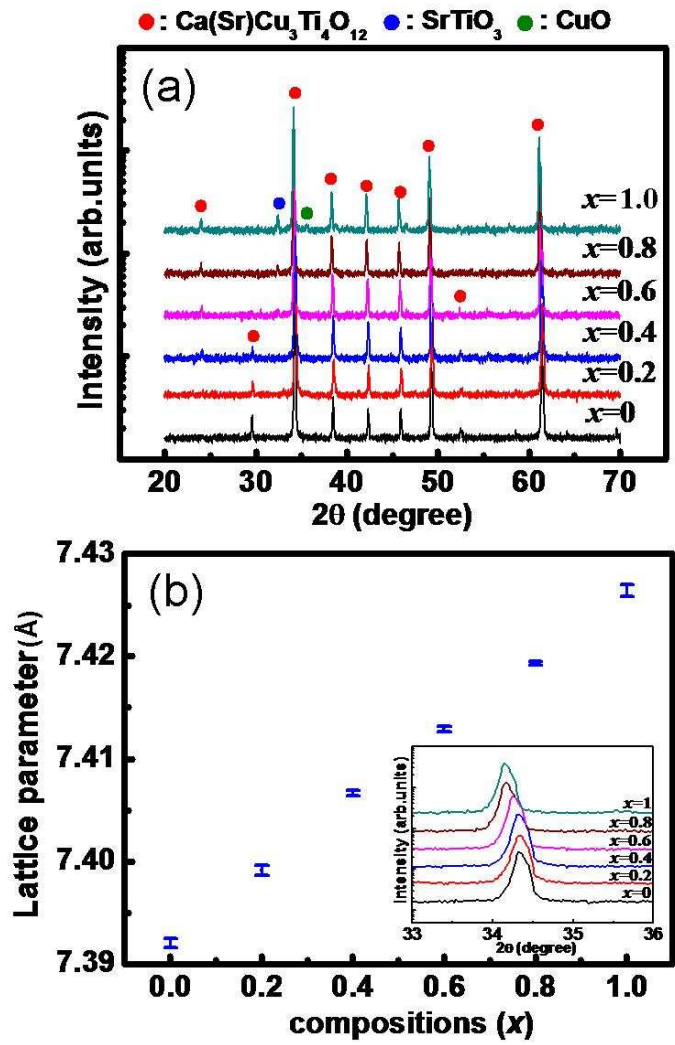


Fig. 4.1 Powder XRD patterns (a) and lattice parameter measurement (b) of $\text{C}_{1-x}\text{S}_x\text{CTO}$ ($0 \leq x \leq 1$) ceramics

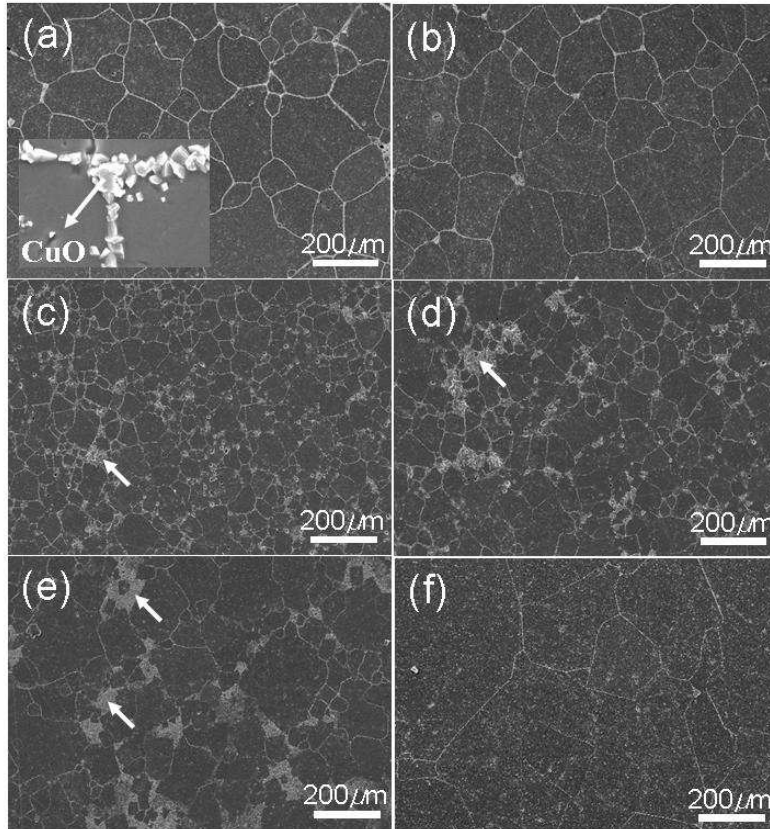


Fig. 4.2 SEM images of CCTO (a), C_{0.8}S_{0.2}CTO (b), C_{0.6}S_{0.4}CTO (c), C_{0.4}S_{0.6}CTO (d), C_{0.2}S_{0.8}CTO (e), and SCTO (f) with thermal etching process at 900°C for 1 h. The inset of Fig. 4.2 (a) shows the segregated copper-oxide at grain boundary

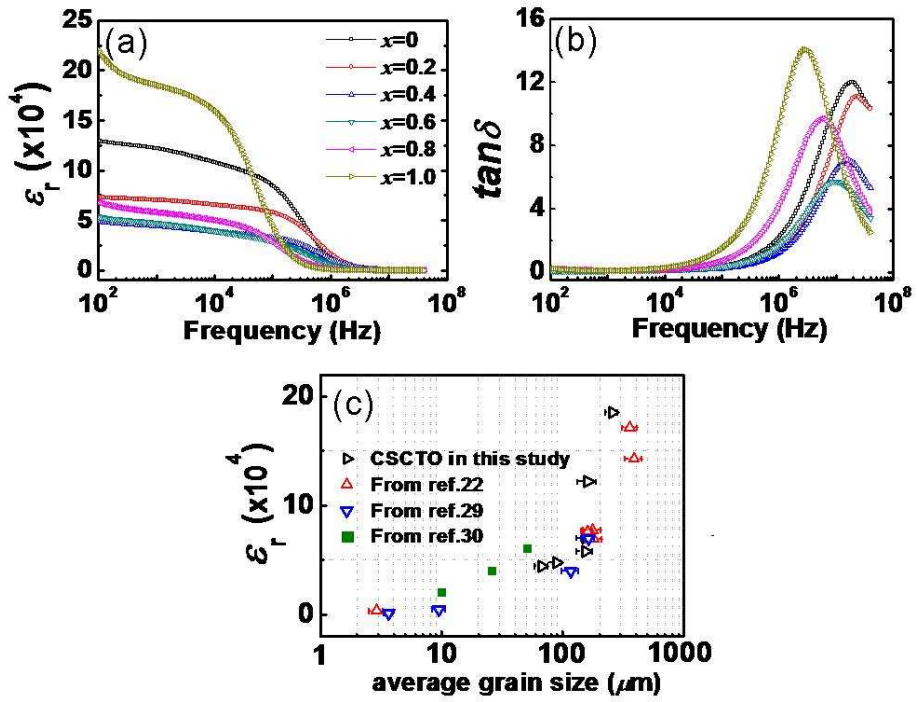


Fig. 4.3 Frequency dependent ϵ_r (a), $\tan\delta$ (b) properties of $C_{1-x}S_xCTO$ ($0 \leq x \leq 1$) ceramics from 100 Hz to 40 MHz, and the variation of the ϵ_r values from ref. 22, 29 and 30 depending on average grain size (c). Note that all the ϵ_r values are measured at 1 kHz. All the representative average grain size was measured by an image analyzer

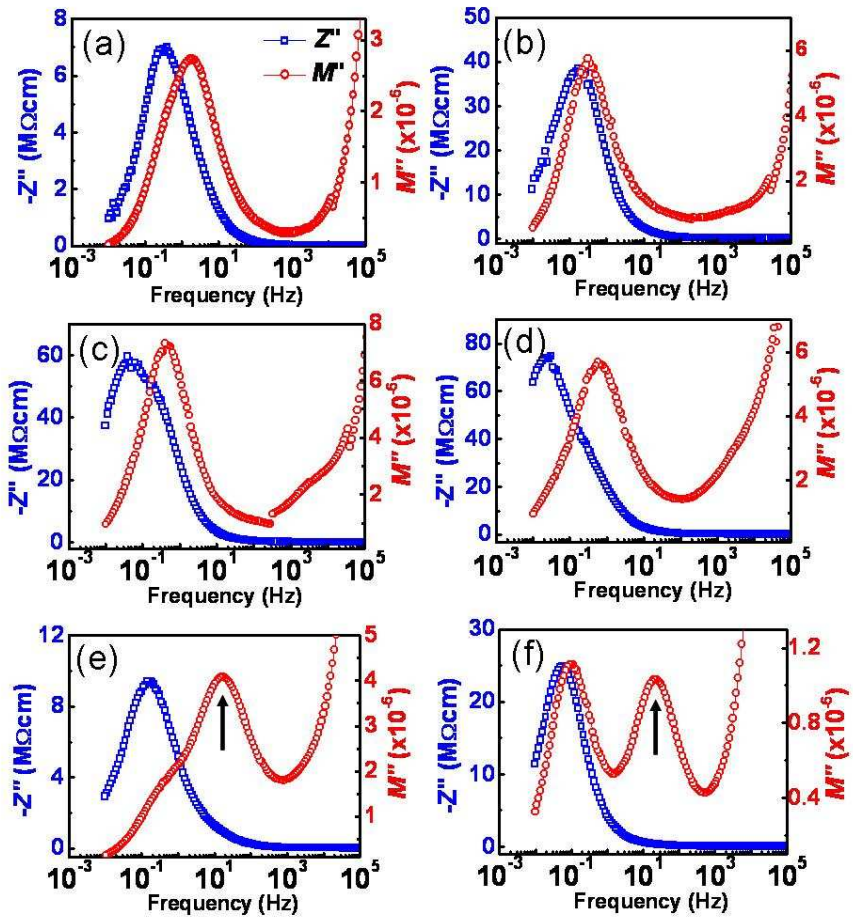


Fig. 4.4 Frequency dependent Z'' and M'' properties of CCTO (a), $C_{0.8}S_{0.2}CTO$ (b), $C_{0.6}S_{0.4}CTO$ (c), $C_{0.4}S_{0.6}CTiO$ (d), $C_{0.2}S_{0.8}CTO$ (e), and SCTO (f) ceramics measured from 10^{-2} to 10^5 Hz

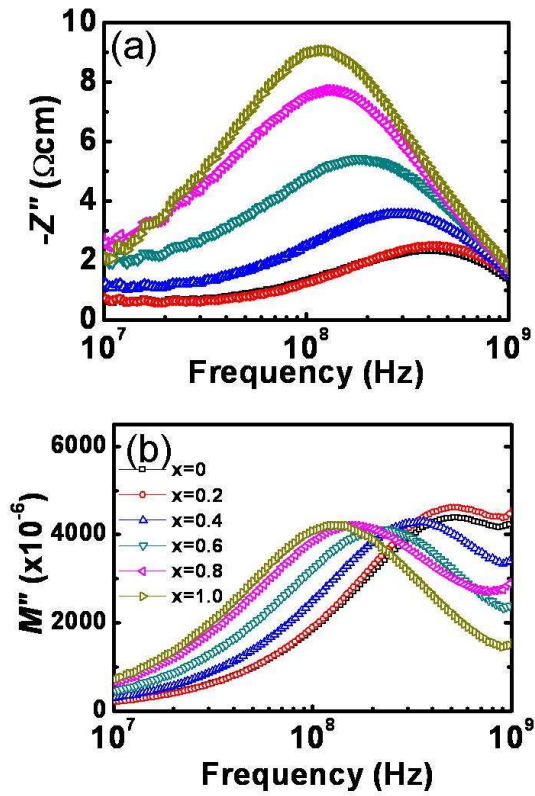


Fig. 4.5 Frequency dependent Z'' (a) and M'' (b) properties of $C_{1-x}S_xCTO$ ($0 \leq x \leq 1$) ceramics measured from 10^7 to 10^9 Hz

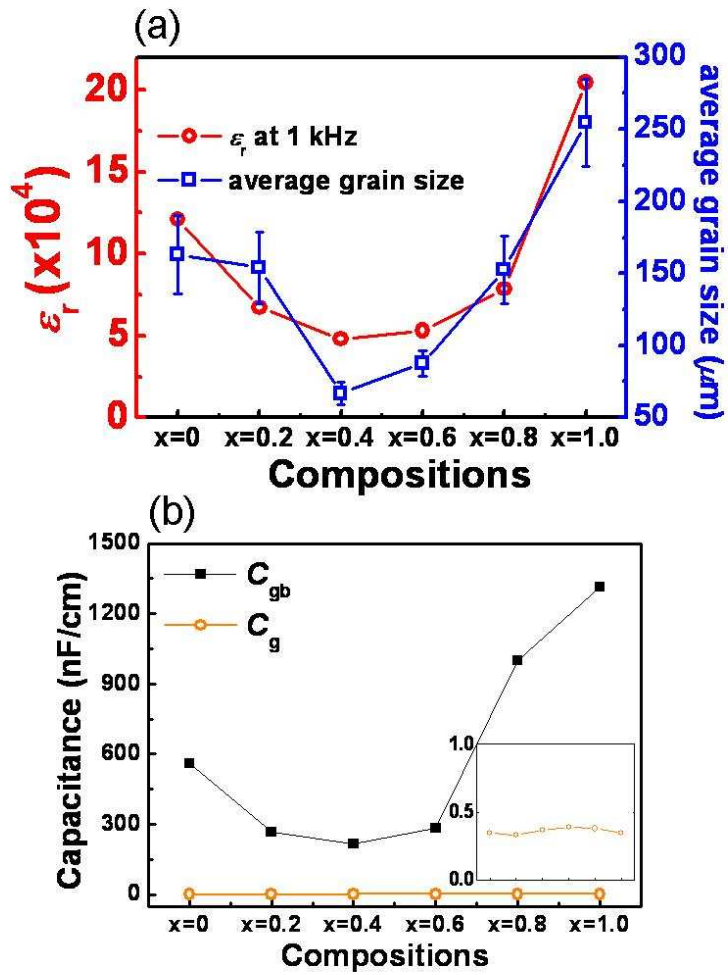


Fig. 4.6 The relationship among ϵ_r values at 1 kHz, average grain size, C_g , and C_{gb} , values of $C_{1-x}S_xCTO$ ($0 \leq x \leq 1$) ceramics

Chapter 5. Subsolidus phase compatibilities in the SrO(CaO)-CuO-TiO₂ ternary system

5.1 Introduction

The CaCu₃Ti₄O₁₂ (CCTO) ceramic has attracted much attention due to the high dielectric constant (ϵ_r) over $\sim 10,000$ with no phase transition over a wide temperature region from 100 to 600 K.[1] Although the high dielectric loss ($\tan\delta > \sim 0.1$) and leakage current in CCTO ceramic are somewhat high for practical application, the extraordinary high ϵ_r values in CCTO ceramic are strong advantage for high- k capacitor. According to Subramanian *et al.*[1] only CCTO compound shows the highest ϵ_r values ($> \sim 10,000$) compared to those of ACu₃Ti₄O₁₂ (ACTO, A= Cd, La, Sm, Dy, Y, Bi, Nd, and Gd) family compounds and numerous solid solutions such as CaCu_{3-x}B_xTi₄O₁₂ (B=Sr [2], Mn [3], and La [4]) and CaCu₃Ti_{4-x}C_xO₁₂ (C=Mn [5], and Al [6]).

However, our previous study in Chap.4 revealed that SrCu₃Ti₄O₁₂ (SCTO) sintered at 1000°C for 12 h showed much higher ϵ_r values ($\sim 170,000$ at 1 kHz) than those of CCTO ceramic ($\sim 100,000$ at 1 kHz) although single phase SCTO compound did not exist due to the presence of SrTiO₃ and CuO. In accordance with our study, Li *et al.* [7] have also observed the existence of STO in the stoichiometric SCTO compound and insisted that the pure phase composition should be Sr_{0.946}(Cu_{2.946}Ti_{0.054})Ti₄O₁₂ in the SrO-CuO-TiO₂ ternary system. They measured the ϵ_r value of Sr_{0.946}(Cu_{2.946}Ti_{0.054})Ti₄O₁₂

ceramic and insisted that the values were only ~ 200 at room temperature. Since the detailed observation of microstructure using high resolution transmission electron microscopy and investigations for the relationship between processing conditions and dielectric properties were absent in their study, it may be inappropriate to conclude the merely low ϵ_r values as an intrinsic properties of SCTO ceramic. Prior to the investigations of the dielectric properties in SCTO ceramic, basic understanding of the phase stability around the single phase SCTO in the SrO-CuO-TiO₂ ternary system is indispensable because wide variety of ϵ_r values in the SCTO and CCTO ceramic is expectable due to the microstructure evolution through liquid phase formation which frequently observable in the previous investigations. [8-10]

Therefore, in the present study, we tried to clarify the composition of single phase SCTO using powder X-ray diffraction (XRD) analysis. In addition, the phase relations around the single phase SCTO were investigated for identifying the existence of solid solutions. Finally, the phase boundaries of SrO-rich (SrO $> \sim 36.8\%$) region in the SrO-CuO-TiO₂ ternary system were determined to complete the subsolidus phase diagram over the full composition region.

Meanwhile, the colossal dielectric response (CDR) observed in CCTO ceramics is responsible for the high C_{gb} values and the values are strongly dependent on the microstructure evolution as previously mentioned in Chapter 2 and 3. The abnormal grain growth in CCTO ceramics is related to the formation of CuO-rich liquid phase at grain boundary during sintering. However, the reason for the presence of CuO-rich liquid phase during

sintering has not been clarified in literatures yet. Therefore, we tried to identify the phase relations around the single phase CCTO and the existence of solid solutions in the CaO-CuO-TiO₂ ternary system at 950°C in air using powder XRD analyses. In addition, we investigated the reason for the presence of CuO-rich liquid phase during sintering in CCTO ceramics.

5.2. Experimental

Numerous samples with the nominal compositions around the stoichiometric SCTO and CCTO compounds in the SrO(CaO)-CuO-TiO₂ ternary systems were prepared using the conventional solid state reaction process. Powders of CaCO₃ (Cerac, 99.9%), SrCO₃ (Cerac, 99.9%), CuO (High Purity Chemicals, 99.9%), and TiO₂ (High Purity Chemicals, 99.9%) were used as starting precursors. The various nominal compositions listed in Table. 6.1 and 6.2 were carefully weighted and ball-milled in ethyl alcohol with ZrO₂ balls for 24h, and then dried, sieved and pressed into pellets. The pellets were calcined at 950°C for 24h in air and the processes were repeated for three times to complete the reactions. The as-calcined samples were reground, ball-milled for 24h, dried and sieved. The phase identification and solubility limit were investigated using high-resolution XRD (BRUKER, D8 advance) and lattice parameter was identified by the XRD patterns with TREOR program in Chapter 4. The samples in the Sr_{0.9639(1-y)}Cu_{3.0361(1-y)}Ti_{4+2y}O₁₂ (0≤y≤0.0235) type solid solutions were sintered at 1000°C for 12h in air and Ag paste was screen printed and fired at 600°C for 1 h prior to the electrical measurement. The frequency dependent ϵ_r and $\tan\delta$ properties

between 100 Hz to 20 MHz were investigated using impedance/gain-phase analyzer (HP4194a). The microstructure was observed by SEM (JSM-5600).

5.3. Results and discussion

5.3.1 SrO-CuO-TiO₂ ternary system

The second phase of STO was always observable in the stoichiometric SCTO compound so that we tried to eliminate the STO and identify the single phase composition by selecting the numerous nominal compositions from sample No. 1 to 9 in Table 5.1. The samples from No. 1 to 9 can be represented by the chemical formula of Sr_{1-x}Cu_{3+x}Ti₄O₁₂ (0 ≤ x ≤ 0.0909) below the Table 5.1. With increasing the amount of x from 0 to 0.0909 in the Sr_{1-x}Cu_{3+x}Ti₄O₁₂ compounds in Fig. 5.1(a), the intensity of STO main peak observed at $2\theta \sim 33^\circ$ is gradually decreased and finally disappears in the Sr_{0.9639}Cu_{3.0361}Ti₄O₁₂ (No.4) compound as shown in Fig. 5.1(b). However, the major peaks of CuO observed at $2\theta \sim 35^\circ$ and 38° , respectively, appear with further increasing x from the compositions of Sr_{0.9581}Cu_{3.0419}Ti₄O₁₂ (sample No.5) in Fig. 5.1(b). According to the previous investigation by Li *et al.* [7], small substitution of Ti in Cu site was observed in the stoichiometric SCTO ceramic and the composition of single phase should be Sr_{0.946}(Cu_{2.946}Ti_{0.054})O₁₂ but the existence of solid solutions around the single phase was unidentified in their study. The absence of solid solutions in their study might be responsible for the following reasons. Li *et al.* [7] adopted relatively lower temperature and shorter holding times of 900°C and 12 h,

respectively, for calcination process compared to those of our 950°C and 24 h so that small amount of residual SrCO₃ phase, which was undetectable by XRD, could be remained in their samples. Moreover, they performed the calcination process only one time and this condition was somewhat insufficient for the full decomposition of SrCO₃. Therefore, we tried to investigate the existence of solid solutions around the single phase Sr_{0.9639}Cu_{3.0361}Ti₄O₁₂ compound by selecting various nominal compositions from sample No.10 to 14 in Table 5.1 and performed calcination process for three times to facilitate the full decomposition of SrCO₃. The samples from No. 10 to 14 can be represented by the chemical formula of Sr_{0.9639(1-y)}Cu_{3.0361(1-3y)}Ti_{4+2y}O₁₂ (-0.0121≤y≤0.0386).

Figure 5.2(a) and (b) show the selected nominal compositions of the Sr_{0.9639(1-y)}Cu_{3.0361(1-3y)}Ti_{4+2y}O₁₂ (-0.0121≤y≤0.0386) compounds in the SrO-CuO-TiO₂ ternary system and powder XRD patterns, respectively. Note that both the two compositions of Sr_{1-x}Cu_{3+x}Ti₄O₁₂ (x=0.0361) and Sr_{0.9639(1-y)}Cu_{3.0361(1-3y)}Ti_{4+2y}O₁₂ (y=0) indicate the single phase composition of sample No. 4. While the second phase of CuO is observed in the sample No.10, single phase Sr_{0.9639(1-y)}Cu_{3.0361(1-3y)}Ti_{4+2y}O₁₂ compounds in the region of 0≤y≤0.0235 are achievable in the XRD patterns of sample No. 4, 11, and 12 in Fig. 5.2(b). With further increasing y over 0.0235, the second phase of TiO₂ starts to occur in Fig. 5.2(b), so that Sr_{0.9639(1-y)}Cu_{3.0361(1-3y)}Ti_{4+2y}O₁₂-type solid solutions are firstly discovered in the present investigation.

The subsolidus phase compatibilities of samples (from No.15 to No.21) in the SrO-rich region over >~36.8% are determined using the powder XRD at 950°C in air as shown in Fig. 5.3. The pseudo-binary compounds of Sr₂TiO₄,

$\text{Sr}_3\text{Ti}_2\text{O}_7$, $\text{Sr}_4\text{Ti}_3\text{O}_{10}$, SrTiO_3 , and $\text{SrTi}_{11}\text{O}_{20}$ have been reported in the Sr-Ti-O system. The Sr_2TiO_4 and $\text{Sr}_3\text{Ti}_2\text{O}_7$ compounds, which show body-centered tetragonal structure with $a=3.88 \text{ \AA}$, $c=12.60 \text{ \AA}$ and $a=3.90 \text{ \AA}$, $c=20.38 \text{ \AA}$, respectively, were first prepared by Ruddlesden *et al.* [11-12] According to the previous studies by McCarthy *et al.* [13], and Tilley *et al.* [14], the Sr_2TiO_4 and $\text{Sr}_3\text{Ti}_2\text{O}_7$ compounds could be prepared in the temperature ranging from 1513 to 1673 K. In addition, Wei *et al.* [15] was able to obtain the above two stable phases below 1300 K.

The pure phase $\text{Sr}_4\text{Ti}_3\text{O}_{10}$ compound, which was unstable below 1648 K, was firstly synthesized by McCarthy *et al.* [13] after thermal heat treatment over a week at 1748 K. The crystal structure was also body-centered tetragonal cell of $a=3.903 \text{ \AA}$ and $c=28.14 \text{ \AA}$.

The SrTiO_3 is a cubic perovskite with $a=3.905 \text{ \AA}$ in JCPDS (No. 35-0734). Kestigian *et al.* [16] first reported that the $\text{SrTiO}_{3-\delta}$ compounds remained the cubic structure within the whole reduction range from $0 \leq \delta \leq 0.5$.

Hessen *et al.* [17] prepared the $\text{SrTi}_{11}\text{O}_{20}$ compound and insisted that the $\text{SrTi}_{11}\text{O}_{20}$ could be produced by the mixture of reduced $\text{SrTiO}_{2.5}$ and borate flux of $\text{SrO} \cdot 2\text{B}_2\text{O}_3$ in high vacuum condition. On the basis of the above investigations, only three phases of Sr_2TiO_4 , $\text{Sr}_3\text{Ti}_2\text{O}_7$ and SrTiO_3 are stable pseudo-binary phases in our experimental conditions.

The following four pseudo-binary compounds: Sr_2CuO_3 , SrCuO_2 , SrCu_2O_3 , and $\text{Sr}_{14}\text{Cu}_{24}\text{O}_{41}$ have been identified in the Sr-Cu-O system and the Sr_2CuO_3 , SrCuO_2 , and $\text{Sr}_{14}\text{Cu}_{24}\text{O}_{41}$ compounds known to be stable at 950°C in air. The Sr_2CuO_3 and SrCuO_2 compounds, which were first reported by Teske *et al.* [18-19] are found to melt incongruently at 1085°C and 1225°C , respectively,

and the eutectic temperature of $\text{Sr}_{14}\text{Cu}_{24}\text{O}_{41}$ is known to be $955^{\circ}\pm 4^{\circ}\text{C}$ as shown in the binary phase diagram of SrO-CuO system. [20] An additional pseudo-binary SrCu_2O_3 compound could be observable under the lower oxygen partial pressure. [21-23] In our experimental conditions, only Sr_2CuO_3 , SrCuO_2 , and $\text{Sr}_{14}\text{Cu}_{24}\text{O}_{41}$ are stable pseudo-binary compounds. Numerous tie lines between the STO and $\text{SrCu}_{3.15}\text{Ti}_{4.3}\text{O}_{12+\delta}$, STO and CuO, STO and $\text{Sr}_{14}\text{Cu}_{24}\text{O}_{41}$, STO and SrCuO_2 , $\text{Sr}_3\text{Ti}_2\text{O}_7$ and SrCuO_2 , Sr_2TiO_4 and SrCuO_2 , and Sr_2TiO_4 and Sr_2CuO_3 compounds exist in Fig. 5.3 (b)~(h). On the basis of the above phase boundaries and solid solutions in Fig. 5.1, 5.2, and 5.3, the subsolidus phase diagram in the SrO-CuO-TiO₂ ternary system is successfully identified at 950°C in air as shown in Fig. 5.5.

The lattice constant measurement for the solid solutions was performed and represented in Fig. 5.5, indicating that no remarkable variation in the lattice parameter was observable. The frequency dependent ϵ_r and $\tan\delta$ properties in Fig. 5.6 indicate that all samples in the solid solution region show the CDR. Further investigations for revealing the electrical properties of grain and grain boundary in each sample using impedance (Z^*) and modulus (M^*) spectroscopy analyses are required.

5.3.2 CaO-CuO-TiO₂ ternary system

The stoichiometric CCTO always show the severe CuO segregation on sample surface after thermal etching process at 900°C for 1 h in air so that we selected several nominal compositions from sample No. 1 to 7 by decreasing the amount of CuO and investigated the phase relations. As

shown in the powder XRD patterns in Fig. 5.7, no second phases are observable with decreasing x from 0 to -0.0191 but the second phases of CaTiO_3 and TiO_2 start to occur with further decreasing x to -0.0526. At this stage, the reason for the existence of TiO_2 phase is unclear so that further investigations around sample No. 5 are required. Figure 5.7 (c) shows the powder XRD patterns of sample No. 8, 9, 10, and 11, indicating that the second phases of TiO_2 and CuO are observed so that sample No. 11 should be in the compatibility triangle among sample No. 10, TiO_2 and CuO .

For identifying the existence of solid solution in the CaO-CuO-TiO_2 ternary system, we selected various nominal compositions from sample No. 12 to 15 and No. 16 to 19 around sample No. 4 and 10, respectively, as shown in Fig. 5.8(a). On the basis of the powder XRD analysis in Fig. 5.8 (b), the second phases of CaTiO_3 and CuO are observed with increasing y from 0.0043 to 0.0397 in the $\text{Ca}_{1.0191(1+y)}\text{Cu}_{2.9809(1+y)}\text{Ti}_{4-2y}\text{O}_{12}$ compounds so that sample No. 12 to 15 should be in the compatibility triangle among sample No.4, CaTiO_3 , and CuO . While only the second phase of CuO appears in the sample No. 16, sample No. 17 to 19 include only TiO_2 second phase in Fig. 5.8(c) of which results indicate that sample No. 16 and sample No. 17, 18, and 19 should be in the compatibility triangle among sample No. 4, CuO , and 10 and on the tie line between sample No. 10 and TiO_2 , respectively.

The existence of the tie line between sample No. 4 and CuO could be clarified by investigating the powder XRD patterns of sample No. 20, 21, and 22 as shown in Fig. 5.9 (c). In Fig. 5.9(c), only two phases of CuO and CCTO appear and the tie line between sample No. 4 and CuO should exist.

Similarly, the existence of the tie lines between sample No. 4 and TiO_2 and sample No. 4 and CaTiO_3 could be clarified by analyzing the powder XRD patterns of sample No. 25 and 26, respectively, in Fig. 5.9(b). As shown in Fig. 5.9(b), only the two phases of TiO_2 & CCTO, and CaTiO_3 & CCTO are compatible with sample No. 25 and 26, respectively, implying that the two tie lines should exist.

The two compounds of CaTiO_3 and $\text{Ca}_3\text{Ti}_2\text{O}_7$ have been identified in the Ca-Ti-O system by previous studies [24-25] but the $\text{Ca}_3\text{Ti}_2\text{O}_7$ compound is only stable at above 1200°C in air and the compound melts incongruently at $\sim 1750^\circ\text{C}$ in air so that only CaTiO_3 is observed in our experimental conditions.

The CaCu_2O_3 [26], Ca_2CuO_3 [27], and $\text{Ca}_3\text{Cu}_7\text{O}_{10}$ [27] compounds exist in the Ca-Cu-O system but Ca_2CuO_3 compound is only stable in our experimental condition.

The pseudo-binary compounds of Cu_2TiO_3 [28], Cu_3TiO_4 [29], Cu_3TiO_5 [30], $\text{Cu}_3\text{Ti}_3\text{O}$ [31] and $\text{Cu}_2\text{Ti}_4\text{O}$ [32] have been reported in the Cu-Ti-O system. According to Hennings *et al.* [27], the Cu_3TiO_4 compound is stable only above 867°C with hexagonal cell structure of $a=3.05 \text{ \AA}$ and $c=11.5 \text{ \AA}$ but its composition fluctuates between $\text{Cu}_3\text{TiO}_{3.9}$ and $\text{Cu}_3\text{TiO}_{4.3}$. The eutectic temperature between CuO and TiO_2 was estimated to 1020°C in air by Lu *et al.* [29] Kelkar *et al.* [30].

On the basis of the above literature survey, the subsolidus phase relations in the CaO-rich region over 50% are identified by the powder XRD patterns of sample No. 23 and 24 in Fig. 5.9(b). Finally, the subsolidus phase diagram in the CaO-CuO- TiO_2 ternary system is successfully identified at 950°C in air as shown in Fig. 5.10. The new type of $\text{Ca}_{1-x}\text{Cu}_{3+x}\text{Ti}_4\text{O}_{12}$ ($0.0191 \leq x \leq 0.0476$) solid solutions is firstly identified in the present study.

The lattice constant measurement with Si powder for the various solid solutions (sample No.4, 3, 2, 1, 8, 9, and 10) was performed and represented in Fig. 5.11(d), indicating that no remarkable variation in the lattice parameter was observable although no second phases appeared in Fig. 5.11(a). Further investigations for clarifying the detailed chemical composition using HR-TEM are required.

Meanwhile, as mentioned previously, abnormally grown large grains are frequently observable in CCTO ceramics due to the presence of CuO-rich liquid phase at grain boundary during sintering at 1060°C for 12 h in air. Therefore, we tried to identify the chemical composition of liquid phase by investigating the powder XRD patterns of solid solutions after sintering at 1050°C for 24 h. Fig. 5.12(a) represents the powder XRD patterns of solid solutions, implying that no second phases related to the CuO are observable. The variation of lattice constant in the solid solutions after sintering is negligibly small in Fig. 5.12(d). However, as shown in the surface images of solid solutions after sintering at 1050°C for 24 h in Fig. 5.13(a), sample No. 10 is composed of abnormally grown large grains and the microstructure is quite similar to the conventional CCTO ceramics. On the basis of the subsolidus phase diagram in Fig. 5.13(b), the composition of sample No.10 is adjacent to the eutectic composition of CuO-TiO₂ binary system so that abnormal grain growth in the sample No.10 could be attributed to the eutectic liquid phase during sintering at 1050°C for 24 h in air because the eutectic temperature in the CuO-TiO₂ binary system was estimated to 1020°C in air by Lu *et al.* [29] Kelkar *et al.* [30].

5.4. Summary

The subsolidus phase relations in the SrO-CuO-TiO₂ and CaO-CuO-TiO₂ ternary systems have been investigated at 950°C in air. The stoichiometric SrCu₃Ti₄O₁₂ compound did not exist but the single phase composition was revealed to Sr_{0.9639}Cu_{3.0361}Ti₄O₁₂ and Sr_{0.9639(1-y)}Cu_{3.0361(1-3y)}Ti_{4+2y}O₁₂-type solid solutions existed in the region of 0 ≤ y ≤ 0.0235. The variation in the lattice parameters of these solid solutions was negligibly small. The ε_r values of the samples in the solid solution region were over ~70,000 at 1 kHz. Further investigations for understanding the electrical properties of grain and grain boundary using Z* & modulus M* spectroscopy are required.

In the CaO-CuO-TiO₂ ternary system, Ca_{1-x}Cu_{3+x}Ti₄O₁₂-type solid solutions existed in a wide region of -0.0191 ≤ x ≤ 0.0476 at 950°C in air. The abnormal grain growth in CCTO ceramics could be due to an eutectic liquid phase between CuO and TiO₂ compounds although the liquid phase was undetectable by XRD patterns after sintering at 1050°C for 24 h. Further investigations by HR-TEM are required for the clarification of Ca_{1-x}Cu_{3+x}Ti₄O₁₂-type solid solutions.

References

- [1] M. A. Subramanian et al., *J. Solid State Chem.*, **151**, 323 (2000)
- [2] C. H. Mu et al., *J. Alloys. Compd.*, 471, 137 (2009)
- [3] M. Li et al., *Appl. Phys. Lett.*, 88, 232903 (2006)
- [4] S. F. Shao et al., *Appl. Phys. Lett.*, 91, 042905 (2007)
- [5] J. Cai et al., *Appl. Phys. Lett.*, 91, 252905 (2007)
- [6] S. W. Choi et al., *J. Am. Ceram. Soc.*, 90, 4009 (2007)
- [7] J. Li et al., *Chem. Mater.*, 16, 5223 (2004)
- [8] S. Y. Lee et al., *Electron. Mater. Lett.*, 3, 23 (2007)
- [9] T. T. Fang et al., *Acta. Mater.*, 54, 2867 (2006)
- [10] S. Y. Lee et al., *Electron. Mater. Lett.*, 7, 287 (2011)
- [11] S. N. Ruddlesden et al., *Acta. Cryst.*, 10, 538 (1957)
- [12] S. N. Ruddlesden et al., *ibid.*, 11, 54 (1958)
- [13] G. J. McCarthy et al., *J. Am. Ceram. Soc.*, 52, 463 (1969)
- [14] R. J. D. Tilley et al., *J. Solid. State. Chem.*, 21, 293 (1977)
- [15] Z. F. Wei et al., *J. Alloys. Compd.*, 327, L10 (2001)
- [16] M. Kestigian et al., *J. Am. Chem. Soc.*, 79, 5598 (1957)
- [17] B. Hossen et al., *J. Solid. State. Chem.*, 94, 306 (1991)
- [18] C. L. Teske et al., (in Ger.), *Z. Anorg. Allg. Chem.*, 371, 325 (1969)
- [19] C. L. Teske et al., (in Ger.), *Z. Ang. Allg. Chem.*, 379, 234 (1970)
- [20] R. S. Roth et al., *J. Am. Ceram. Soc.*, 72, 395 (1989)
- [21] J. C. Grivel et al., *J. Alloys. Compd.*, 464, 457 (2008)
- [22] C. B. Alcock et al., *J. Am. Ceram. Soc.*, 73, 1176 (1990)
- [23] C. L. Teske et al., *Z. Ang. Allg. Chem.*, 379, 113 (1970)
- [24] H. C. Fitt et al., *J. Am. Ceram. Soc.*, 34, 9 (1951)
- [25] R. C. Devries et al., *J. Phys. Chem.*, 58, 1069 (1954)
- [26] C. L. Teske et al., *Z. Ang. Allg. Chem.*, 370, 134 (1970)
- [27] M. L. Carvalho et al., *Physica C.*, 336, 1 (2000)

- [28] N. G. Schmahl et al., *Z. Ang. Allg. Chem.*, 332, 12 (1964)
- [29] D. Hennings et al., *J. Solid. State. Chem.*, 31, 275 (1980)
- [30] A. A. Slobodoyanyuk et al., *Russ. J. Inorg. Chem.*, 17, 922 (1972)
- [31] F. H. Lu et al., *J. Eur. Ceram. Soc.*, 21, 1093 (2001)
- [32] G. P. Kelkar et al., *J. Am. Ceram. Soc.*, 76, 1815 (1993)

Table 5.1 The selected nominal compositions and phases observed at 950°C in air in the SrO-CuO-TiO₂ ternary system

Sample No	Nominal compositions			Phases observed
	SrO	CuO	TiO ₂	
1. SrCu ₃ Ti ₄ O ₁₂	0.1250	0.3750	0.5	SrCu ₃ Ti ₄ O ₁₂ , SrTiO ₃
2. SrCu _{0.9756} Cu _{3.0244} Ti ₄ O ₁₂	0.1220	0.3780	0.5	SrCu ₃ Ti ₄ O ₁₂ , SrTiO ₃
3. Sr _{0.9897} Cu _{3.0303} Ti ₄ O ₁₂	0.1212	0.3788	0.5	SrCu ₃ Ti ₄ O ₁₂ , SrTiO ₃
4. Sr_{0.9639}Cu_{3.0361}Ti₄O₁₂	0.1205	0.3795	0.5	SrCu₃Ti₄O₁₂
5. Sr _{0.9581} Cu _{3.0419} Ti ₄ O ₁₂	0.1198	0.3802	0.5	SrCu ₃ Ti ₄ O ₁₂ , CuO
6. Sr _{0.9524} Cu _{3.0476} Ti ₄ O ₁₂	0.1190	0.3810	0.5	SrCu ₃ Ti ₄ O ₁₂ , CuO
7. Sr _{0.9412} Cu _{3.0588} Ti ₄ O ₁₂	0.1176	0.3824	0.5	SrCu ₃ Ti ₄ O ₁₂ , CuO
8. Sr _{0.9302} Cu _{3.0698} Ti ₄ O ₁₂	0.1163	0.3837	0.5	SrCu ₃ Ti ₄ O ₁₂ , CuO
9. Sr _{0.9091} Cu _{3.0909} Ti ₄ O ₁₂	0.1136	0.3864	0.5	SrCu ₃ Ti ₄ O ₁₂ , CuO
10. Sr _{0.9756} Cu _{3.0732} Ti _{3.9756} O ₁₂	0.1216	0.3830	0.4954	SrCu ₃ Ti ₄ O ₁₂ , CuO
11. Sr_{0.9524}Cu₃Ti_{4.0238}O₁₂	0.1194	0.3761	0.5045	SrCu₃Ti₄O₁₂
12. Sr_{0.9412}Cu_{2.9647}Ti_{4.0471}O₁₂	0.1183	0.3728	0.5089	SrCu₃Ti₄O₁₂
13. Sr _{0.9339} Cu _{2.9416} Ti _{4.0623} O ₁₂	0.1176	0.3706	0.5118	SrCu ₃ Ti ₄ O ₁₂ , TiO ₂
14. Sr _{0.9266} Cu _{2.9189} Ti _{4.0772} O ₁₂	0.1170	0.3684	0.5146	SrCu ₃ Ti ₄ O ₁₂ , TiO ₂
15. Sr _{2.4470} Cu _{1.4753} Ti _{4.0398} O ₁₂	0.3074	0.1853	0.5073	SrCu ₃ Ti ₄ O ₁₂ , SrTiO ₃
16. Sr _{3.1925} Cu _{2.4231} Ti _{3.1922} O ₁₂	0.3625	0.2751	0.3624	SrTiO ₃ , CuO
17. Sr _{4.1355} Cu _{2.3080} Ti _{2.7782} O ₁₂	0.4485	0.2503	0.3013	Sr ₁₄ Cu ₂₄ O ₄₁ , SrTiO ₃
18. Sr _{4.9066} Cu _{2.6756} Ti _{2.2089} O ₁₂	0.5011	0.2733	0.2256	SrCuO ₂ , SrTiO ₃
19. Sr _{5.3482} Cu _{1.3451} Ti _{2.6544} O ₁₂	0.5720	0.1439	0.2840	SrCuO ₂ , Sr ₃ Ti ₂ O ₇
20. Sr _{6.2999} Cu _{1.5951} Ti _{2.0525} O ₁₂	0.6333	0.1604	0.2063	SrCuO ₂ , Sr ₂ TiO ₄
21. Sr _{6.7806} Cu _{1.5698} Ti _{1.8247} O ₁₂	0.6664	0.1543	0.1793	Sr ₂ CuO ₃ , Sr ₂ TiO ₄

The samples from No. 1 to 9 and No. 10 to 14 are represented by the chemical formulae of Sr_{1-x}Cu_{3+x}Ti₄O₁₂ (0 ≤ x ≤ 0.0909) and Sr_{0.9639(1-y)}Cu_{3.0361(1-y)}Ti_{4+2y}O₁₂ (-0.0121 ≤ y ≤ 0.0386), respectively.

Table 5.2 The selected nominal compositions and phases observed at 950°C in air in the CaO-CuO-TiO₂ ternary system

Sample No	Nominal compositions			Phases Observed
	CaO	CuO	TiO ₂	
1. CaCu ₃ Ti ₄ O ₁₂	0.1250	0.3750	0.5	CaCu ₃ Ti ₄ O ₁₂
2. Ca _{1.0063} Cu _{2.9937} Ti ₄ O ₁₂	0.1258	0.3742	0.5	CaCu ₃ Ti ₄ O ₁₂
3. Ca _{1.0127} Cu _{2.9873} Ti ₄ O ₁₂	0.1266	0.3734	0.5	CaCu ₃ Ti ₄ O ₁₂
4. Ca _{1.0191} Cu _{2.9809} Ti ₄ O ₁₂	0.1274	0.3726	0.5	CaCu ₃ Ti ₄ O ₁₂
5. Ca _{1.0256} Cu _{2.9744} Ti ₄ O ₁₂	0.1282	0.3718	0.5	CaCu ₃ Ti ₄ O ₁₂ , CaTiO ₃
6. Ca _{1.0390} Cu _{2.9610} Ti ₄ O ₁₂	0.1299	0.3701	0.5	CaCu ₃ Ti ₄ O ₁₂ , CaTiO ₃ , TiO ₂
7. Ca _{1.0526} Cu _{2.9474} Ti ₄ O ₁₂	0.1316	0.3684	0.5	CaCu ₃ Ti ₄ O ₁₂ , CaTiO ₃ , TiO ₂
8. Ca _{0.9877} Cu _{3.0123} Ti ₄ O ₁₂	0.1235	0.3765	0.5	CaCu ₃ Ti ₄ O ₁₂
9. Ca _{0.9756} Cu _{3.0244} Ti ₄ O ₁₂	0.1220	0.3780	0.5	CaCu ₃ Ti ₄ O ₁₂
10. Ca _{0.9524} Cu _{3.0476} Ti ₄ O ₁₂	0.1190	0.3810	0.5	CaCu ₃ Ti ₄ O ₁₂
11. Ca _{0.9302} Cu _{3.0698} Ti ₄ O ₁₂	0.1163	0.3837	0.5	CaCu ₃ Ti ₄ O ₁₂ , TiO ₂ , CuO
12. Ca _{1.0236} Cu _{2.9936} Ti _{3.9915} O ₁₂	0.1278	0.3738	0.4984	CaCu ₃ Ti ₄ O ₁₂ , CaTiO ₃
13. Ca _{1.0323} Cu _{3.0194} Ti _{3.9742} O ₁₂	0.1286	0.3762	0.4952	CaCu ₃ Ti ₄ O ₁₂ , CaTiO ₃ , CuO
14. Ca _{1.0412} Cu _{3.0456} Ti _{3.9566} O ₁₂	0.1294	0.3786	0.4919	CaCu ₃ Ti ₄ O ₁₂ , CaTiO ₃ , CuO
15. Ca _{1.0596} Cu _{3.0993} Ti _{3.9205} O ₁₂	0.1311	0.3836	0.4852	CaCu ₃ Ti ₄ O ₁₂ , CaTiO ₃ , CuO
16. Ca _{0.9677} Cu _{3.0966} Ti _{3.9677} O ₁₂	0.1205	0.3855	0.4940	CaCu ₃ Ti ₄ O ₁₂ , CuO
17. Ca _{0.9375} Cu ₃ Ti _{4.0313} O ₁₂	0.1176	0.3765	0.5059	CaCu ₃ Ti ₄ O ₁₂ , TiO ₂
18. Ca _{0.9231} Cu _{2.9538} Ti _{4.0615} O ₁₂	0.1163	0.3721	0.5116	CaCu ₃ Ti ₄ O ₁₂ , TiO ₂
19. Ca _{0.9091} Cu _{2.9091} Ti _{4.0909} O ₁₂	0.1149	0.3678	0.5172	CaCu ₃ Ti ₄ O ₁₂ , TiO ₂
20. Ca _{1.0169} Cu ₃ Ti _{3.9915} O ₁₂	0.1270	0.3746	0.4984	CaCu ₃ Ti ₄ O ₁₂ , CuO
21. Ca _{1.0127} Cu _{3.0380} Ti _{3.9747} O ₁₂	0.1262	0.3785	0.4953	CaCu ₃ Ti ₄ O ₁₂ , CuO
22. Ca _{1.0042} Cu _{3.1130} Ti _{3.9414} O ₁₂	0.1246	0.3863	0.4891	CaCu ₃ Ti ₄ O ₁₂ , CuO
23. Ca _{3.1291} Cu _{2.6096} Ti _{3.1306} O ₁₂	0.3528	0.2942	0.3530	CaTiO ₃ , CuO
24. Ca _{5.8204} Cu _{1.8177} Ti _{2.1809} O ₁₂	0.5928	0.1851	0.2221	CaTiO ₃ , Ca ₂ CuO ₃
25. Ca _{0.9697} Cu _{2.8364} Ti _{4.0970} O ₁₂	0.1227	0.3589	0.5184	CaCu ₃ Ti ₄ O ₁₂ , TiO ₂
26. Ca _{1.1429} Cu _{2.8571} Ti ₄ O ₁₂	0.1429	0.3571	0.5	CaCu ₃ Ti ₄ O ₁₂ , CaTiO ₃

The samples from No.1 to 11, No.12 to 15, No.16 to 19, and No.20 to 22 are represented by the chemical formulae of Ca_{1-x}Cu_{3+x}Ti₄O₁₂ (-0.0526 ≤ x ≤ 0.0698), Ca_{1.0191(1+y)}Cu_{2.9809(1+y)}Ti_{4-2y}O₁₂ (0.0043 ≤ y ≤ 0.0397), Ca_{0.952-z}Cu_{3.047-3z}Ti_{4+2z}O₁₂ (-0.0160 ≤ z ≤ 0.0454), and Ca_{1.0191(1-w)}Cu_{2.9809+9.0191w}Ti_{4-4w}O₁₂ (0.0021 ≤ w ≤ 0.0146), respectively.

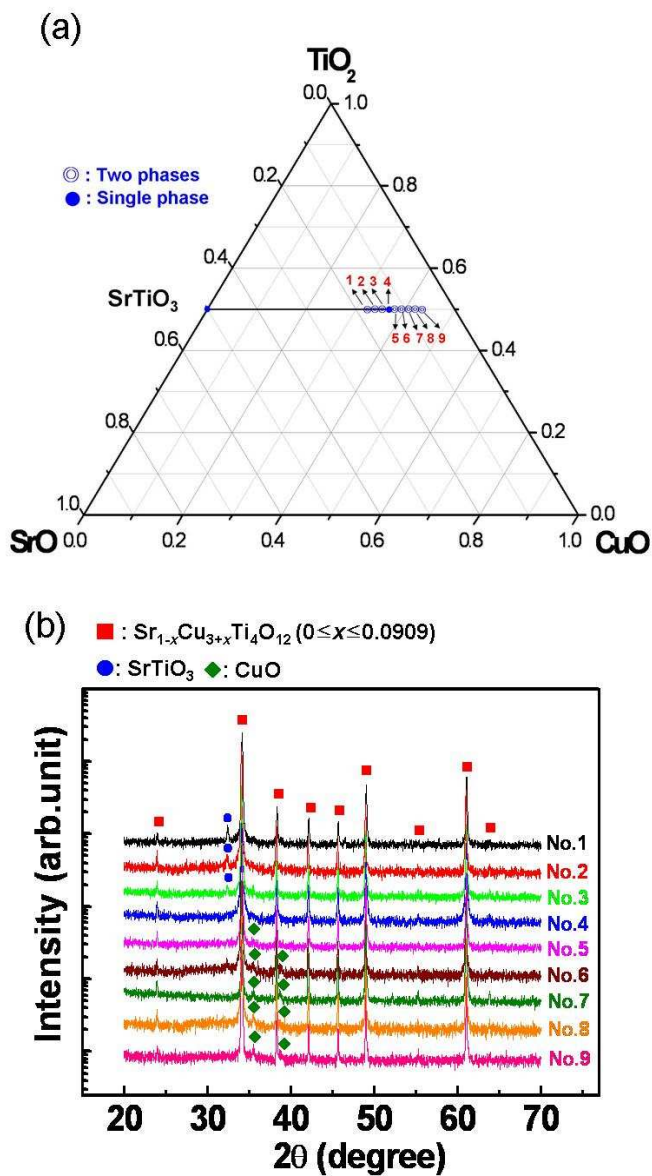


Fig. 5.1 The selected compositions in the $\text{Sr}_{1-x}\text{Cu}_{3+x}\text{Ti}_4\text{O}_{12}$ ($0 \leq x \leq 0.0909$) compounds (a) and powder XRD patterns (b)

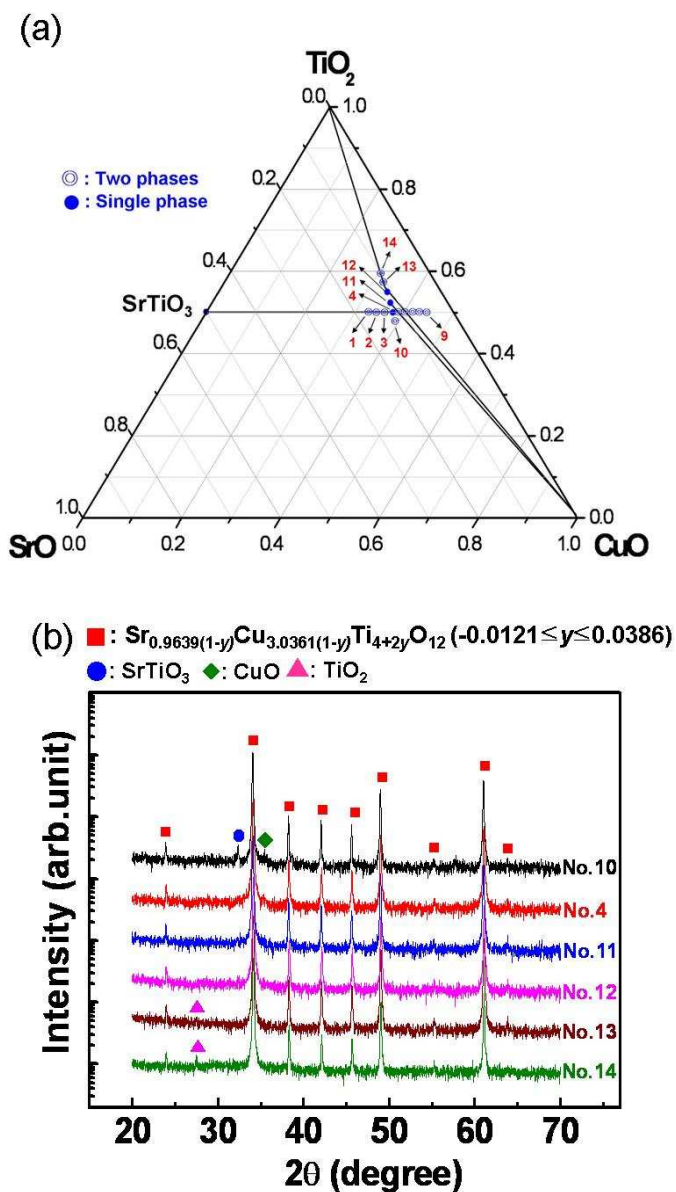


Fig. 5.2 The selected compositions in the $\text{Sr}_{0.9639(1-y)}\text{Cu}_{3.0361(1-y)}\text{Ti}_{4+2y}\text{O}_{12}$ ($-0.0121 \leq y \leq 0.0386$) compounds (a) and powder XRD patterns (b)

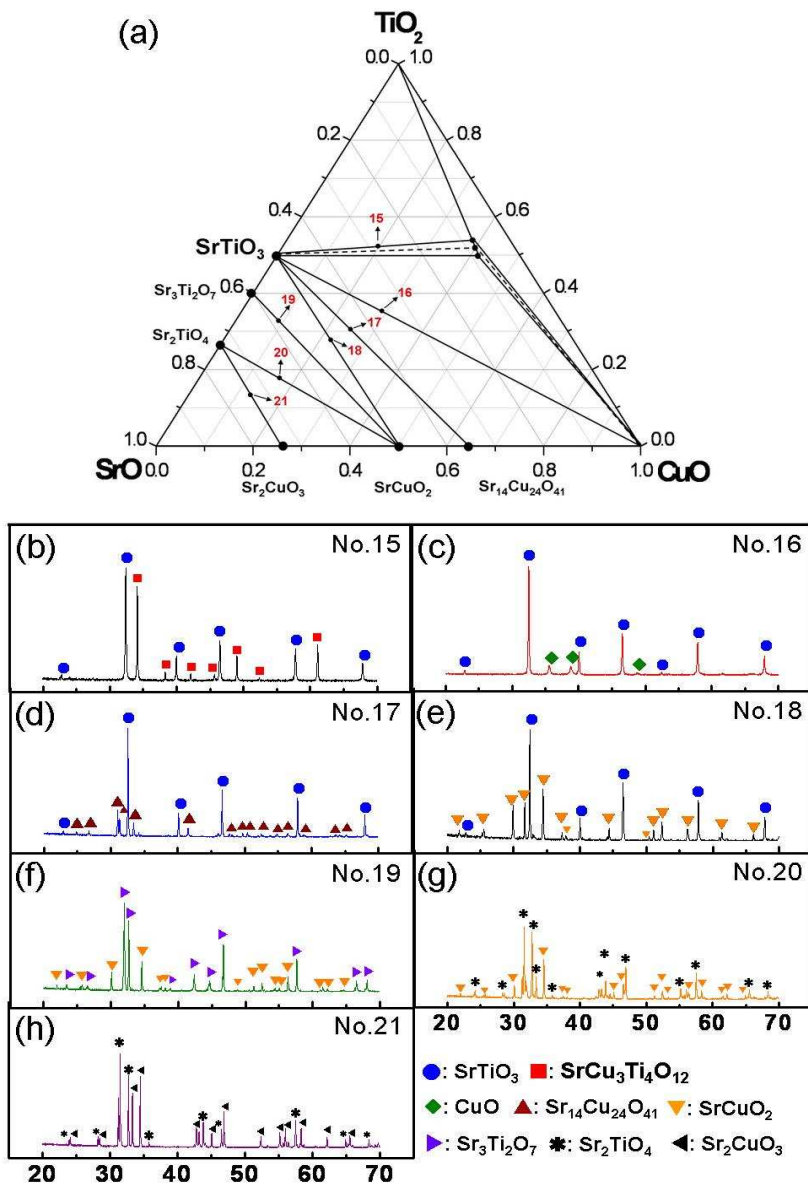


Fig. 5.3 The phase relations of the SrO-rich (SrO > ~36.8%) region in the SrO-CuO-TiO₂ ternary system (a), and powder XRD patterns of various samples No.15 (b), No.16 (c), No. 17 (d), No. 18 (e), No. 19 (f), No. 20 (g), and No. 21 (h)

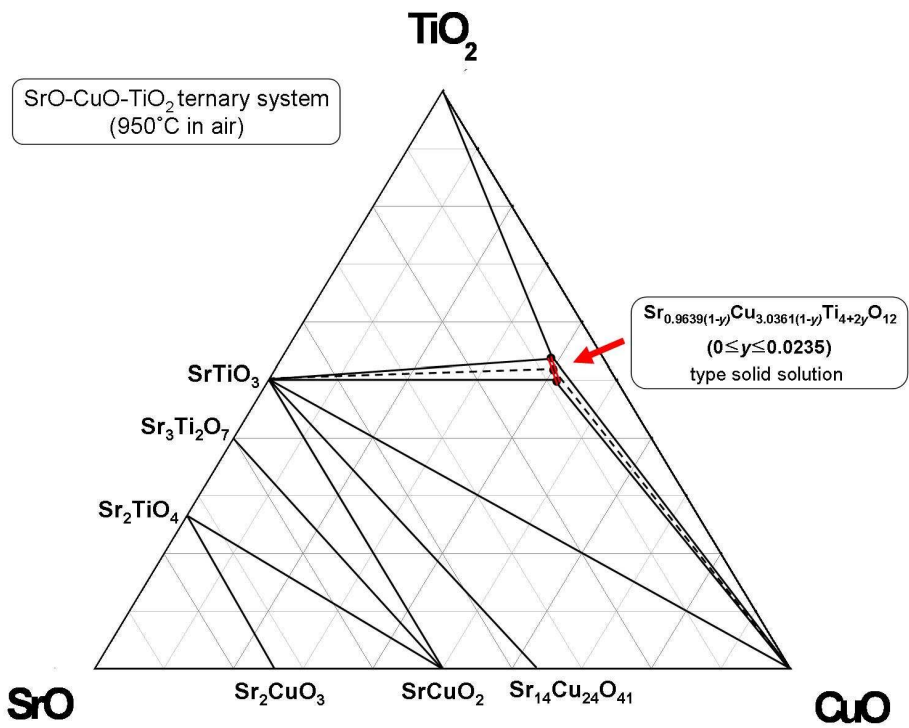


Fig. 5.4 The subsolidus phase diagram in the SrO-CuO-TiO₂ ternary system at 950°C in air

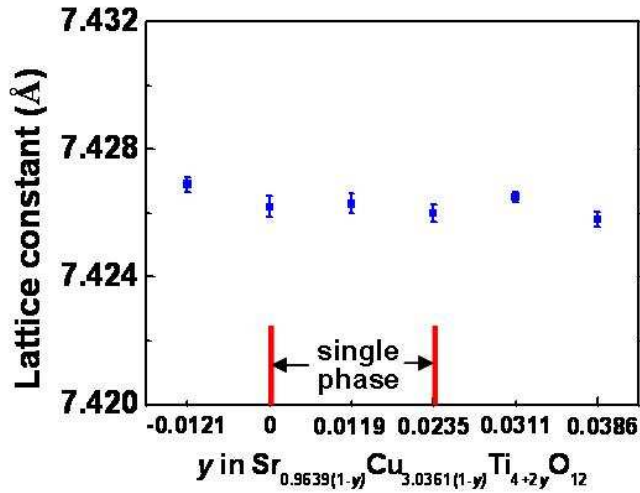


Fig. 5.5 The variation of lattice constant in the $\text{Sr}_{0.9639(1-y)}\text{Cu}_{3.0361(1-y)}\text{Ti}_{4+2y}\text{O}_{12}$ ($-0.0121 \leq y \leq 0.0386$) solid solutions

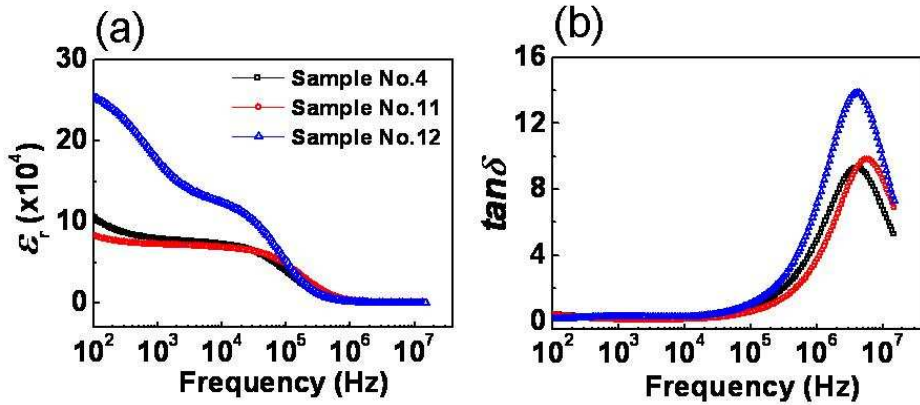


Fig. 5.6 Frequency dependent ϵ_r and $\tan\delta$ properties of $\text{Sr}_{0.9639(1-y)}\text{Cu}_{3.0361(1-y)}\text{Ti}_{4+2y}\text{O}_{12}$ -type solid solutions

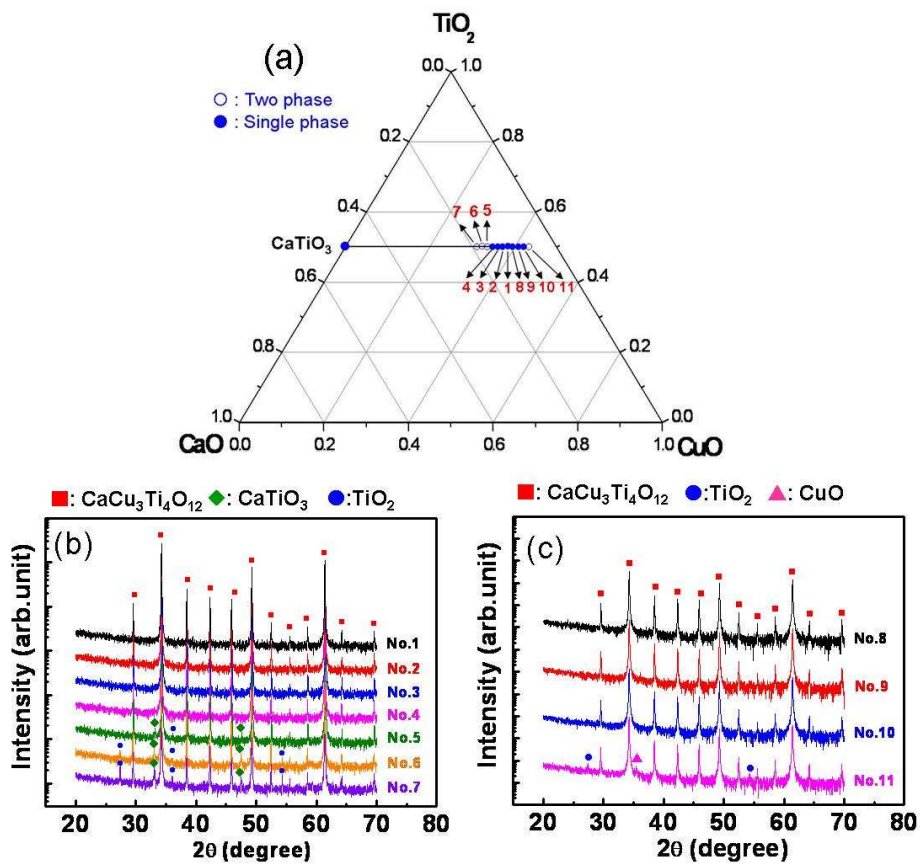


Fig. 5.7 The selected compositions in the $\text{Ca}_{1-x}\text{Cu}_{3+x}\text{Ti}_4\text{O}_{12}$ ($-0.0526 \leq x \leq 0.0698$) compounds (a) and powder XRD patterns (b) and (c)

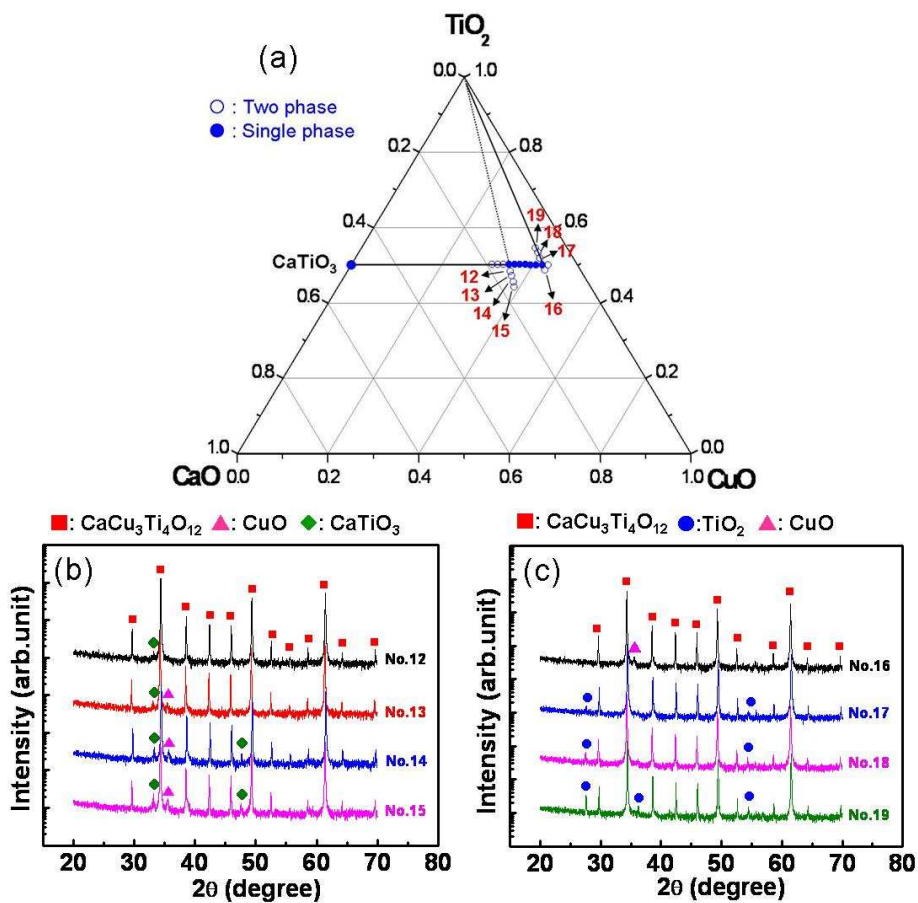


Fig. 5.8 The selected compositions in the $\text{Ca}_{1.0191(1+y)}\text{Cu}_{2.9809(1+y)}\text{Ti}_{4-2y}\text{O}_{12}$ ($0.0043 \leq y \leq 0.0397$) and $\text{Ca}_{0.952-z}\text{Cu}_{3.047-3z}\text{Ti}_{4+2z}\text{O}_{12}$ ($-0.0160 \leq z \leq 0.0454$) compounds (a) and powder XRD patterns (b) and (c)

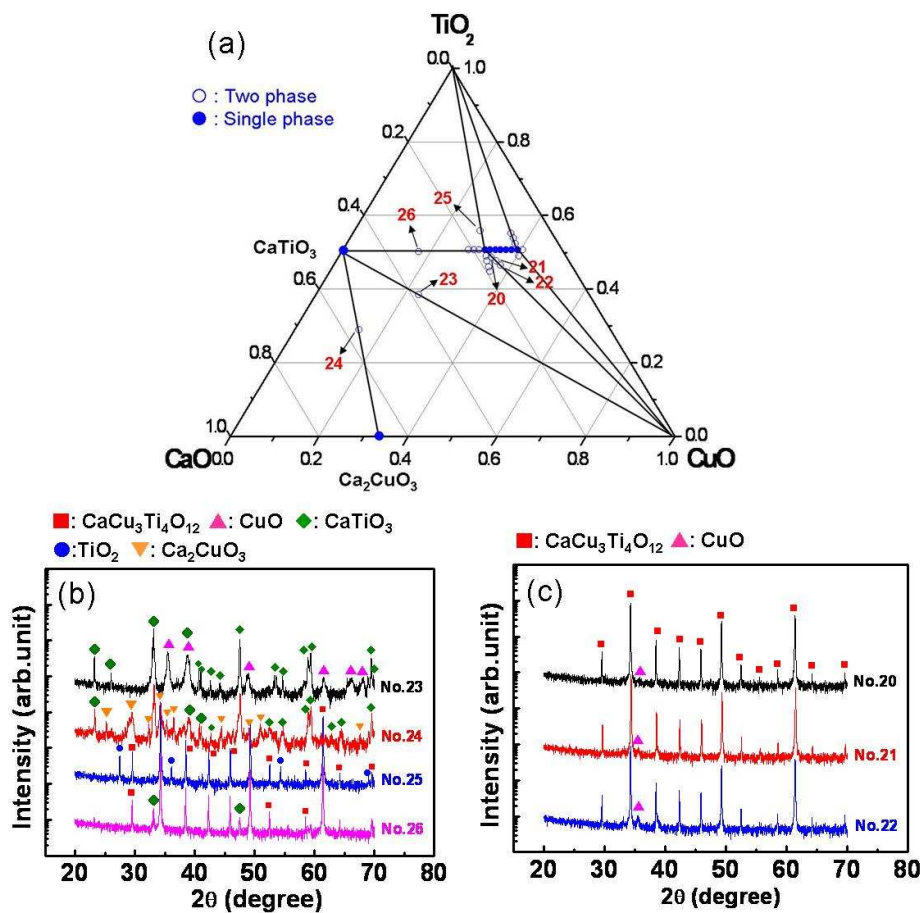


Fig. 5.9 The selected compositions in the $\text{Ca}_{1.0191(1-w)}\text{Cu}_{2.9809+9.0191w}\text{Ti}_{4-4w}\text{O}_{12}$ ($0.0021 \leq w \leq 0.0146$) compounds and the phase compatibilities of the sample No. 23, 24, 25, and 26 (a) and powder XRD patterns (b) and (c)

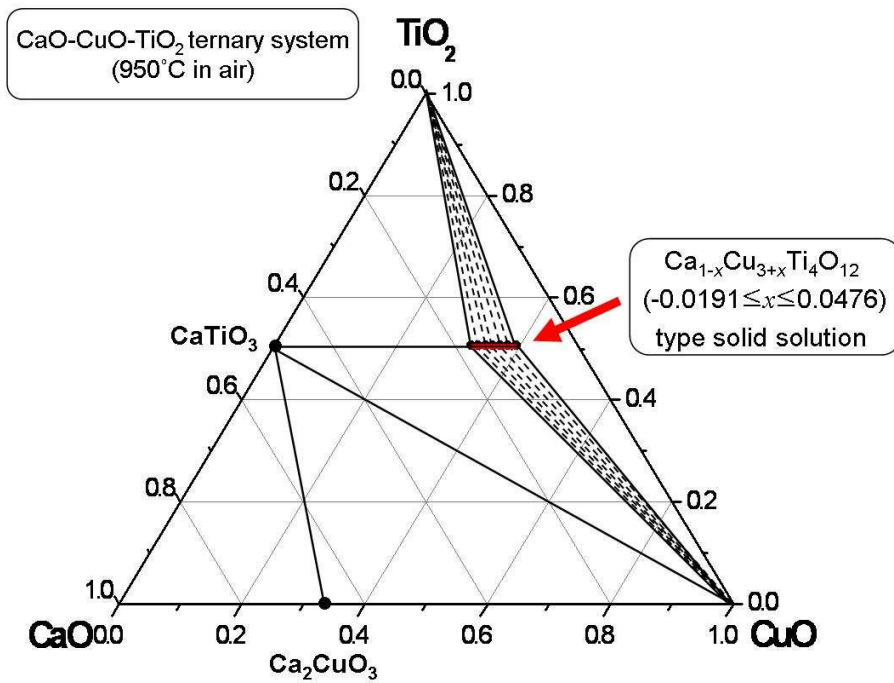


Fig. 5.10 The subsolidus phase diagram in the CaO-CuO-TiO₂ ternary system at 950°C in air

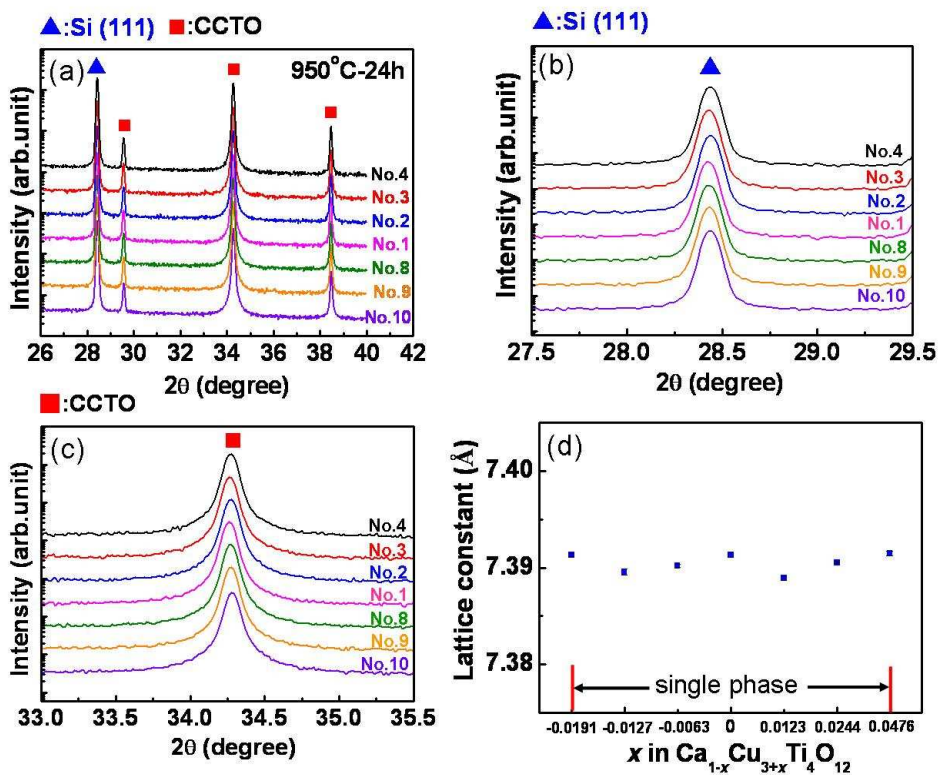


Fig. 5.11 The XRD patterns of samples from No.4 to No.10 at 950°C for 24 h in air with Si powder (a) enlarged XRD patterns of Si (b) enlarged XRD patterns of CCTO main peaks (c), and the variation of lattice constants in the $\text{Ca}_{1-x}\text{Cu}_{3+x}\text{Ti}_4\text{O}_{12}$ -type ($-0.0191 \leq x \leq 0.0476$) solid solutions

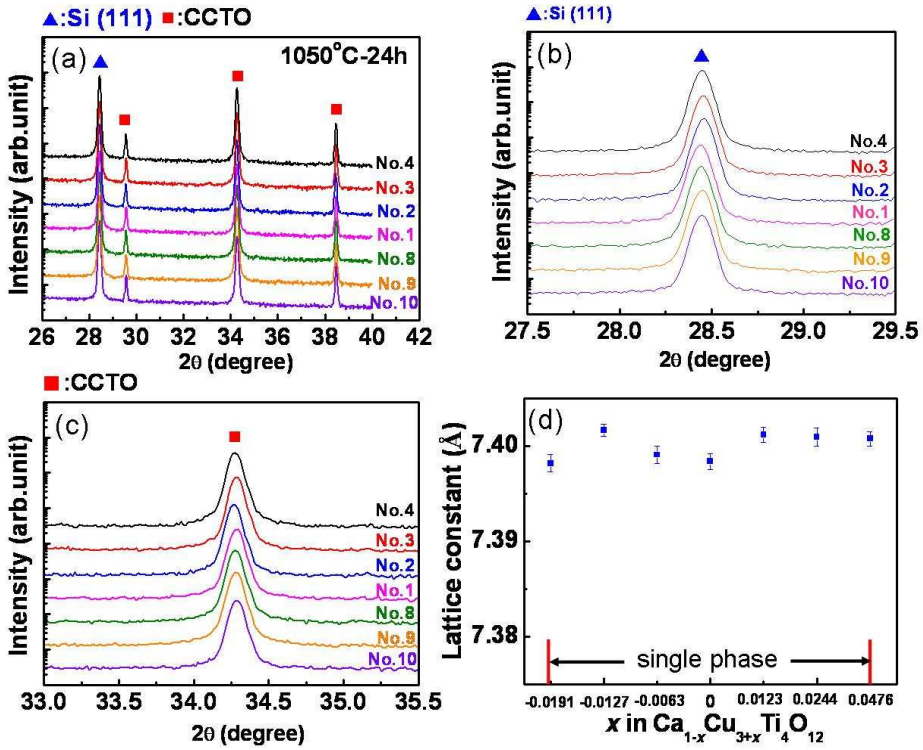


Fig. 5.12 The XRD patterns of samples from No.4 to No.10 at 1050°C for 24 h in air with Si powder (a) enlarged XRD patterns of Si (b) enlarged XRD patterns of CCTO main peaks (c), and the variation of lattice constants in the $\text{Ca}_{1-x}\text{Cu}_{3+x}\text{Ti}_4\text{O}_{12}$ -type ($-0.0191 \leq x \leq 0.0476$) solid solutions sintered at 1050°C for 24 h in air

(a)



(b)

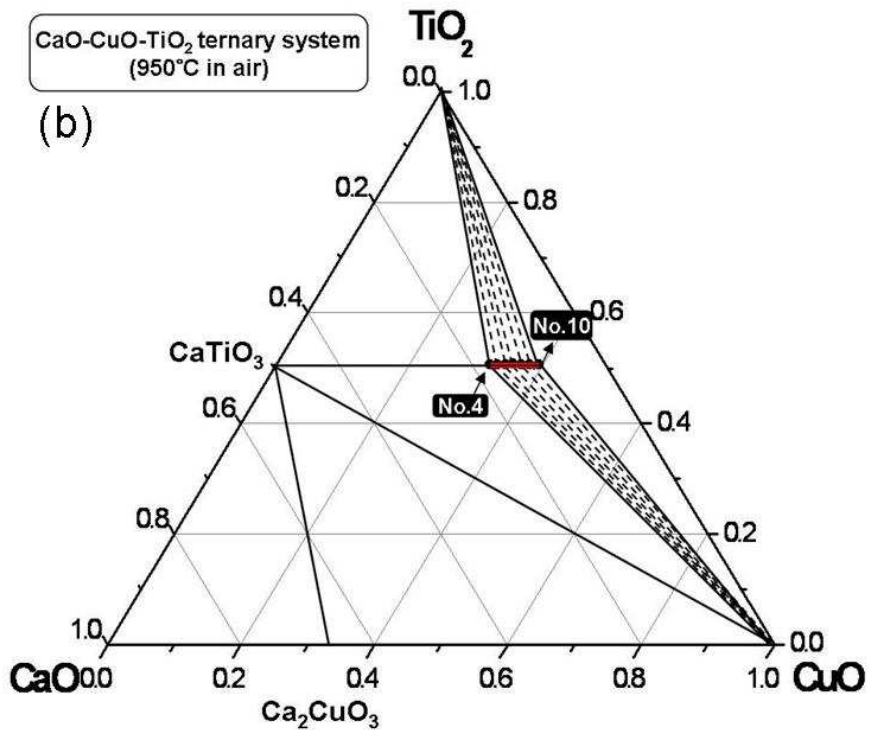


Fig. 5.13 The surface images of solid solutions after sintering at 1050°C for 24 h in air (a) and subsolidus phase diagram in the CaO-CuO-TiO₂ ternary system at 950°C in air (b).

Chapter 6. Dielectric Properties of Polycrystalline and Epitaxial CCTO Films

6.1. Introduction

The unprecedentedly high ϵ_r values of $\sim 10^4$ of the cubic perovskite CCTO ceramics without any phase transition over a wide temperature region of 100 ~ 600 K has drawn considerable attention for both its physical origin and practical applications.[1] First of all, related to the physical origin of the colossal dielectric response (CDR) of CCTO ceramics [2-6] and films[7-8], many research groups seem to accept the grain boundary IBLC model as the mechanism for CDR. The CDR is, however, observed also in CCTO single crystals [9-10] without grain boundaries, indicating that it is unexplainable only by the grain boundary IBLC model. Thus, for explaining the CDR in both CCTO ceramics and single crystals, it has been suggested as an alternative mechanism that CDR is attributable to the presence of insulating barriers such as domain boundaries [11-13] and twin boundaries [10, 14]. Recently, Ferrarelli *et al.*[15] have proposed that a non-ohmic contact between the electrodes (Au, InGa) and CCTO single crystal is responsible for CDR. Consequently, it can be said that the mechanism of CDR in CCTO is still controversial.

On the other hand, for practical applications, CCTO should be made in the form of film devices. Thus many research groups fabricated CCTO films and reported their properties [7-8, 16-37]. Up to date, various deposition

techniques, including PLD [7,16-28], sol-gel [8,29-33], sputtering [35-36], and MOCVD [37-38] have been employed for the fabrication of the CCTO films on Si substrates. As previously suggested by Li *et al.*[31], it is important to fabricate high quality CCTO films on Si substrates for real applications, including high capacitive dynamic random access memory. While the CCTO films fabricated on platinized Si substrates by PLD [7, 18-20, 24-28] show ϵ_r values in the region of 1,500~2,500 at 10 kHz, relatively low ϵ_r values below ~1,500 at 10 kHz are observable for the films on platinized Si substrates by the sol-gel technique [29-30, 32-33].

Most of CCTO films on platinized Si substrates by PLD are deposited at a fixed substrate temperature [7, 19-20, 24, 26-28]. Within the best of our knowledge, only one systematic study is available from Fang *et al.*[18]. They reported the effects of deposition temperature ranging from 450 to 700°C and oxygen pressure ranging from 2.66 to 26.6 Pa on the microstructures and dielectric properties of CCTO films. In contrast, in the deposition temperature region above 700°C, we have recently reported that the dielectric properties of CCTO films were remarkably varied by deposition temperature so that ϵ_r values at 10 kHz were increased from ~300 to ~2,000 with increasing deposition temperature from 700 to 750°C, respectively, and then decreased to ~ 900 at 800°C [25]. However, the reason for this variation in dielectric properties with deposition temperature has been unclarified yet. Therefore, in this study we tried to understand the effect of deposition temperature, ranging from 700 to 800°C, on the dielectric and leakage current properties of PLD-processed CCTO films on the Pt/TiO₂/SiO₂/Si substrates by carefully investigating detailed microstructures with HR-TEM and compositional

distributions of samples using various analysis methods, including EDS and EELS in HR-TEM, and AES. In addition, we tried to decrease the high $\tan\delta$ values and leakage current of CCTO films by adopting the additional CTO layer using the multi-layered structures of Pt/CTO/CCTO, Pt/CCTO/CTO, and Pt/CTO/CCTO/CTO due to the absence of chemical reactions between CCTO and CTO ceramics. The severe drop of ϵ_r values in multi-layered CCTO films were overcome by increasing the thickness of CCTO layer from ~200 nm to ~1.2 μm . Finally, we investigated the dielectric properties of epitaxial CCTO films with SRO bottom electrode on STO substrates because CCTO single crystals show much higher ϵ_r values than CCTO ceramics.

6.2. Experimental

The CCTO polycrystalline targets were fabricated by solid state reaction using CaCO_3 (Cerac, 99.95%), CuO (High Purity Chemicals, 99.99%) and TiO_2 (High Purity Chemicals, 99.99%). The mixed powder was ball-milled in ethyl alcohol using a polyethylene bottle with ZrO_2 balls for 24 h, and then uniaxially pressed into pellets and calcined at 950°C for 24 h in air. The as-calcined pellets were ball-milled for 24 h and further consolidated by cold isostatic pressing with 100 MPa. The samples were sintered in air at 1060°C for 12 h. The polycrystalline CCTO thin films were deposited on the Pt/ TiO_2 / SiO_2 /Si substrates by PLD using a KrF excimer laser ($\lambda=248$ nm). The CCTO target was ablated in 800mTorr O_2 at various substrate temperatures ranging from $700\sim 800^\circ\text{C}$. A laser pulse with a fluence of 1.6 J/cm^2 at 5 Hz pulse rate was used to grow CCTO thin films with a thickness

of about 500 nm. The as-grown CCTO films were cooled under the four possible combinations of cooling conditions; slow cooling ($3^{\circ}\text{C}/\text{min}$: from deposition temperature to 500°C) at high and low oxygen pressure of 66 kPa and 100 Pa, respectively and fast cooling ($\sim 20^{\circ}\text{C}/\text{min}$: from deposition temperature to 500°C) at high and low oxygen pressure. The CTO layer was deposited at 750°C for 30 min under the oxygen pressure of 200 mTorr using Nd-YAG ($\lambda=355\text{ nm}$) laser with a fluence of $1.6\text{ J}/\text{cm}^2$. For epitaxial CCTO films, the CCTO target was ablated in 800mTorr O_2 at 750°C with a fluence of $1.6\text{ J}/\text{cm}^2$ at 5 Hz to grow 500nm-epitaxial films. The SRO bottom electrode with a 200nm thickness was deposited on STO single crystal substrate at 700°C for 15min in 100 mTorr O_2 . The surface morphologies of CCTO thin films were observed by field-emission scanning electron microscopy (FESEM, NOVA NanoSEM 200 and JSM 6330F) with acceleration voltage of 10 kV and atomic force microscopy (Nanofocus Inc). The segregated nanoparticles on the polycrystalline CCTO film surface were identified using EPMA (JEOL JXA-8500F) with characteristic X-ray of $\text{Cu-K}\alpha$. The phase compositions and chemical reactions between Pt layer and CCTO films were analyzed by using high resolution XRD (BRUKER D8 ADVANCE and X'pert Pro, PANalytical) with θ - 2θ scan using $\text{Cu-K}\alpha$ radiation ($\lambda=1.54056\text{ \AA}$). The cross section images of CCTO films and segregated nano-crystallized TiO_2 at grain boundary were analyzed by using high resolution transmission electron microscopy (HR-TEM, JEOL-3000F) with an acceleration voltage of 300kV. The inter-diffusion at the interfaces of CCTO/Pt and Pt/ TiO_2 was identified using EDS analysis attached to the HR-TEM. The existence of the inter-metallic compound of PtCu_3 on the surface

of Pt electrode is identified using fast fourier transformation (FFT) image from the HR-TEM image of Pt electrode. The stoichiometry of nanocrystallized TiO₂ was confirmed using electron energy loss spectroscopy (EELS, Gatan) attached to another TEM (Tecnai F20, FEI). The compositional depth profile was obtained using Auger electron spectroscopy (AES, PHI660). The morphology and roughness of film surface are investigated using AFM. For the measurements of dielectric properties, silver top electrodes with 150 μm in diameter were deposited on CCTO thin films by DC sputtering using a shadow mask. The relative dielectric constant, ϵ_r and $\tan\delta$ of the specimens were measured by an impedance/gain-phase analyzer as a function of the frequency between 100 Hz to 1 MHz (HP 4194a). In order to reveal the electrical transport of CCTO films under DC bias conditions, current-voltage (*I-V*) measurement were performed by using a LCR source meter (KEITHLEY-4200 SCS).

6.3. Results and discussion

6.3.1 Polycrystalline CCTO films on platinized Si substrates

6.3.1.1 Single-layered films

Fig. 6.1 (a)-(e) shows FESEM images of CCTO thin films which were deposited at various substrate temperatures ranging from 700 to 800°C and followed by slow cooling at high oxygen pressure, of which cooling conditions are typically adopted during cooling stage of oxide thin film

fabrication [16, 19, 27]. Compared to the CCTO films deposited at 700 and 725°C, showing no segregation on film surface as shown in Fig. 6.1(a) and (b), respectively, the film deposited at 750°C exhibits small amount of nanoparticles segregated at grain boundaries (Fig. 6.1(c)). As the deposition temperature was increased from 750 to 800°C, the amount of segregated particles was severely increased as shown in Fig. 6.1(d) and (e). In order to indentify the nanoparticles segregated at grain boundaries, EPMA mapping analysis was performed as shown in Fig. 6.2 (a) and (b). The surface segregations exactly coincide with the areas with high copper counts in EPMA mapping, suggesting these segregated nanoparticles are related to copper compounds. In fact, copper-oxide segregation at the grain boundaries has been frequently observed in the polycrystalline CCTO ceramics. When sintered CCTO sample was thermally etched at elevated temperature of 900°C in air, grain boundary was grooved and copper was diffused out of the grain boundary, resulting in copper-oxide segregation [39]. Fang *et al.*[11] also observed that copper oxides were mainly located at grain boundaries of CCTO samples. In the case of CCTO thin films in this study, the cooling condition of slow cooling rate at high oxygen pressure is thought to have an effect similar to thermal etching, so that large amount of copper-oxides was diffused out from the grain boundaries as shown in Fig. 6.1(c)-(e).

The messy surface of CCTO thin film due to large amount of segregated copper oxide is critical drawback in practical application, i.e., in high-*k* dielectrics. Referring to previous reports [40-41], thermal stability of perovskite materials against chemical decomposition is very sensitive to ambient oxygen conditions. Therefore, to obtain smooth CCTO film surface

without copper oxide segregation, cooling parameters such as oxygen pressure and cooling rate were carefully controlled. Thus, instead of the cooling condition of slow cooling rate at high oxygen pressure, we adopted fast cooling rate at low oxygen pressure. Here, fast cooling means that sample was cooled from deposition temperature to room temperature by turning off the heater locating under the substrate. As a result, all the CCTO thin films show no surface segregation as shown in Fig. 6.1(f)-(j), irrespective of deposition temperature. The EPMA mapping analysis shown in Fig 6.2 (c) and (d) also shows no trace of copper-oxide segregation. However, some out-grown large particles (indicated by white arrows in Fig. 6.1(h)-(j)), which were frequently observed in PLD-grown films [42-43], appear on film surface from the deposition temperature of 750°C to 800°C. When the oxygen pressure during cooling stage was further decreased to $\sim 10^{-4}$ Pa, segregation-free smooth surface was also obtained (not shown). These results imply that copper-oxide segregation preferentially occurs at high oxygen pressure and temperature.

Fig 6.3 shows the selected XRD patterns of CCTO films prepared by two different cooling conditions. We could observe diffraction peak of copper oxide only in the sample cooled slowly at high oxygen pressure, which was absent in those cooled fast at low oxygen pressure in Fig. 6.3(a). Therefore, this peak is considered to originate from the segregated copper oxides on the film surface. Additionally, impurity phase of rutile-TiO₂ was also observed in the high-oxygen-cooled sample.

From the XRD patterns of the CCTO thin films cooled fast at low oxygen pressure (Fig, 6.3(b)-(d)), an interesting features are observed. Those are

appearance of preferred orientation and change of its direction with increasing substrate temperature. The intensity of (220) diffraction peak was increased compared to those of other peaks as the substrate temperature was increased from 700°C to 750°C. Similar preferential orientation was also observed in previous results of polycrystalline CCTO films [18-19, 28]. However, as the substrate temperature is increased over 750°C, different preferred orientation is observed, i.e., (400)-preferred growths become dominant as shown in Fig. 6.3(b). In addition, intermetallic compounds of PtCu₃ and PtTiO₂ are observable in CCTO film deposited at 800°C in Fig. 6.3(b). The reasons for the existence of these intermetallic compounds are represented later.

Fig. 6.4 shows the dielectric properties of the CCTO films as a function of substrate temperature and measuring frequency. Except the film fabricated at 700°C, all the films with no copper-oxide segregation showed remarkably improved dielectric constants in all measured frequency range. Especially, the extent of increment in dielectric constant was the highest at the deposition temperature of 750°C. As the extent of compositional non-stoichiometry of CCTO films due to copper-oxides segregation was increased, the chemical composition of CCTO grains could be Cu-deficient state. Therefore, the amount of stoichiometric CCTO phases in the film without copper-oxide segregation was much larger than that in the films with copper-oxide segregation, and thus the dielectric constant of the CCTO films without copper-oxide segregation as shown in Fig. 6.1 (g)-(j) was remarkably increased. In addition, the dielectric loss properties of CCTO films with smooth surface were also improved.

The reasons for the wide variety of the ϵ_r values in the copper-oxide segregation free CCTO films in Fig. 6.1(f)-(j) were investigated. Figure 6.5(a) shows X-ray diffraction (XRD) patterns of the CCTO films. The (220), (400) and (422)-reflection peaks of CCTO represent that all films are polycrystalline in JCPDS (No: 01-072-5884). Except these CCTO peaks, two other peaks are also observed at $2\theta \sim 42^\circ$ and $\sim 44^\circ$ at elevated temperatures as previously mentioned in Fig. 6.3. These peaks observed at $2\theta \sim 42^\circ$ and $\sim 44^\circ$ are PtCu₃ (111) and PtTi₃ (211), respectively, because the peak of PtCu₃ at $2\theta \sim 42^\circ$ is the strongest in JCPDS (No.00-035-1358). The PtCu₃ compound formation could be confirmed by TEM analysis, which will be described later. Figure 6.5(b) shows that, comparing with as-received substrate, the (111) diffraction peak of Pt electrode is shifted to higher diffraction angle in all films with increasing deposition temperature, implying that a severe Cu diffusion from CCTO film to Pt layer occurred at the interface to form a Pt-Cu solid solution from 700 to 750°C, and further Cu diffusion over the solubility limit of Cu in Pt at 775 and 800°C might form the PtCu₃ intermetallic compound as well. In addition, the peak observed at $2\theta \sim 44^\circ$ is coincident with the (211) main diffraction peak of PtTi₃ in JCPDS (No.00-018-0979). This peak was also observable when as-received Pt/TiO₂/SiO₂/Si substrates were *in-situ* annealed within the deposition chamber at the temperature region of 750 ~ 800°C in the oxygen pressure of 800 mTorr.

For a quantitative analysis of any preferred orientation, we estimated the relative intensity ratios of (220) main diffraction peaks of CCTO films, $\{I_{(220)} / (I_{(220)} + I_{(422)} + I_{(400)})\}$, and obtained the values of 0.63, 0.6, and 0.6 for the

films grown at 700, 725, and 750°C, respectively. Since the value of 0.6 is calculated from the JCPDS data, these results strongly support that films are composed of randomly oriented polycrystalline grains. With increasing deposition temperature above 750°C, however, the intensity of (400) diffraction peak is abruptly increased at 775°C and becomes dominant at 800°C, representing that CCTO films grow with a strong (400)-preferred orientation. In accordance with this observation, estimated relative intensity ratios of (400)-orientation, $\{I_{(400)} / (I_{(220)} + I_{(422)} + I_{(400)})\}$ increase from 0.21 at 750°C to 0.46 and 0.78 at 775 and 800°C, respectively, while the value of 0.16 is estimated from JCPDS. These results are completely different from those in previous reports [7, 18] since (422)-preferential orientation has been observed for PLD-CCTO films on platinized Si substrates in the literature while (400)-preferential orientation is observed in our films. According to Fang *et al.*[18], (422)-preferential growth of CCTO film is favored with decreasing deposition temperature below 700°C, or oxygen pressure below 200 mTorr at 720°C, or film thickness below 480 nm at 720°C in 200 mTorr. Thus, this discrepancy must be due to the difference in the deposition temperature. The origin for (400)-preferential growth of CCTO films will be described later on the basis of TEM analysis.

Referring to the FE-SEM micrographs in our previous report [25], one can observe that films grown at 700, 725, and 750°C reveal smooth and uniform square shaped grains without any microcracks. The grain morphologies are in good agreement with those of previous report by Fang *et al.*[18]. However, as the deposition temperature is increased above 750°C, square-and round-shaped grains coexist (see Fig. 1 (i) and (j) in ref. [25]). The occurrence of

round-shaped grains on the film surface might be due to the formation of (400)-preferential orientation in Fig. 6.1(a) since these phenomena occur at the same deposition temperatures.

The cross-sectional TEM images of CCTO films are represented in Fig. 6.6. It is shown that somewhat loosely connected small columnar grains are converted into dense large grains as the deposition temperature is increased from 700 to 800°C. While the interfaces of Pt electrode toward CCTO layer in Fig. 6.6 (a) and (b) are flat, those in Fig. 6.6(c) ~ (e) are relatively rough and in addition, large amount of Pt hillocks, indicated by white circles, are also observed. Jung *et al.*[44] have reported that Pt hillock formation is accelerated for relieving the compressive stress of Pt electrode caused by Ti diffusion from the Ti adhesion layer to Pt electrode. They also report that the Pt hillocks show strong (100) electron diffraction patterns compared to that of Pt (111) electrode. Strong (400)-preferential growth of CCTO films in the XRD patterns of Fig. 6.5 (a) above 750°C may be ascribed to the formation of [100]-oriented Pt hillocks at the Pt electrode surface. Similar to the “dead layer” frequently observed at the interface between functional dielectric films and Pt electrode [45-48], it is also observed in our samples as indicated by white arrows in Fig. 6.6(c), (d) and (e). In contrast to clear selected area diffraction pattern (SADP) of CCTO grains in the upper inset of Fig. 6.6(f), the dead layer shows randomly orientated lattice fringes in the Fig. 6.6(f) and ambiguous SADP in the lower inset of Fig. 6.6(f), representing that the dead layer consists of randomly oriented grains of 30-50 nm although it is undetectable on the XRD patterns in Fig. 6.5.

Fig. 6.7 shows ϵ_r and $\tan\delta$ as functions of frequency for the CCTO film at room temperature. The CCTO film grown at 750°C shows the highest dielectric constant of 2,000 at 10 kHz, whereas other films show lower dielectric constants at 10 kHz, *i.e.* $\epsilon_r \sim 300, 1700, 1100,$ and 850 at 700°C, 725°C, 775°C and 800°C, respectively. As the deposition temperature is increased from 700 to 750°C, the dielectric constant is increased due to the presence of enlarged grains with densely packed structure in Fig. 6.6 (a), (b) and (c), of which results are in good agreement with previous results of CCTO films [18]. However, the severe dielectric constant drop is observed when the deposition temperature is increased over 750°C. Dielectric loss exhibited unpredictable behavior in their frequency-dependence. In general, large dielectric loss at the low frequency is greatly reduced in the medium frequency region, but the loss increases again at high frequencies. The dielectric loss of 0.1 or higher at low frequency is much larger than that of other dielectrics and ferroelectrics [49-50]. This may be related to their DC resistivity characteristics because the low-frequency loss is attributed to space charges and interfacial disorders. The large loss in the high frequency region between 10^5 and 10^6 kHz is due to dipolar oscillations of the materials.

For identifying the chemical reactions at the interface between CCTO films and Pt electrode, both AES and EDS analyses were performed as shown in Fig. 6.8. Compared with the small amount of Ti diffusion from the adhesive layer of TiO₂ to Pt electrode in Fig. 6.8(c), (g) and (k) indicated by white arrows, a severe Cu diffusion from CCTO films to Pt electrode is clearly observed in the Cu-mapping images by EDS analysis in Fig 6.8 (a), (e) and (i). In addition, AES analysis data in Fig 6.8 (d), (h) and (l) exhibit

that the amount of diffused Cu into Pt electrode is increased with increasing deposition temperature from 700 to 800°C. Therefore, it is obvious that the Pt (111) peak shifts to the higher diffraction angle in Fig. 6.5(b) is due to an increased diffusion of Cu into Pt. As previously mentioned, more serious Cu diffusion in Pt over the solubility limit [51] might result in the formation of PtCu₃ compound above 750°C in Fig. 6.5(b). The PtCu₃ phase mainly exists at the surface of Pt electrode as shown in Fig. 6.9(a) indicated by white circle in the region 2. In contrast to the fast fourier transformation (FFT) image of Pt (111) electrode (Pt 111, $d_{111}=2.265\text{\AA}$) in the inset of Fig. 6.9(a), the diffraction peak of PtCu₃ (PtCu₃ 111, $d_{111}=2.137\text{\AA}$) in region 2 is clearly observable in Fig. 6.9(b). However, the PtTi₃ phase in Fig. 6.5 was hardly observed with HR-TEM analysis probably because of its relatively small amount.

AES analyses in Fig. 6.8(d), (h), (l) for revealing the chemical composition of the dead layer between CCTO films and Pt electrode indicate that the atomic percentages of Ti and O are relatively increased at the dead layer region ② compared to that of other elements. In contrast to the existence of Cu-L_{2,3} spectrum of CCTO grain near the energy loss region of 940eV by the electron energy loss spectrum (EELS) analysis, no trace of Cu spectrum appeared in the dead layer as shown in Fig. 6.10(d). Therefore, the dead layer is mainly composed by the TiO₂ phase. In addition, the thickness of TiO₂-rich dead layer is increased as the Cu-diffusion is accelerated with increased deposition temperature in Fig. 6.10 (a), (b) and (c). Consequently, a serious decrease in the dielectric constants of CCTO films above 750°C in Fig. 6.7(a) is attributed to the TiO₂-rich dead layer of relatively lower

dielectric constant ($\epsilon_{r,\text{TiO}_2} \leq 100$) which is connected with CCTO films in series [24, 52]. The dead layer is known detrimental to other dielectric films on the Pt/TiO₂/SiO₂/Si substrates because it usually shows much lower dielectric constant compared with dielectric films [47]. Also, the measured dielectric constant could be related to the carrier concentration of films, which may vary with deposition temperature so that leakage current behaviors of CCTO films will be discussed in the following paragraph.

Figure 6.11 shows the *I-V* characteristics of the CCTO films measured at room temperature. The CCTO film deposited over 750°C shows relatively high leakage current compared to the CCTO films deposited at 700 and 725°C. These results show strong consistency with the low frequency dielectric loss behaviors in Fig. 6.7(b). To explain the conduction mechanism, two conventional models are addressed in this study. One is Schottky thermionic emission (SE) and the other is Poole-Frenkel (PF) conduction. These models are basically thermal excitation effects of electric charges out of defects either at interface or inside of the bulk [53]. Following is the explicit formula for SE emission

$$J_{SE} = AT^2 \exp\left[-\frac{q}{kT}\left(\phi_{BE} - \sqrt{\frac{qE}{4\pi\epsilon\epsilon_0}}\right)\right] \quad (1)$$

, where A is a constant, ϕ_{BE} is the barrier height, q is the electric charge, k is the Boltzmann's constant, E is the electric field and T is the temperature. And, ϵ is the dielectric permittivity at the optical frequency and ϵ_0 are the dielectric permittivity of vacuum. Following is the form for PE conduction

$$J_{PF} = BE \exp \left[-\frac{q}{kT} \left(\phi_{PF} - \sqrt{\frac{qE}{\pi \epsilon \epsilon_0}} \right) \right] \quad (2)$$

,where B is a constant, ϕ_{PF} is the barrier height. It is essential to measure the temperature dependence of the leakage currents but the fitted value of leakage current could give a guideline for the proper explanation of the conduction models at room temperature. From the fittings of the data, the slopes for the SE emission are between 0.0017 and 0.0030 while the gradients for the PE conduction are in the range of 0.0010 and 0.0023. It is known that dielectric constant of CCTO films at optical frequency region is 1 to 1.6, which are dependent on porosity or crystallinity of the films [54]. Dielectric constants from the SE emission are even below 1 whereas the PF conduction provides the dielectric constant from 1.6 to 2.8 except the sample grown at 700°C. The optical dielectric constant is close to the previously reported values but little higher than the previously reported values of CCTO films due to the difference of deposition temperatures and film crystallinity [27, 54]. Origin of the relatively high dielectric constant of the film at 700°C is unclear so that further investigation using other analysis tools is required. The estimated values of dielectric constant are summarized in Table 6.1. Thus, it is reasonable that PF conduction is dominant in our CCTO films, which indicates that bulk-type trapping of carriers prevail leakage currents of the films. In earlier work by Fang *et al.* [27], they also measured the leakage current of CCTO film deposited at 650°C and insisted that the leakage current mechanism was SE emission. However, all of our samples show PF conduction and the discrepancy could be attributed to the difference of

deposition temperature. In our samples, it is possible that TiO₂-rich dead layer existing at interface between CCTO films and Pt electrode could act as trap sites for blocking charge transport and as a source for varying the dielectric loss and leakage current. Similarly, the trap-related conduction behaviors in CCTO films are frequently observed in the previous studies [52, 55-56]. In addition, as shown in Fig. 6.12 (a)-(c), it is confirmed that nanocrystallized impurity phase of rutile-TiO₂ is embedded in each grain boundary of all CCTO films. EELS analysis on the oxygen stoichiometry of nanocrystallized TiO₂ revealed that the peak splitting of the Ti-L_{2,3} edge at the grain boundary was not as clear as that of the grain inside in the inset of Fig. 6.12(d) but quite similar to that of previously reported stoichiometric rutile TiO₂ [57]. Therefore, it can be suggested that the insulating TiO₂ nanoparticles at the grain boundaries also block the free carriers transport and induce the PF conduction behavior of CCTO films. Consequently, microstructure changes and compositional variations in CCTO films are responsible for the variation in their dielectric and leakage current properties.

6.3.1.2 Multi-layered CCTO films

We tried to investigate the effectiveness of CTO layer as an electrical barrier for decreasing the high $\tan\delta$ values and leakage current of polycrystalline CCTO films by fabricating multi-layered structures. As shown in Fig. 6.13 (b)-(d), three possible multi-layered structures of Pt/CTO-60nm/CCTO-500nm, Pt/CCTO-500nm/CTO-60nm, and Pt/CTO-60nm/CCTO-500nm/CTO-60nm films were successfully fabricated on

platinized-Si substrates. Compared with single-layered CCTO films, the Pt/CCTO/CCTO and Pt/CCTO/CCTO/CTO samples show the enlarged grain size in Fig. 6.13(b) and (d), respectively, while the Pt/CCTO/CTO film shows the negligible variation in grain size in Fig. 6.13(b).

The frequency dependent dielectric constant and loss properties in Fig. 6.14(a) and (b) indicate that the high $\tan\delta$ values over ~ 0.1 in the single-layered CCTO films are remarkably decreased below 0.1 in the Pt/CCTO/CCTO and Pt/CCTO/CCTO/CTO structures but the $\tan\delta$ values in the Pt/CCTO/CTO films are still high for practical application. While the $\tan\delta$ properties in the multi-layered films are remarkably improved, the ϵ_r values are much lower than that of single-layered films. Especially, the ϵ_r values in the Pt/CCTO/CCTO/CTO film show the lowest values in the measuring frequency region compared to those of other samples because the total ϵ_r values in the multi-layered films are remarkably decreased by the CTO layer showing the relatively lower ϵ_r values (~ 170 at 1 kHz) than CCTO film with the following equation

$$\frac{d_{\text{total}}}{\epsilon_{\text{total}}} = \frac{d_{\text{CCTO}}}{\epsilon_{\text{CCTO}}} + \frac{d_{\text{CTO}}}{\epsilon_{\text{CTO}}} \quad (3)$$

,where the d_{total} , d_{CCTO} , and d_{CTO} is the total thickness of multi-layered films, CCTO films, and CTO layer, respectively, and ϵ_{total} , ϵ_{CCTO} , and ϵ_{CTO} is the dielectric constant of multi-layered films, CCTO films, and CTO layer, respectively. The measured and calculated ϵ_r values in the multi-layered films at 1, 10, 100 kHz are represented in Table 6.2. As shown in Table 6.2,

the calculated ϵ_r values in all multi-layered films are quite similar with those of measured ϵ_r values. Figure 6.14(c) shows the I - V characteristics of all films measured at room temperature. Similar with the low frequency $\tan\delta$ characteristics at ~ 100 Hz in Fig. 6.14(b), the CCTO film with double-sided CTO layer shows the lowest leakage current.

Although the remarkably improved $\tan\delta$ and leakage current properties are obtainable in the CCTO film with double-sided CTO layer, the severe drop in the ϵ_r values is inappropriate for practical application so that we choose the Pt/CTO/CCTO structure and increase the thickness of CCTO films from ~ 200 nm to $\sim 1.2\mu\text{m}$. Because ϵ_r values in dielectric films are generally increased with increasing film thickness[58] and the $\tan\delta$ and ϵ_r values in the Pt/CTO/CCTO film are comparable and relatively higher than those of the Pt/CTO/CCTO/CTO film, respectively, in Fig. 6.14(a) and (b).

Figure 6.15 shows the XRD patterns of the single and multi-layered CTO/CCTO films with various thicknesses ranging from ~ 200 nm to $\sim 1.2\mu\text{m}$. The reflection peaks of (211), (220), (400) and (422) are from CCTO films and (101) and (040) are from CTO films as shown in Fig. 6.15 representing that polycrystalline films are successfully fabricated. However, unidentified impurity phases are observable also at $2\theta \sim 38^\circ$ and 64° in Fig. 6.15(a) and (c), respectively. For a quantitative analysis of any preferred orientation, we calculated the relative intensity ratios of (211) diffraction peak using the $\{I_{(211)} / (I_{(211)} + I_{(220)} + I_{(400)} + I_{(422)})\}$ relations because the (211) peaks are dominant in ~ 200 and ~ 450 nm-CCTO films in Fig. 6.15(a) and obtained the values of 0.810 and 0.819, respectively. The relative intensity ratios of (211) diffraction peak from the JCPDS data (No.75-2188) using the $\{I_{(211)} / (I_{(211)} + I_{(220)} + I_{(400)})\}$

+ $I_{(422)}$)} relations is 0.020, implying that (211)-preferred orientation is dominant in the above two single-layered CCTO films. However, with increasing the thickness of CCTO films ranging from ~800 nm to ~1.2 μm , the intensity of (211) diffraction peak is decreased and (220) peak is abruptly increased. The estimated relative intensity ratios of the (220) peak using the $\{I_{(220)} / (I_{(211)} + I_{(220)} + I_{(400)} + I_{(422)})\}$ relations in the ~800 nm and ~1.2 μm -CCTO films are 0.496 and 0.637, respectively, and the corresponding value from JCPDS data is 0.589, of which results support that CCTO films are composed of randomly oriented grains over the thickness of ~800 nm. Similar with these observations, (211)-preferred orientation is observable also in the multi-layered CTO/CCTO films with ~210 nm and ~380 nm thickness because the relative intensity ratios of the (211) diffraction peak using the $\{I_{(211)} / (I_{(211)} + I_{(220)} + I_{(400)} + I_{(422)})\}$ relations are 0.794 and 0.549 in each film. With further increasing the thickness over ~750 nm, randomly oriented grains become dominant. In contrast to the earlier study by Fang *et al.*, [27] the main peak of CTO layer, which is addressed at $2\theta \sim 33^\circ$ in JCPDS data (No.22-0153) is invisible in our multi-layered CCTO films. Instead, the second peak of (040) is observable in Fig. 6.15(c), of which discrepancy could be attributable to the deposition temperature because they deposited the CTO layers at relatively lower temperature of 650°C compared to that of our 750°C.

Meanwhile, Fig. 6.15 (b) and (d) shows the enlarged XRD patterns of Pt electrode in the single and multi-layered CCTO films, indicating that the peaks of Pt electrode are shifted to higher diffraction angle in all samples. Depending on the previous study, the Pt peak shift is surely attributable to the Cu diffusion from CCTO film to Pt layer so that Pt-Cu solid solution is

formed in all samples.[59] While the further Cu diffusion over the solubility limit of Cu in Pt electrode with increasing thickness over 800 nm in single-layered CCTO films form the PtCu₃ intermetallic compound as shown in Fig. 6.15(b), no intermetallic compound between Pt and Cu could be observable in multi-layered CTO/CCTO films irrespective of the thickness in Fig. 6.12(d). Although, the severe Cu diffusion over the solubility limit of Cu in Pt electrode could be avoidable by introducing the CTO layer, it might be insufficient for preventing the Cu diffusion into Pt electrode.

As shown in the surface morphologies of Fig. 6.16, the average grain size in both the single and multi-layered films is increased with increasing the thickness and the size is much larger than those of Fang *et al.*'s [27] samples due to the relatively higher deposition temperature of 750°C compared to that of 650°C in their study. However, micro crack is observable at the thickness of 1.2 μm in single-layered film as shown in the inset of Fig. 6.16 (d). The cross-sectional SEM images represent that loosely packed smaller grains in ~200 nm-single and multi-layered films in Fig. 6.16 (e) and (m), respectively, are converted into dense structure in Fig. 6.16 (f) and (n) and columnar structure with larger grains start to occur with further increasing the thickness up to ~1.2 μm in Fig. 6.16 (h) and (p).

Similar with our previous investigation in Fig. 4(g) of ref [59], the cross-sectional TEM images of the multi-layered film also reveal that the presence of intermetallic compound of PtTi₃ is originated from the Ti diffusion from the adhesive layer of TiO₂ to Pt electrode indicated by white arrows in Fig 6.8. In addition, a severe Cu diffusion from CCTO films to Pt electrode is clearly observable in the EDS Cu-mapping image of Fig 6.17 (b). The Cu

diffusion is identified also by AES analysis in Fig. 6.17 (c) and (d) because the atomic percent of Cu in Pt electrode is increased in all samples.

Figure 6.18 shows the frequency dependent ϵ_r and $\tan\delta$ properties of single and multi-layered CCTO films at room temperature. Both the ϵ_r values below 1 kHz in single and multi-layered films are increased from ~ 280 to $\sim 7,400$ and ~ 640 to $\sim 3,800$, respectively, with increasing CCTO thickness from ~ 200 to $\sim 1.2 \mu\text{m}$ in Fig. 6.18(a)-(d). However, except the sample with $\sim 200\text{nm}$ thickness, the ϵ_r values in multi-layered films are much lower than those of single-layered films. In general, the ϵ_r values in multi-layered dielectric films are relatively lower than those of single-layered films because the total ϵ_r values in multi-layered films are determined by the above equation (1). In our investigation, the measured ϵ_{CCTO} values below 1 kHz are ~ 170 and these values are much lower than those of single-layered CCTO films so that relatively lower ϵ_{total} values are observable in our multi-layered films. Meanwhile, the ϵ_r values in the multi-layered film with $\sim 200\text{nm}$ thickness are higher than those of ϵ_r values in the single-layered film in Fig. 6.18 (a), of which phenomenon could be apprehensible with the following reasons. According to our previous study, the TiO_2 -rich dead layer ($\epsilon_{r,\text{TiO}_2} \leq 100$) is formed at the interface between CCTO films and Pt electrode due to severe Cu diffusion over the deposition temperature of 750°C so that relatively lower ϵ_r values of CCTO films than expected values are observable in Fig. 3 of ref. [59]. In the thickness range below $\sim 400 \text{ nm}$, the formation of TiO_2 -rich dead layer could be more critical for decreasing the ϵ_r values of single-layered film compared to that of multi-layered film because the amount of Cu diffusion in multi-layered films are smaller than single-layered

films. Therefore, the ϵ_r values in single-layered film with ~ 200 nm thickness could be lower than those of multi-layered film. However, the effects of dead layer might be diminished by increasing the thickness of CCTO films over ~ 400 nm so that the ϵ_r values in all single-layered films could be higher than those of multi-layered films.

As shown in Fig. 6.18 (e)-(h), the $\tan\delta$ values below 1 kHz in all multi-layered films are remarkably lower than those of the single-layered films. Especially, the $\tan\delta$ values of 0.017, 0.018, and 0.022 at 10 kHz in the multi-layered films of ~ 210 , 380, and 750 nm, respectively, are the lowest values compared to those of previously reported CCTO films at room temperature. The values are even comparable with the lowest $\tan\delta$ values of 0.015 at 10 kHz in CCTO ceramics with the composition of $\text{Ca}_{0.8}\text{La}_{0.2}\text{Cu}_3\text{Ti}_4\text{O}_{12}$ by Feng *et al*'s study.[60] However, the $\tan\delta$ values in the multi-layered films with the thickness of $\sim 1.3 \mu\text{m}$ are significantly increased up to ~ 1 at 1 MHz in Fig. 6.18 (h).

Figure 6.19 shows the representative ϵ_r , $\tan\delta$, and calculated ϵ_r values of samples at 1, 10, and 100 kHz. The calculated ϵ_r values up to the thickness of ~ 750 nm in the multi-layered films are similar with those of the measured ϵ_r values. However, the calculated ϵ_r values in the $\sim 1.3 \mu\text{m}$ multi-layered film are fairly lower than those of the measured ϵ_r values at the same frequencies. These discrepancies might be ascribed to the presence of cracks on the film surface in Fig. 6.16 (d) so that relatively lower ϵ_r values than expected values in the single-layered film are responsible for the decreased ϵ_r values calculated by the equation (1). Fig. 6.19 (d)-(f) shows the representative $\tan\delta$ values in all samples at 1, 10, and 100 kHz, indicating that the highly

decreased $\tan\delta$ values less than ~ 0.1 in all multi-layered films maintain up to 100 kHz.

The remarkably improved $\tan\delta$ properties below 1 kHz are closely related to the DC resistivity. The I - V measurement (not shown) revealed that the leakage current in all multi-layered films was significantly reduced compared to those of single-layered films as reported by Fang *et al.*[27] For clarifying the reason of the highly decreased $\tan\delta$ values and leakage current in multi-layered films, the leakage current mechanism of single (~ 800 nm) and multi-layered (~ 750 nm) films was investigated using the two conventional models. Both the SE emission and PF conduction are thermal excitation effects of the electric charge from the interface between bulk and electrode and inside of the bulk, respectively.[53] The following equations are the explicit formula for SE emission and PF conduction

$$J_{SE} \propto \exp\left[-\frac{q}{kT}\left(\phi_{BE} - \sqrt{\frac{qE}{4\pi\epsilon\epsilon_0}}\right)\right], \quad \beta_{SE} = \frac{q}{kT} \sqrt{\frac{q}{4\pi\epsilon\epsilon_0}} \quad (4)$$

$$J_{PF} \propto E \exp\left[-\frac{q}{kT}\left(\phi_{PF} - \sqrt{\frac{qE}{\pi\epsilon\epsilon_0}}\right)\right], \quad \beta_{PF} = \frac{q}{kT} \sqrt{\frac{q}{\pi\epsilon\epsilon_0}} \quad (5)$$

,where Φ_{SE} and Φ_{PF} is the Schottky barrier height and trap energy level, respectively, q is the electric charge, k is the Boltzmann's constant, E is the electric field, T is the temperature and ϵ and ϵ_0 are the dielectric constant at the optical frequency and vacuum, respectively. The β_{SE} and β_{PF} determine the slope of $\log J_{SE}$ versus $E^{1/2}$ and $\log(J_{PF}/E)$ versus $E^{1/2}$, respectively. While the previously reported dielectric constant of CCTO films at optical frequency region is between 1 to 1.6 [54], the optical dielectric constants of

the single (~800 nm) and multi-layered (~750 nm) films calculated from the β_{SE} values are even below 0.3. However, the optical dielectric constants of the two films from β_{PF} values are between 0.76~1.77 and 1.57~1.94, respectively, and these values are quite similar with previously reported values so that PF conduction is dominant in our films. As mentioned in the previous paragraph, both the TiO₂-rich dead layer and insulating CTO layers between CCTO films and Pt electrode act as bulk-type charge trapping centers. In contrast to our observation, Fang *et al.*[27] insisted that SE emission and PF conduction were the dominant conduction mechanisms in single and multi-layered CCTO films, respectively. These discrepancies could be responsible for the different deposition temperature because they adopted relatively lower deposition temperature of 650°C compared to that of our 750°C so that TiO₂-rich dead layer formation due to the Cu diffusion could be avoidable. Fig. 6.20 shows the plot of $\log J/E$ versus $1/T$ for single (~800 nm) and multi-layered (~750 nm) film, respectively, indicating that a straight line is obtainable and the trap ionization energies of the two films calculated from the slope of $\log (J/E)$ versus $1/T$ are summarized in Table. 6.3. As shown in Table.6.3, the trap ionization energies of 0.25~0.28 eV in multi-layered film is much higher than those of 0.05~0.09 eV in single-layered film. Consequently, the decrease of ϵ_r values by interposing the low- k CTO layer between CCTO and Pt electrode is inevitable in this investigation, $\tan\delta$ and leakage current properties in multi-layered films are remarkably improved due to the increased trap ionization energy.

6.3.2 Epitaxial CCTO films on single crystal substrates

In comparison with polycrystalline CCTO films, we fabricated epitaxial CCTO films with increasing the thickness from ~100 to 700 nm on STO (001) substrates with SRO bottom electrode. The lattice constant of STO and SRO are 3.905 Å and 3.93 Å, respectively, and the lattice mismatch between two substances is below 1 %. As shown in Fig. 6.21 (a) and (b), single-layered CCTO film of ~200 nm only show the well-developed (001) habit planes and single spot, respectively, implying that single layered films show perfect *c*-axis orientation. However, the multi-layered films show the unknown impurity phase around at $2\theta \sim 38^\circ$ in Fig. 6.21 (b). At this stage, the reason for the presence of impurity phase is unclear, but it could be attributable to the severe Cu diffusion from CCTO film to SRO electrode. Further investigations for identifying the chemical composition of SRO electrode using HR-TEM are required. The frequency dependent ϵ_r and $\tan\delta$ properties in Fig. 6.22 (a) show that the ϵ_r values at 1 kHz in the single-layered films are decreased with increasing film thickness. Although the ϵ_r values in the multi-layered films are somewhat increased from ~600 to ~1,000 at 1 kHz with increasing the film thickness from ~200 to ~450 in Fig. 6.22 (a), further increase in ϵ_r values disappears and severe drop starts to occur in the ~700 nm multi-layered film. Moreover, the $\tan\delta$ values at 1 kHz in all samples are remarkably higher than those of polycrystalline films in Fig. 6.18 (e)-(h). For clarifying the reasons of the deteriorated ϵ_r and $\tan\delta$ properties in the epitaxial CCTO films, we investigated the surface morphology and roughness using FESEM and AFM, respectively, in Fig.

6.23. With increasing the thickness of single-layered films from ~200 to ~700 nm, the root mean square values are increased from 2.509 to 8.892 nm in Fig. 6.23 (e)-(h) and large amount of hillocks is observable on film surface in Fig. 6.23.(a)-(d). These hillocks could be critical draw back for inducing short-circuit leakage current and the hillock formation is attributable to the large discrepancy in lattice parameter between SRO ($a=3.93 \text{ \AA}$) and CCTO ($a=3.69 \text{ \AA}$) films. Further investigations for identifying the existence chemical reactions between SRO and CCTO films are required using HR-TEM.

6.4 Summary

We have fabricated CCTO thin films on platinized Si substrates at various deposition temperatures. After deposition, the films were cooled with two different conditions: slow cooling ($3^{\circ}\text{C}/\text{min}$) at high oxygen pressure of 66 kPa and fast cooling ($\sim 20^{\circ}\text{C}/\text{min}$) at low oxygen pressure of 100 Pa. When the CCTO films were cooled slowly at high oxygen pressure from the deposition temperature above 750°C , severe copper-oxide segregation was observed on the film surface. However, when the CCTO films were cooled fast at low oxygen pressure, it disappeared irrespective of deposition temperature. These results imply that copper-oxide segregation is strongly related to high deposition temperature and oxygen pressure during cooling stage. The dielectric properties of the CCTO films were also affected by cooling condition. The fast cooled CCTO films with no copper-oxide segregation showed higher dielectric constant than the slowly cooled films with copper-oxide segregation, except the case of 700°C , implying that copper-oxide segregation has a detrimental effect on the dielectric property. In other words, the increment in the compositional inhomogeneity of CCTO films due to severe copper-oxide segregation degraded dielectric properties.

In addition, we carefully investigated the effect of deposition temperatures on the dielectric and leakage current properties of single-layered polycrystalline CCTO films. While the dielectric constant, ϵ_r is greatly increased from ~ 300 to ~ 2000 at 10 kHz with increasing the deposition temperature from 700 to 750°C , it is seriously decreased above 750°C and thus led to ~ 900 at 800°C . The improvement in the ϵ_r value up to 750°C is

most probably due to the CCTO microstructure change from smaller columnar grains to dense larger equiaxed grains. The relatively low dielectric loss of CCTO films deposited at 700 and 725°C including smooth surface of Pt layer at low frequency region implies that electrical conductivity under AC-field can be strongly affected by the inter-diffusion at the interfaces between CCTO films and Pt electrode. Large degradation in the ϵ_r value above 750°C is attributable to the TiO₂-rich dead layer formed at the interface between the CCTO layer and Pt electrode by a severe Cu diffusion from CCTO to Pt electrode. Meanwhile, the Pt hillocks grown at [100]-direction due to the Ti diffusion from the adhesive layer of TiO₂ to Pt electrode induce strong (400)-preferred orientation of CCTO films from 750 to 800°C. The leakage current behaviors of CCTO films are in good agreement with PF conduction mechanism, where both the TiO₂-rich dead layer at the interface and rutile TiO₂ nanocrystalline particles segregated at CCTO grain boundaries are considered to play a role of charge trapping centers for blocking current flow through CCTO films.

The high $\tan\delta$ value over ~0.1 at 1 kHz in the single-layered CCTO film was remarkably decreased to ~0.05 and ~0.04 in the multi-layered films of Pt/CTO/CCTO and Pt/CTO/CCTO/CTO, respectively. Furthermore, all the multi-layered films showed much lower leakage current compared to that of single-layered film. However, severe drop in ϵ_r values were observable in the multi-layered films so that the ϵ_r value of ~750, ~1,150, and ~1,020 at 1 kHz were obtainable in the Pt/CTO/CCTO/CTO, Pt/CTO/CCTO, and Pt/CCTO/CTO films, respectively, and these values were relatively lower than that of ~2,000 in the single-layered film. With increasing the CCTO

thickness, the ϵ_r values at 1 kHz in both the single and multi-layered films were also increased from ~ 280 to $\sim 7,400$ and from ~ 640 to $\sim 3,800$, respectively. The $\tan\delta$ values of ~ 0.05 in the Pt/CTO/CCTO film were almost unaltered within the measuring frequency region between 10^2 to 10^6 Hz but the values were abruptly increased to ~ 1 at ~ 100 kHz with further increasing the thickness up to $\sim 1.2 \mu\text{m}$. The leakage current in the multi-layered films was much lower than those of single-layered film since the trap ionization energies of the multi-layered films were relatively higher than that of single-layered film. We fabricated single and multi-layered epitaxial CCTO films with CTO buffer layer and investigated the dielectric properties by increasing the CCTO thickness from ~ 100 to 700 nm on STO (001) substrates with SRO bottom electrode. All samples showed perfect c -axis orientation but unidentified impurity phase was observable in the multi-layered films. The ϵ_r values in all samples were not increased with increasing film thickness and no remarkable decrease in $\tan\delta$ values was observable in the multi-layered films. These results were attributable to the presence of large amount of pin holes on the film surface due to the large discrepancy in lattice parameter between SRO and CCTO films.

References

- [1] M. A. Subramanian *et al.*, *J. Solid. State. Chem.*, 151, 323 (2000)
- [2] S. Y. Chung *et al.*, *Nat. Mater.*, 3, 774 (2004)
- [3] D. C. Sinclair *et al.*, *Appl. Phys. Lett.*, 80, 2153 (2002)
- [4] T. B. Adams *et al.*, *Adv. Mater.*, 14, 1321 (2002)
- [5] Y. H. Lin *et al.*, *J. Appl. Phys.*, 103, 074111 (2008)
- [6] T. B. Adams *et al.*, *J. Am. Ceram. Soc.*, 89, 3129 (2006)
- [7] L. Fang *et al.*, *Appl. Phys. A.*, 80, 1763 (2005)
- [8] Y. W. Li *et al.*, *Appl. Phys. Lett.*, 92, 042901 (2008)
- [9] C. C. Homes *et al.*, *Science.*, 293, 673 (2001)
- [10] J. Li *et al.*, *Solid. State. Commun.*, 135, 260 (2005)
- [11] T. T. Fang *et al.*, *Chem. Mater.*, 17, 5167 (2005)
- [12] M. A. Ramirez *et al.*, *J. Phys. D: Appl. Phys.*, 42, 185503 (2009)
- [13] S. Krohns *et al.*, *Appl. Phys. Lett.*, 91, 022910 (2007)
- [14] M. H. Whangbo *et al.*, *Chem. Mater.*, 18, 3257 (2009)
- [15] M. C. Ferrarelli *et al.*, *J. Mater. Chem.*, 19, 5916 (2009)
- [16] W. Si *et al.*, *Appl. Phys. Lett.*, 81, 2056 (2002)
- [17] Y. Lin *et al.*, *Appl. Phys. Lett.*, 81, 631 (2002)
- [18] L. Fang *et al.*, *Thin Solid Films.*, 440, 60 (2003)
- [19] L. Fang *et al.*, *J. Appl. Phys.*, 95, 6483 (2004)
- [20] G. Deng *et al.*, *Appl. Phys. Lett.*, 91, 202903 (2007)
- [21] Y. L. Zhao *et al.*, *Thin Solid Films.*, 445, 7 (2003)
- [22] G. Deng *et al.*, *Appl. Phys. Lett.*, 92, 172909 (2008)
- [23] M. Mitsugi *et al.*, *Appl. Phys. Lett.*, 90, 242904 (2007)
- [24] L. Fang *et al.*, *Solid. State. Commun.*, 137, 381 (2006)
- [25] S. Y. Lee *et al.*, *Thin Solid Films.*, 518, 5711 (2010)
- [26] G. Deng *et al.*, *J. Appl. Phys.*, 105, 084106 (2009)
- [27] L. Fang *et al.*, *J. Appl. Phys.*, 100, 104101 (2006)
- [28] L. Fang *et al.*, *J. Cryst. Growth.*, 310, 3470 (2008)

- [29] D. Maurya *et al.*, *Bull. Mater. Sci.*, 31, 55 (2008)
- [30] R. Jimenez *et al.*, *J. Eur. Ceram. Soc.*, 27, 3829 (2007)
- [31] Y. W. Li *et al.*, *J. Cryst. Growth.*, 310, 378 (2008)
- [32] L. C. Chang *et al.*, *Thin Solid Films.*, 516, 454 (2007)
- [33] D. P. Singh *et al.*, *Mat. Sci. Eng. B.*, 157, 58 (2009)
- [34] E. Joanni *et al.*, *Appl. Phys. Lett.*, 92, 132110 (2008)
- [35] S. Y. Lin *et al.*, *J. Electron. Mater.*, 38, 453 (2009)
- [36] B. S. Prakash *et al.*, *Thin Solid Films.*, 516, 2874 (2008)
- [37] R. L. Nigro *et al.*, *Thin Solid Films.*, 515, 6470 (2007)
- [38] R. L. Nigro *et al.*, *Surf. Coat. Tech.*, 201, 9243 (2007)
- [39] S. Y. Lee *et al.*, *Electron. Mater. Lett.*, 3, 23 (2007)
- [40] J. Lin *et al.*, *Appl. Phys. Lett.*, 76, 17 (2000)
- [41] H. N. Lee *et al.*, *Appl. Phys. Lett.*, 84, 20 (2004)
- [42] E. V. Pechen *et al.*, *Appl. Phys. Lett.*, 66, 17 (1995)
- [43] K. Kinoshita *et al.*, *Jpn. J. Appl. Phys.*, 33, 417 (1994)
- [44] W. W. Jung *et al.*, *J. Electroceram.*, 13, 55 (2004)
- [45] H. Chen *et al.*, *Appl. Surf. Sci.*, 254, 3175 (2008)
- [46] J. Wang *et al.*, *J. Mater. Sci: Mater Electron.*, 20, 1208 (2009)
- [47] J. X. Liao *et al.*, *Appl. Surf. Sci.*, 252, 7407 (2006)
- [48] C. Zhao *et al.*, *J. Phys. D: Appl. Phys.*, 42, 185412 (2009)
- [49] M. Abazari *et al.*, *J. Appl. Phys.*, 103, 104106 (2008)
- [50] P. Gonon *et al.*, *J. Appl. Phys.*, 101, 073901 (2007)
- [51] T. B. Massalski *et al.*, *Binary Alloy Phase Diagrams Second Edition*, ed. (APDIC, 1986), p.1461
- [52] L. Fang *et al.*, *J. Phys. D: Appl. Phys.*, 38, 4236 (2005)
- [53] A. Vorobiev *et al.*, *J. Appl. Phys.*, 96, 4642 (2004)
- [54] R. L. Nigro *et al.*, *J. Am. Chem. Soc.*, 127, 13772 (2005)
- [55] Y. W. Li *et al.*, *Phys. Lett. A.*, 373, 2389 (2009)
- [56] B. Vodungbo *et al.*, *J. Phys. :Condens. Matter.*, 19, 116205 (2007)
- [57] C. Mitterbauer *et al.*, *Microsc Microanal.*, 9, 834 (2003)

- [58] C. S. Hwang *et al.*, *J. Appl. Phys.*, 92, 432 (2002)
- [59] S. Y. Lee *et al.*, *J. Mater. Res.*, 26, 2543 (2011)
- [60] L. Feng *et al.*, *Phys. Stat. Sol.*, (a), 203, R22 (2006)

Table 6.1 Calculated values of optical dielectric constant of the CCTO films based on SE and PF conduction

Deposition Temp (°C)	SE slope	ϵ_{SE}	PF slope	ϵ_{PF}	ϵ in ref. 49
800	0.0030	0.24	0.0023	1.65	1 ~ 1.6
775	0.0028	0.27	0.0021	1.96	1 ~ 1.6
750	0.0027	0.30	0.0020	2.13	1 ~ 1.6
725	0.0026	0.32	0.0017	2.84	1 ~ 1.6
700	0.0017	0.74	0.0010	8.43	1 ~ 1.6

Table 6.2 Measured and calculated dielectric constant of single and multi-layered polycrystalline CCTO films at 1, 10, and 100 kHz

Structures	Measured ϵ_r values (at 1 kHz)	Calculated ϵ_r values (at 1 kHz)
CCTO	2,162	-
CTO/CCTO	1,138	958
CCTO/CTO	1,025	958
CTO/CCTO/CTO	710	661
Structures	Measured ϵ_r values (at 10 kHz)	Calculated ϵ_r values (at 10 kHz)
CCTO	1,711	-
CTO/CCTO	1,045	868
CCTO/CTO	904	868
CTO/CCTO/CTO	678	621
Structures	Measured ϵ_r values (at 100 kHz)	Calculated ϵ_r values (at 100 kHz)
CCTO	1,490	-
CTO/CCTO	965	813
CCTO/CTO	839	813
CTO/CCTO/CTO	658	595

Table 6.3 Calculated trap ionization energies in single (~800 nm) and multi-layered (~800 nm) polycrystalline CCTO films based on PF conduction

Samples	E-field (kV/m)	Slope	$q\phi_{PF}$ (eV)	Samples	E-field (kV/m)	Slope	$q\phi_{PF}$ (eV)
CCTO	3000	-1.16	0.09	CTO/CCTO	3000	-3.07	0.26
(800nm)	5000	-0.76	0.06	(750nm)	5000	-3.16	0.27
	6000	-0.67	0.05		7000	-3.23	0.27
	7000	-0.61	0.05		9000	-3.24	0.27
					11000	-3.15	0.27
					13000	-3.01	0.25

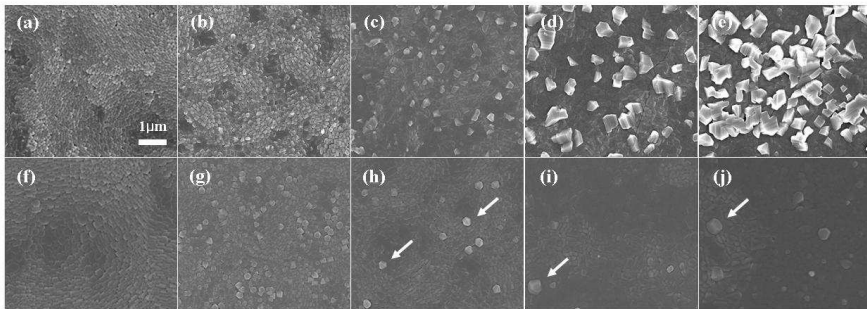


Fig. 6.1 FESEM images of CCTO thin films deposited at 700°C (a), 725°C (b), 750°C (c), 775°C (d), 800°C (e) with slow cooling rate (3°C/min) at high oxygen pressure of 66 kPa and deposited at 700°C (f), 725°C (g), 750°C (h), 775°C (i), 800°C (j) with fast cooling rate (~20°C/min) at low oxygen pressure of 100 Pa. (White arrows in Fig. 6.1 (h)-(j) indicated not segregated copper-oxides but out-grown large particles by PLD process.)

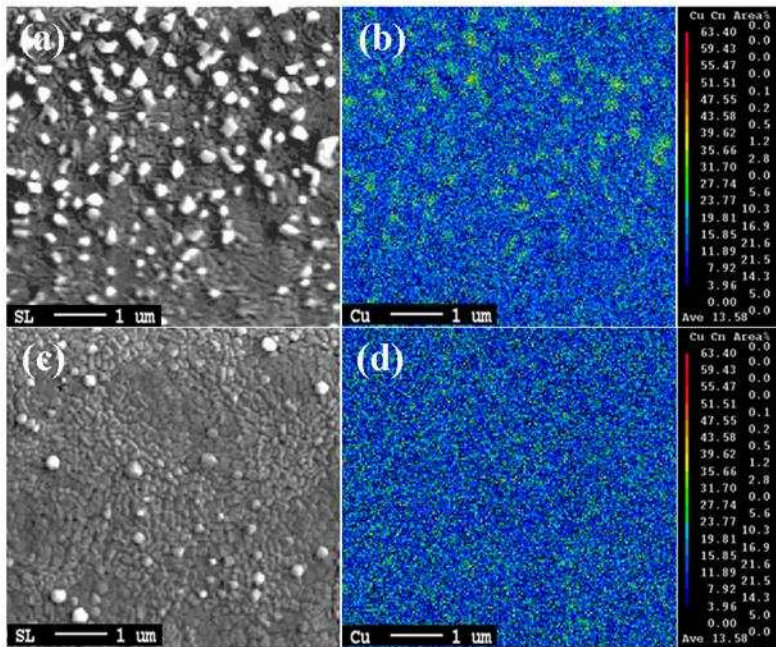


Fig. 6.2 EPMA mapping images of selected CCTO films: (a) and (b) shows secondary electron and Cu-K α edge mapping images of CCTO films, respectively, cooled down slowly (3°C/min) at high oxygen pressure of 66kPa. (c) and (d) shows secondary electron and Cu-K α edge mapping images of CCTO films, respectively, cooled down fast (~20°C/min) at lower oxygen pressure of 100Pa

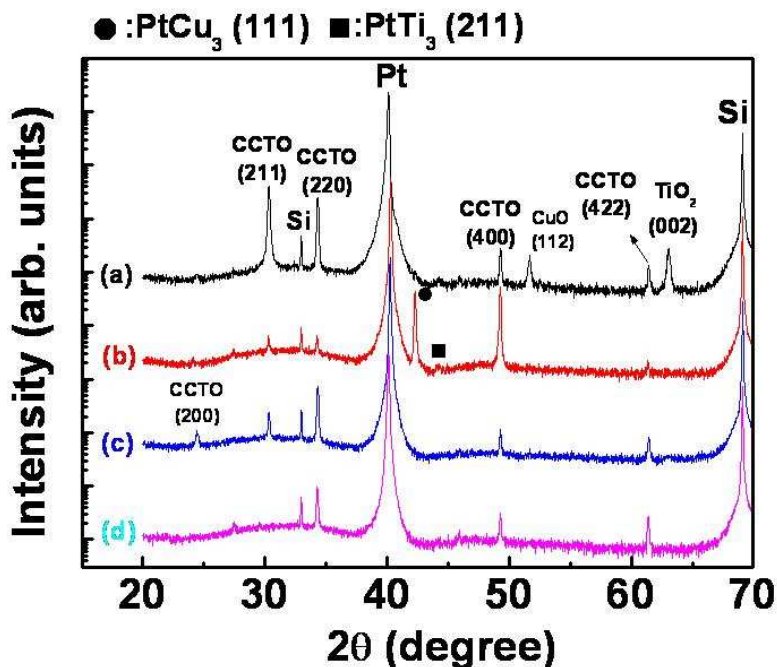


Fig. 6.3 XRD patterns of selected CCTO films: (a) CCTO film cooled down slowly at high oxygen pressure of 66 kPa after grown at 750°C. CCTO films cooled down fast at low oxygen pressure of 100 Pa after grown at (b) 800°C, (c) 750°C, and (d) 700°C

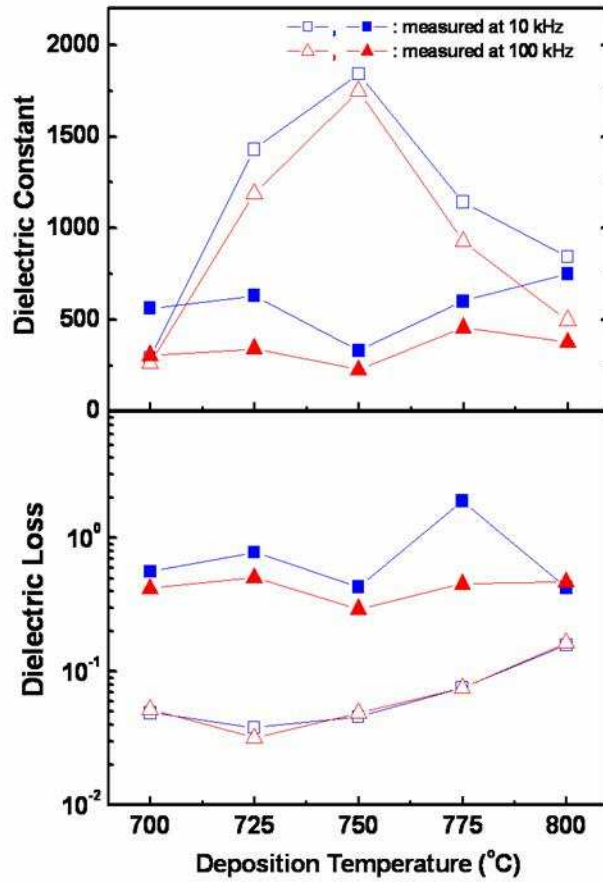


Fig. 6.4 Dielectric constant (ϵ_r) and loss ($\tan\delta$) properties of CCTO thin films as a function of deposition conditions at the frequencies of 10 and 100 kHz. (Closed symbol is denoted by the case of slow cooling at high oxygen pressure of 66 kPa and open symbol the case of fast cooling at low oxygen pressure of 100 Pa)

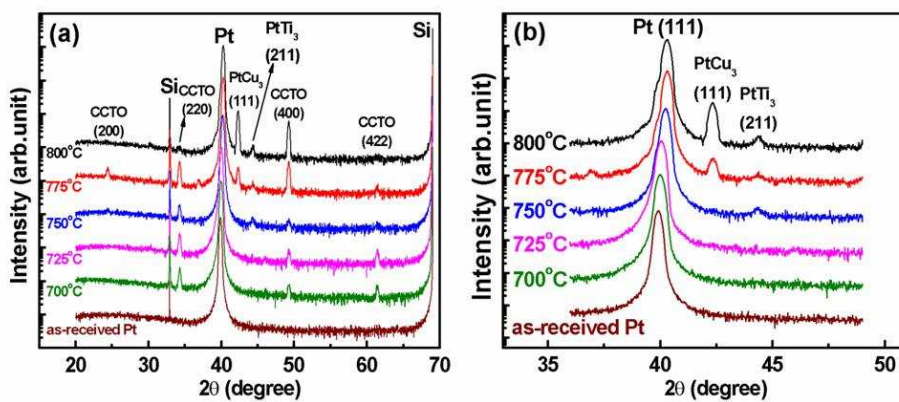


Fig. 6.5 XRD patterns of CCTO films deposited under various substrate temperatures ranging from 700°C to 800°C on Pt/TiO₂/SiO₂/Si substrates (a) and enlarged diffraction patterns of Pt electrode (b). Notice that this is semi-logarithmic plot and all data are from our previous report of ref. [25]

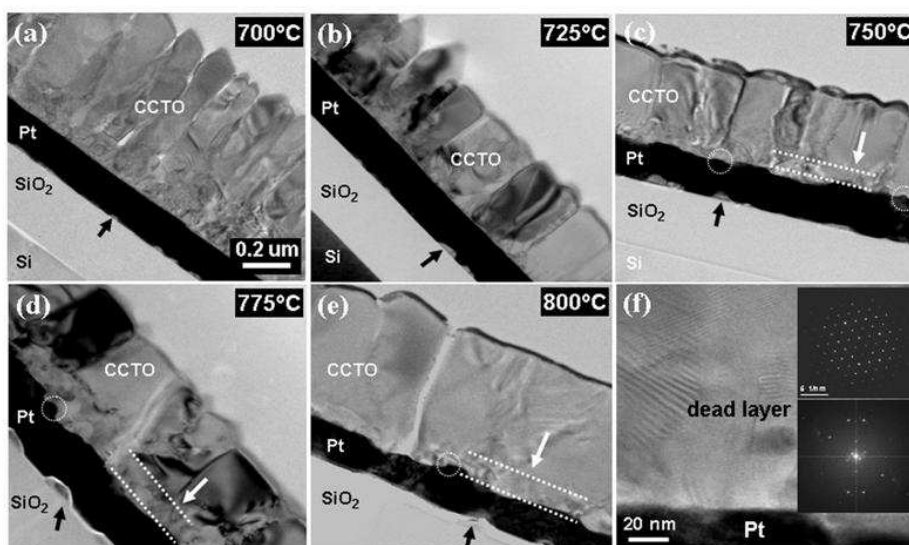


Fig. 6.6 Cross sectional TEM images of CCTO films deposited at 700°C (a), 725°C (b), 750°C (c), 775°C (d) and 800°C (e) on platinumized Si substrate, respectively. The Ti diffusion from the glue layer of TiO₂ is indicated by black arrows. The upper and lower inset of Fig. 6.2(f) shows the SADP images of CCTO grain inside and dead layer of CCTO film deposited at 775°C, respectively

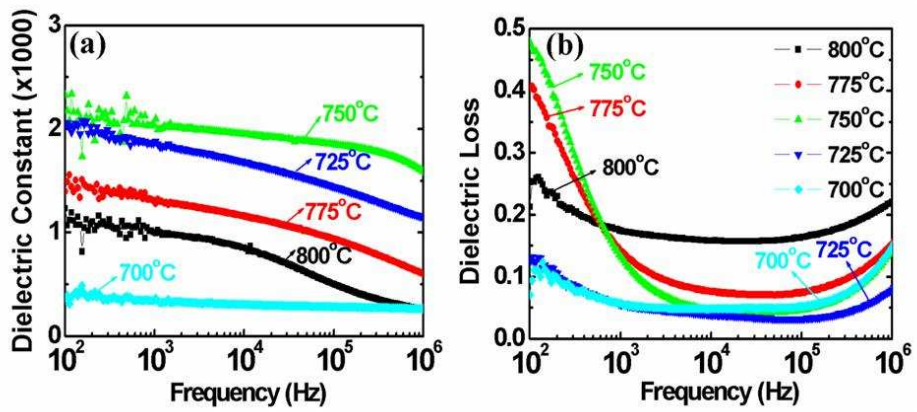


Fig. 6.7 Dielectric constant (a) and loss (b) properties of CCTO films as a function of frequency from 100 Hz to 1 MHz. Note that all the measured ϵ_r and $\tan\delta$ values are from our previous report of ref. [25]

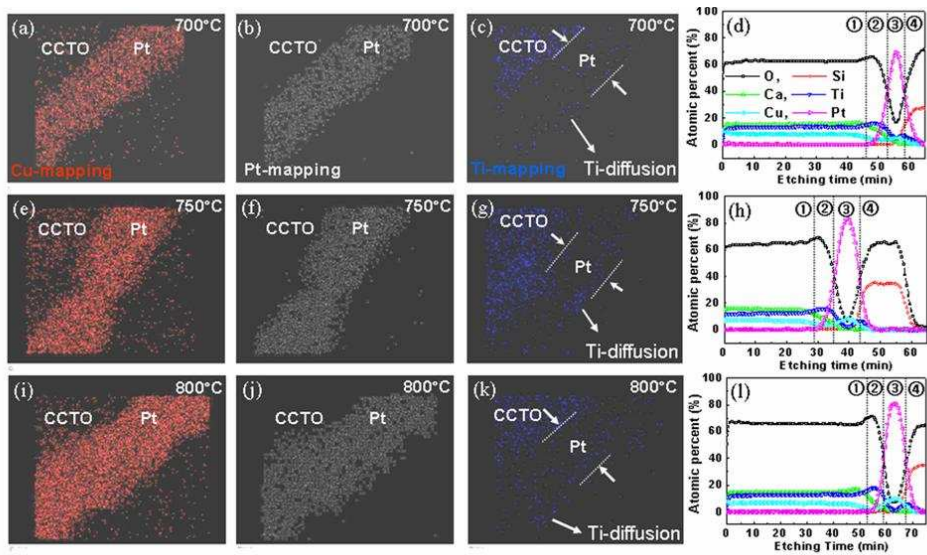


Fig. 6.8 The EDS mapping images of CCTO films deposited at 700°C, 750°C, and 800°C by Cu-mapping (a), (e), and (i), Pt-mapping (b), (f) and (j), Ti-mapping (c), (g) and (k), respectively. The compositional depth profiles by AES of CCTO films deposited at 700°C (d), 750°C (h), and 800°C (l), respectively. The each divided region of ①, ②, ③, and ④ indicates CCTO films, dead layer, Pt electrode and SiO₂, respectively

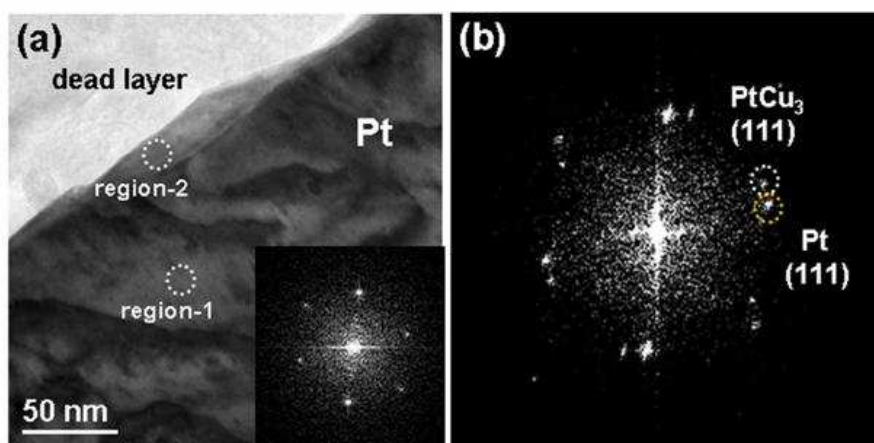


Fig. 6.9 The low magnification TEM image of Pt electrode in the CCTO deposited at 800°C (a). The inset of (a) shows the FFT image of region 1 in Pt electrode. Fig. 6.9(b) shows the FFT image of PtCu₃ (111) in region 2 with Pt (111) electrode

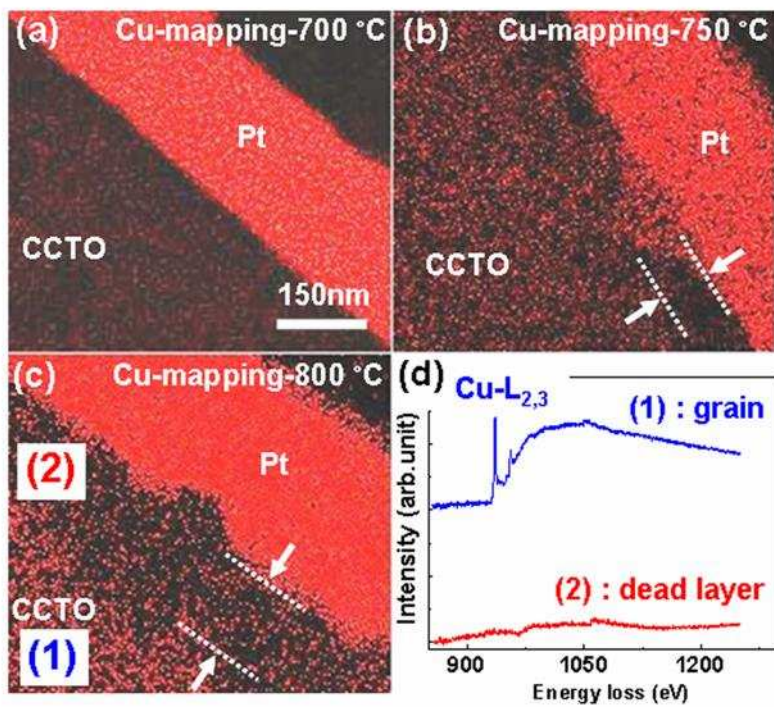


Fig. 6.10 The TEM-EDS Cu-mapping images of CCTO films deposited at 700 °C (a), 750 °C (b), 800 °C (c), and EELS spectra of CCTO grain (1) and TiO₂-rich dead layer region (2) of CCTO film deposited at 800 °C, respectively. (d)

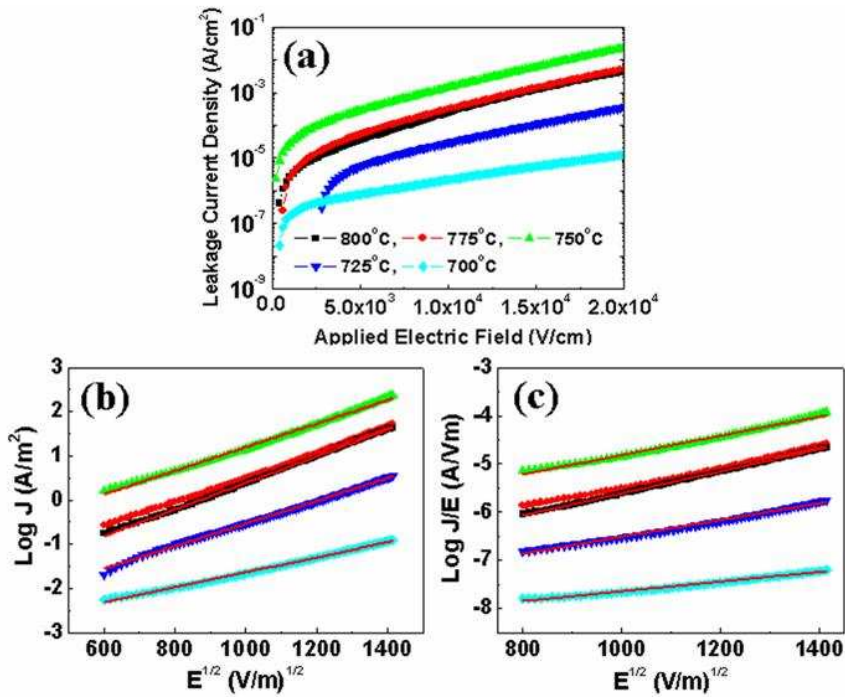


Fig. 6.11 The I - V measurement of CCTO films under DC bias condition for plots of J vs. E (a) for plots of $\log J$ vs. $E^{1/2}$ fitted by Schottky thermionic emission (b) and for plots of $\log (J/E)$ vs. $E^{1/2}$ by Poole-Frenkel conduction mechanism (c)

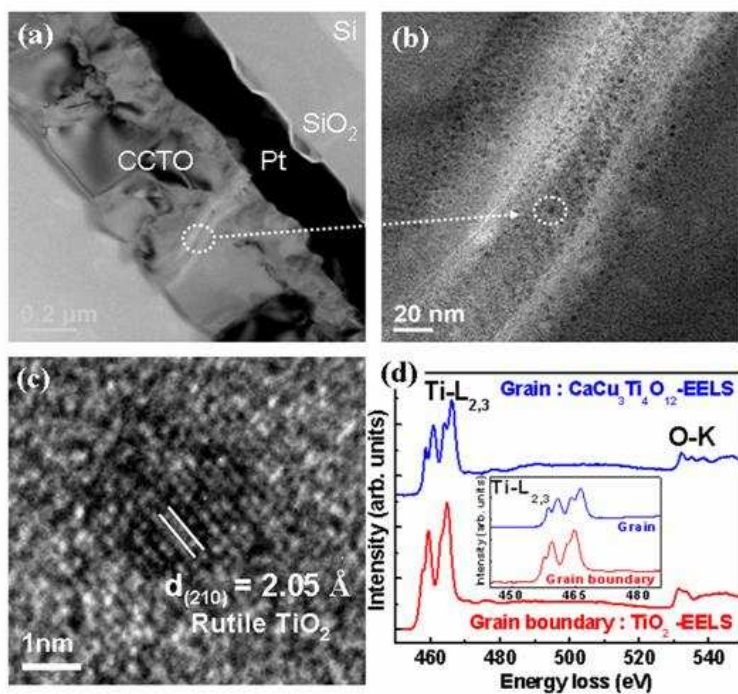


Fig. 6.12 Cross section TEM image of CCTO film deposited at 775°C on platinumized Si substrate (a), enlarged image of grain boundary (b), HR-TEM image of nanocrystallized rutile TiO₂ in grain boundary (c), and EELS spectra of grain and nanocrystallized TiO₂ in grain boundary (d). The inset of (d) shows the enlarged view of EELS spectra for Ti-L_{2,3} edge

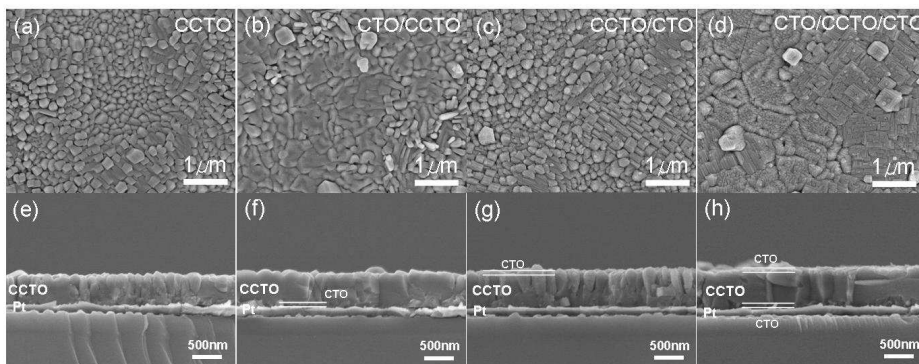


Fig. 6.13 The SEM images of single (a) and (e) and multi-layered CCTO (500nm) films of Pt/CTO/CCTO (b) and (f), Pt/CCTO/CTO (c) and (g), and Pt/CTOCCTO/CTO (d) and (h)

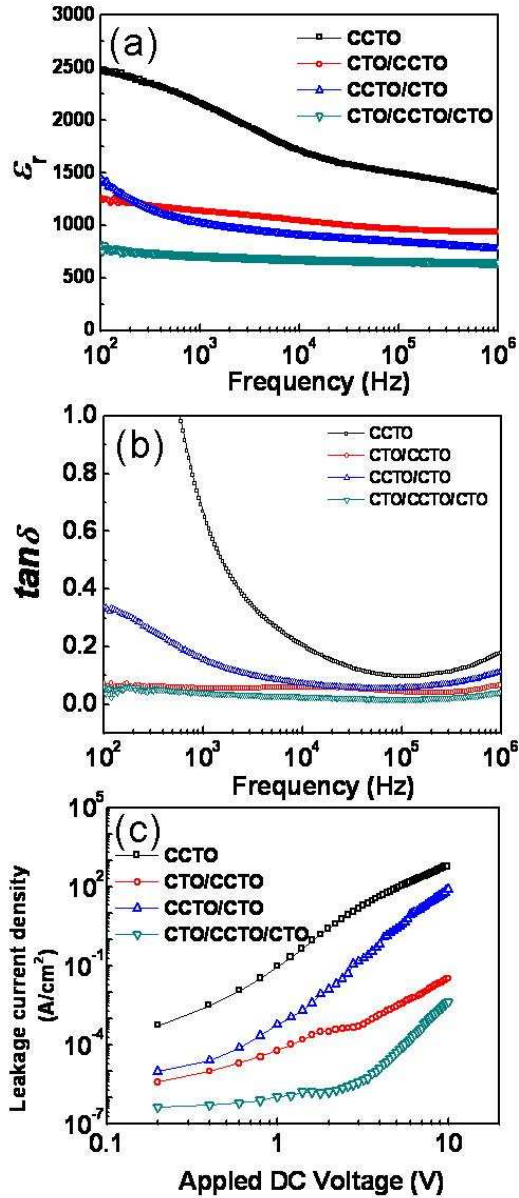


Fig. 6.14 Frequency-dependent dielectric constant (a) and loss (b) properties and I-V characteristics (c) of single and multi-layered CCTO (500nm) films

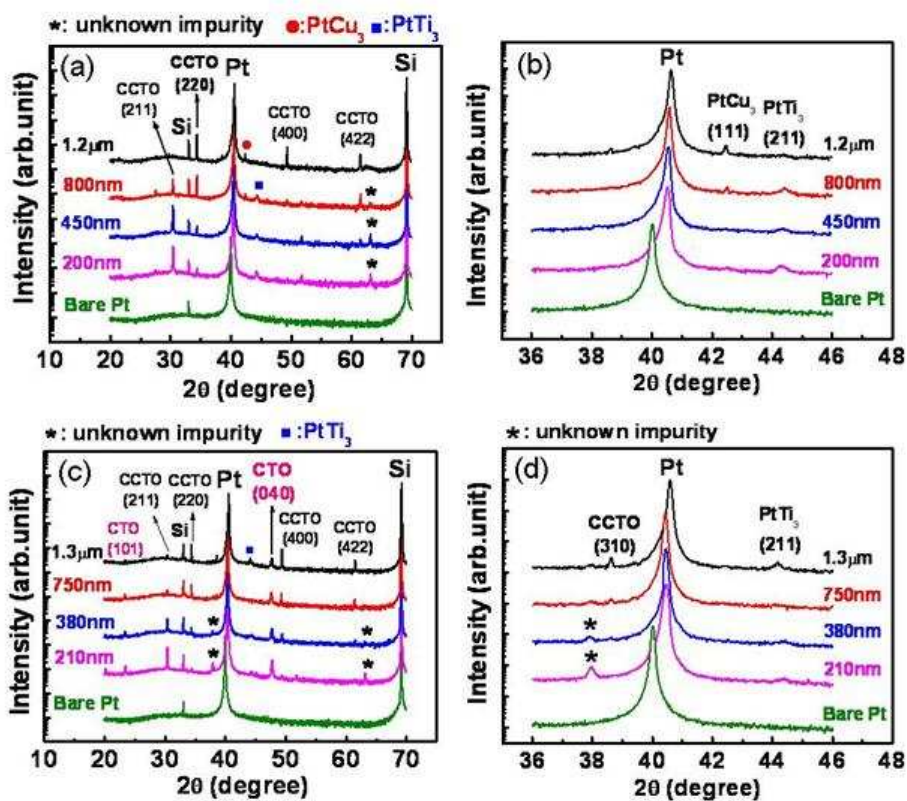


Fig. 6.15 XRD patterns of single and multi-layered CCTO films with thickness ranging from ~200 nm to ~1.2 μm deposited on Pt/TiO₂/SiO₂/Si substrates (a) and (c), respectively, and enlarged XRD patterns of single and multi-layered films (b) and (d), respectively

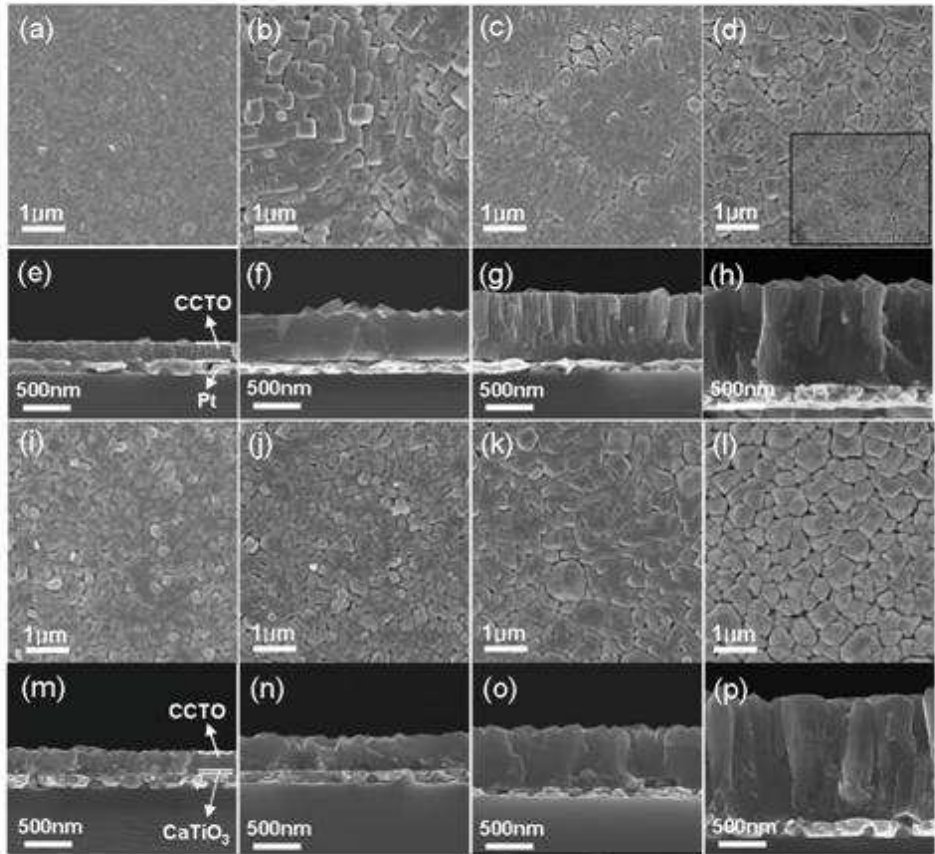


Fig. 6.16 Surface morphologies (a)-(d) and (i)-(l) and cross sectional SEM images (e)-(h) and (m)-(p) of single and multi-layered films, respectively

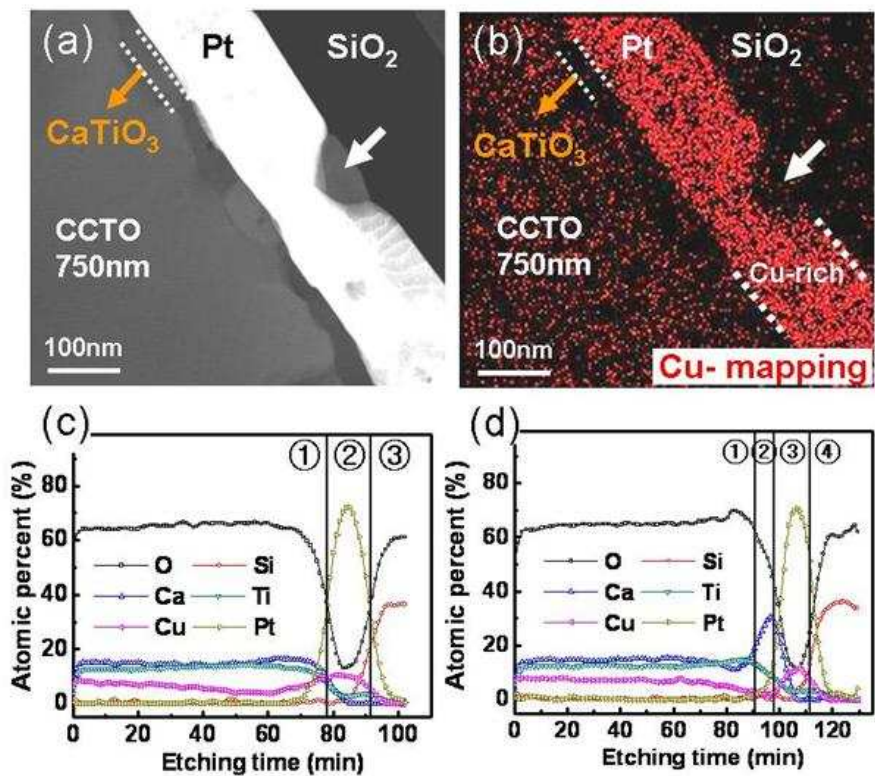


Fig. 6.17 Cross sectional TEM image (a) and EDS Cu-mapping image (b) of ~750 nm multi-layered film. The compositional depth profiles of ~800 nm single-layered films (c) and ~750 nm multi-layered film (d) by AES analysis

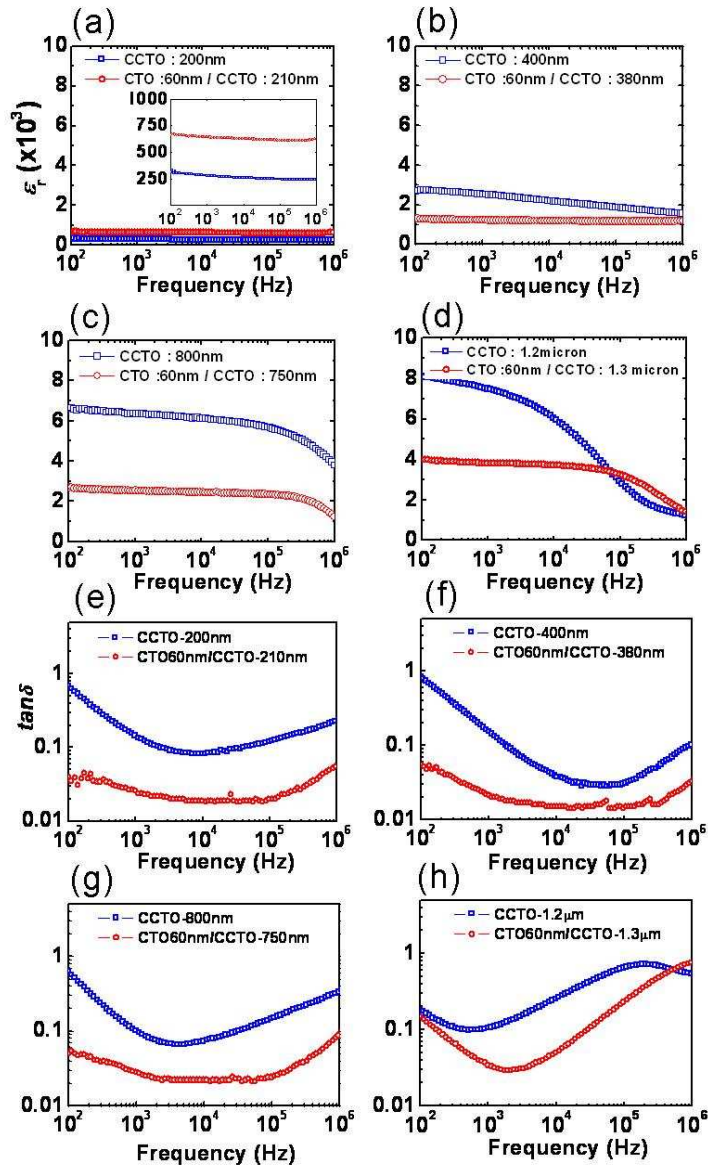


Fig. 6.18 Dielectric constant of single and multi-layered films (a)-(d) and loss (e)-(h) properties of single and multi-layered films as a function of frequency from 100 Hz to 1 MHz

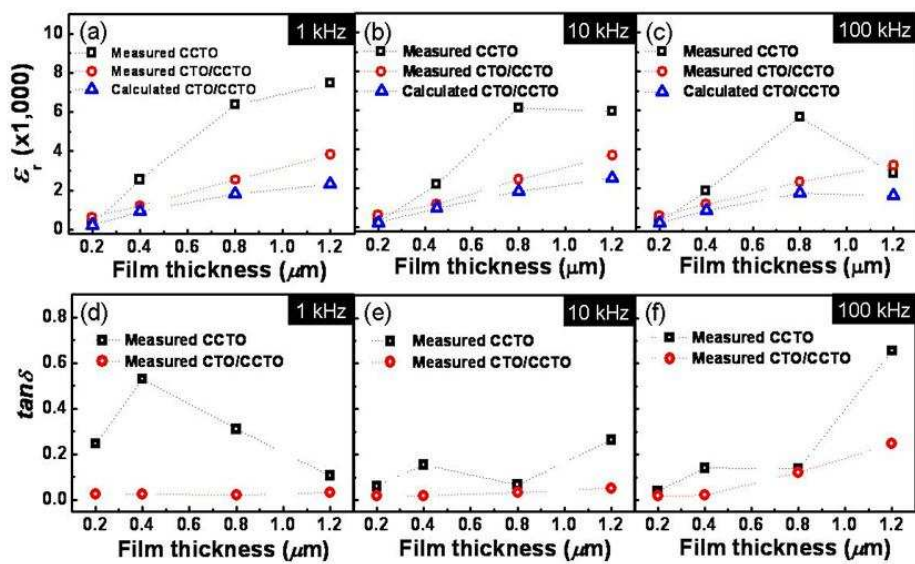


Fig. 6.19 The representative measured and calculated ϵ_r (a)-(c) and $\tan\delta$ (d)-(f) values of single and multi-layered films at 1, 10, and 100 kHz

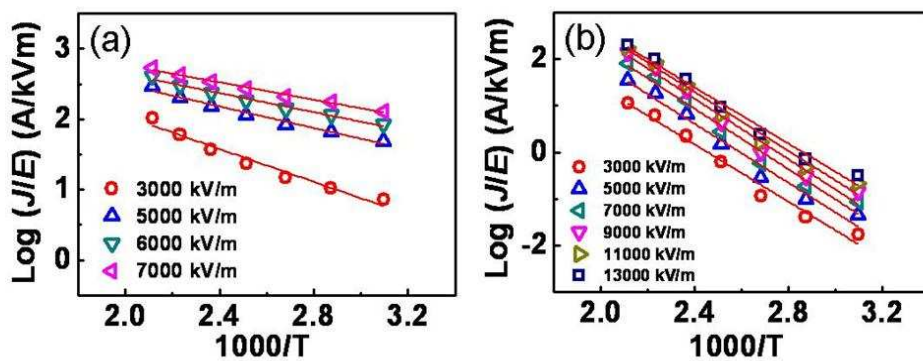


Fig. 6.20 The temperature dependent I - V measurement for plots of $\log J$ vs. $1000/T$ in ~800 nm single (a) and ~750 nm multi-layered film (b) fitted by Poole-Frenkel conduction mechanism

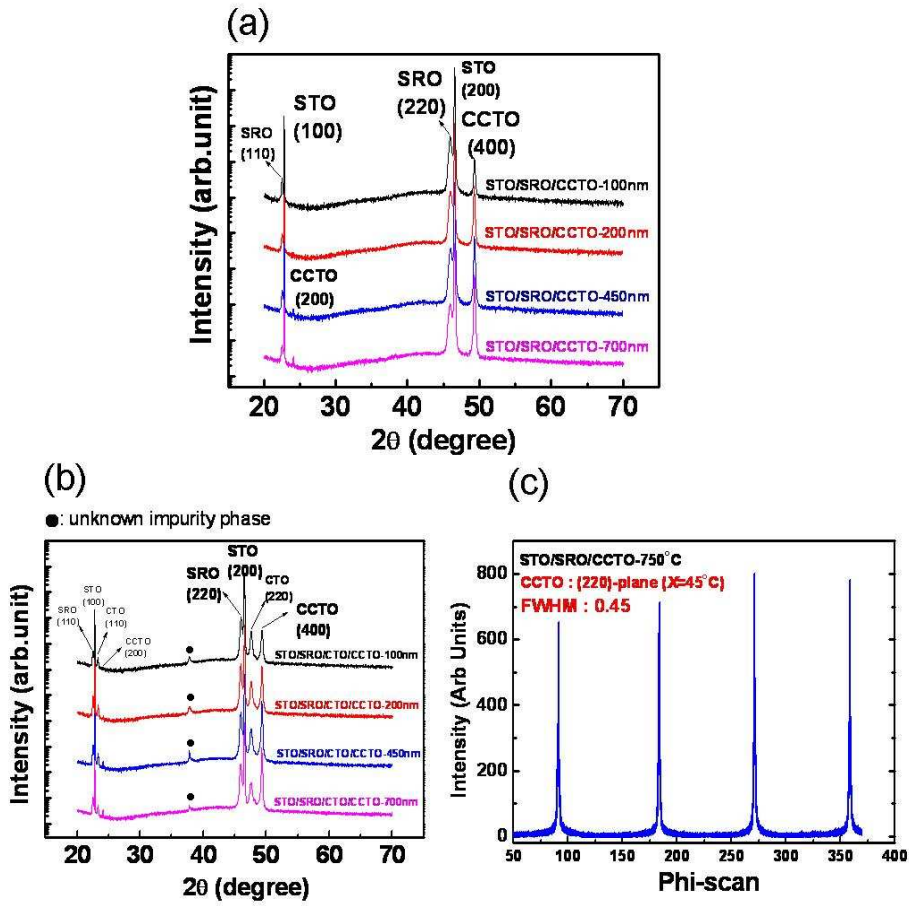


Fig. 6.21 XRD patterns of single and multi-layered epitaxial CCTO films by θ - 2θ measurement (a)-(b), and Φ -scan (c)

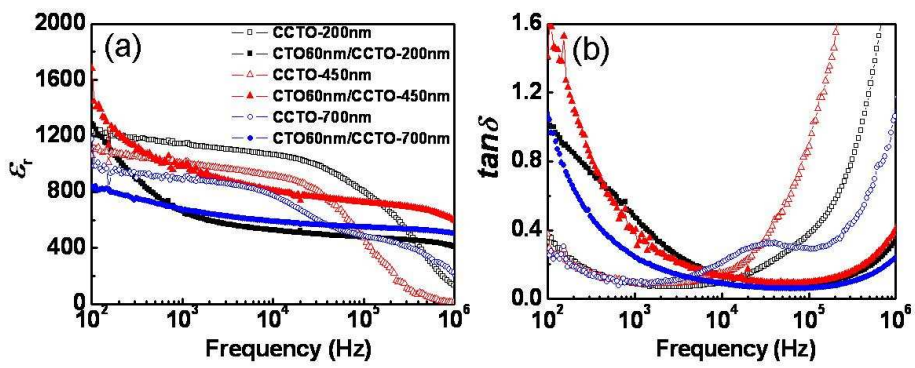


Fig. 6.22 Frequency-dependent dielectric constant (a) and loss (b) properties of single and multi-layered epitaxial CCTO films on STO single crystal substrates

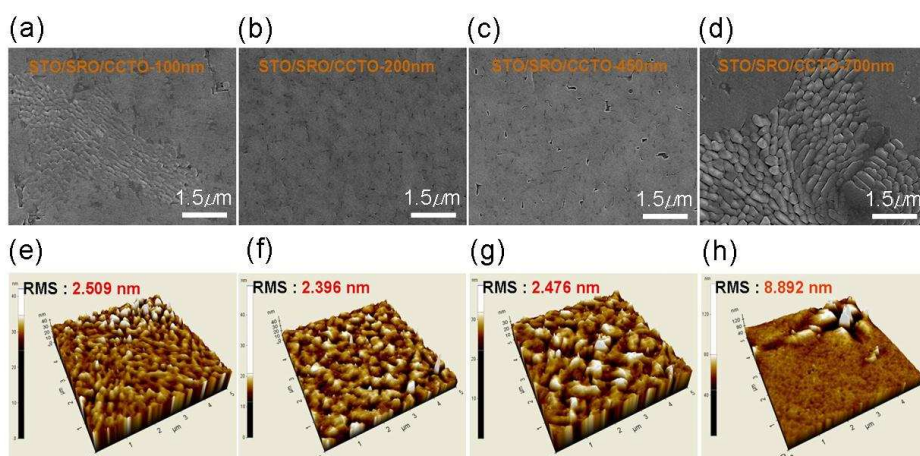


Fig. 6.23 Surface morphologies by SEM (a)-(d) and AFM images (e)-(h) of single-layered epitaxial CCTO films

Chapter 7. Summary

Although the CDR in CCTO ceramics has drawn a great attention of researchers, the physical origins of high- k in CCTO ceramics and single crystals have been unclarified yet. In addition, a high $\tan\delta$ and a large leakage current with a low breakdown voltage in CCTO are still critical drawbacks for practical application in the capacitor industry. Thus, in this these, we tried to clarify the mechanisms of high- k in CCTO bulks. Then, we systemically investigated the dielectric properties $C_{1-x}S_x\text{CTO}$ ($0 \leq x \leq 1$) ceramics. We also investigated the subsolidus phase diagrams of the SrO-CuO-TiO₂ and CaO-CuO-TiO₂ ternary systems at 950°C in air. Finally, we fabricated polycrystalline and epitaxial CCTO films by PLD for practical application. In order to decrease the high $\tan\delta$ and leakage current of single-layered CCTO films, we fabricated multi-layered CCTO films with additional CTO layer.

First, the ϵ_r values at 1 kHz in CCTO ceramics showed strong dependence on the sintering conditions and microstructures. The values were increased from ~3,000 to ~170,000 with increasing the sintering temperatures from 980 to 1000°C for 12 h, which was accompanied by an abnormal grain growth. With further increasing the sintering temperature up to 1080°C, the ϵ_r value at 1 kHz was decreased to ~69,000 with relatively smaller grain size of 150 μm . While no abnormal grain growth occurred in the CCTO ceramics sintered at 980°C for the holding time to 24 h and thus their ϵ_r values showed relatively lower ϵ_r values (< 4,000 at 1 kHz), the abnormal grain growth

occurred in the samples after a certain holding time at the sintering temperature of higher than 1000°C and thus their ϵ_r values abruptly increased. The Z^* and modulus M^* spectroscopy revealed that the variation of ϵ_r values in CCTO ceramics was exactly coincide with that of C_{gb} values. Meanwhile, the ϵ_r values in CCTO single crystals showed a strong dependence on the electrodes so that ϵ_r value of $\sim 200,000$ at 1 kHz in the sample with Ag electrode was much higher than that of $\sim 30,000$ in samples with Au and InGa electrodes at the same frequency. Consequently, the CDR in CCTO ceramics and single crystals originate from the grain boundary effect with high C_{gb} values and nonohmic contact R values at the interface between sample and electrode, respectively.

Second, we systemically investigated the dielectric properties of $C_{1-x}S_x$ CTO ($0 \leq x \leq 1$) ceramics. While the ϵ_r values in both $C_{0.4}S_{0.6}$ CTO and $C_{0.6}S_{0.4}$ CTO samples were $\sim 50,000$ at 1 kHz with relatively smaller average grain size of $\sim 80 \mu\text{m}$, extremely high ϵ_r values of $\sim 120,000$ and $\sim 180,000$ at 1 kHz were observable in the CCTO and SCTO ceramics with relatively larger average grain size of ~ 160 and $\sim 250 \mu\text{m}$, respectively. The maximum $\tan\delta$ values in the $C_{0.4}S_{0.6}$ CTO and $C_{0.6}S_{0.4}$ CTO samples were much lower than those of CCTO and SCTO samples. The Z^* and M^* spectroscopy revealed that the the C_{gb} values were much higher than those of C_g values in all samples. Therefore, the CDR in $C_{1-x}S_x$ CTO ($0 \leq x \leq 1$) ceramics were surely attributable to high C_{gb} values in all samples. Although the second phases of SrTiO₃ and CuO appeared for the compositions of $x \geq 0.8$, a linear increase in the lattice parameters was observable for the full range of Sr substitution, of which results suggested that the solubility limit of Sr substituent x existed

between $x=0.6$ and $x=0.8$ in $C_{1-x}S_x$ CCTO-type solid solutions.

Third, we carefully investigated the subsolidus phase diagrams of the SrO(CaO)-CuO-TiO₂ ternary systems at 950°C in air. In the SrO-CuO-TiO₂ ternary system, the single phase composition of SCTO compound was determined to Sr_{1-x}Cu_{3+x}Ti₄O₁₂ ($x=0.036$) and the existence of Sr_{0.9639(1-y)}Cu_{3.0361(1-3y)}Ti_{4+2y}O₁₂-type solid solutions with the solubility limit of $0 \leq y \leq 0.0235$ was identified for the first time. The variation in the lattice parameters in these new type solid solutions was negligibly small. The ϵ_r values of solid solutions were over $\sim 70,000$ at 1 kHz with abnormally grown large grains. In the CaO-CuO-TiO₂ ternary system, Ca_{1-x}Cu_{3+x}Ti₄O₁₂ type solid solutions existed in the solubility limit of $-0.0191 \leq x \leq 0.0476$ although the lattice parameter variation in the solid solution region was negligibly small.

Finally, we have fabricated single-layered polycrystalline CCTO (~ 500 nm) films under various deposition temperatures ranging from 700 to 800°C on platinized Si substrates by PLD. Then, we have systemically investigated the relationship among microstructures, compositional distributions, and dielectric properties. In addition, we have synthesized multi-layered polycrystalline and epitaxial CCTO films on platinized Si and single crystal STO substrates, respectively, for improving the $\tan\delta$ and leakage current properties of single-layered CCTO films. With increasing the deposition temperature from 700 to 750°C, the ϵ_r values in single-layered CCTO films were greatly enhanced from ~ 300 to $\sim 2,000$ at 10 kHz, respectively. However, the ϵ_r values were gradually decreased above 750°C, which was surely attributable to the formation of a TiO₂-rich dead layer at the interface

between CCTO and Pt electrode. The leakage current behaviors of the single-layered films were in good agreement with PF conduction model. The TiO₂-rich dead layer and rutile TiO₂ nanocrystalline particles are considered to play a role of charge trapping centers.

The high $\tan\delta$ value over ~ 0.1 at 1 kHz in the single-layered CCTO film was remarkably decreased to ~ 0.05 and ~ 0.04 in the multi-layered polycrystalline CCTO films of Pt/CTO/CCTO and Pt/CTO/CCTO/CTO, respectively. Furthermore, all the multi-layered films showed much lower leakage current compared to that of single-layered film. However, severe drop in ϵ_r values were observable in the multi-layered films. With increasing the thickness of Pt/CTO/CCTO film, the ϵ_r values at 1 kHz in both the single and multi-layered films were also increased from ~ 280 to $\sim 7,400$ and from ~ 640 to $\sim 3,800$, respectively. The $\tan\delta$ values of ~ 0.05 in the Pt/CTO/CCTO film were almost unaltered within the measuring frequency region between 10^2 to 10^6 Hz but the values were abruptly increased to ~ 1 at ~ 100 kHz with further increasing the thickness up to $\sim 1.2 \mu\text{m}$. The leakage current in the multi-layered films was much lower than those of single-layered film since the trap ionization energies of the multi-layered films were relatively higher than that of single-layered film. We fabricated single and multi-layered epitaxial CCTO films with CTO buffer layer and investigated the dielectric properties by increasing the CCTO thickness from ~ 100 to 700 nm on STO (001) substrates with SRO bottom electrode. All samples showed a perfect c -axis orientation but unidentified impurity phase was observable in the multi-layered films. The ϵ_r values in all samples were unaltered with increasing film thickness and no remarkable decrease in $\tan\delta$ values was observable in

the multi-layered films, which are attributable to the presence of large amount of pin holes on the CCTO film surface.

Publications

Paper (SCI journals)

1. S. Y. Lee, Y. W. Hong, and S. I. Yoo, "Dielectric properties of $\text{CaCu}_3\text{Ti}_4\text{O}_{12}$ polycrystalline ceramics", *Electron. Mater. Lett.*, 7, 287 (2011)
2. S. Y. Lee, D. K. Yoo, and S. I. Yoo, "Microstructures and Dielectric Properties of Cu-deficient and excess $\text{CaCu}_3\text{Ti}_4\text{O}_{12}$ Polycrystalline Ceramics", *Electron. Mater. Lett.*, 3, 23 (2007)
3. S. Y. Lee, Y. H. Kim, K. J. Choi, S. M. Jung, and S. I. Yoo, "Effect of copper oxide segregation on the dielectric properties of $\text{CaCu}_3\text{Ti}_4\text{O}_{12}$ thin films fabricated by pulsed laser deposition" *Thin Solid Film.*, 5, 5711 (2010)
4. S. Y. Lee, S. M. Choi, M. Y. Kim, J. H. Lee, William Jo, Y. H. Kim, K. J. Choi, and S. I. Yoo, "Microstructures and electrical properties of $\text{CaCu}_3\text{Ti}_4\text{O}_{12}$ thin films on $\text{Pt/TiO}_2/\text{SiO}_2/\text{Si}$ substrates by pulsed laser deposition" *J. Mater. Res.*, 26, 2543 (2011)
5. S. Y. Lee, D. K. Yoo, S. I. Yoo, J. H. Lee, William Jo, Y. W. Hong, Y. H. Kim, and K. J. Choi, "Colossal dielectric responses of $(\text{Ca}_{1-x}\text{Sr}_x)\text{Cu}_3\text{Ti}_4\text{O}_{12}$ ($0 \leq x \leq 1$) ceramics" (will be submitted)
6. S. Y. Lee, and S. I. Yoo, "The subsolidus phase diagram of SrO-CuO-TiO_2 ternary system" (will be submitted)
7. S. Y. Lee, and S. I. Yoo, "The subsolidus phase diagram of CaO-CuO-TiO_2 ternary system" (will be submitted)

8. S. Y. Lee, J. H. Lee, William Jo, Y. H. Kim, K. J. Choi, and S. I. Yoo, “Highly improved dielectric properties of $\text{CaCu}_3\text{Ti}_4\text{O}_{12}$ films with CaTiO_3 inter-layer on $\text{Pt}/\text{TiO}_2/\text{SiO}_2/\text{Si}$ substrates by pulsed laser deposition” (will be submitted)
9. S. Y. Lee, N. R. Lee, William Jo, and S. I. Yoo, “Surface potential and local current mapping in colossal dielectric $\text{CaCu}_3\text{Ti}_4\text{O}_{12}$ thin-films combined with highly insulating CaTiO_3 layers” (will be submitted)
10. S. Y. Lee, S. D. Yang, and S. I. Yoo, “Primary phase field of $\text{CaCu}_3\text{Ti}_4\text{O}_{12}$ in the CaO-CuO-TiO_2 ternary system” (will be submitted)

Contributed papers (SCI journal)

11. K. P. Ko, R. K. Ko, S. Y. Lee, H. K. Kim, S. H. Moon, S. S. Oh, and S. I. Yoo, “ $\text{GdBa}_2\text{Cu}_3\text{O}_{7-\delta}$ Coated Conductor on BaZrO_3 -Buffered IBAD-MgO Template” *IEEE TRANSACTION ON APPLIED SUPERCONDUCTIVITY.*, 19, 3427, (2009)
12. Y. M. Kang, A. N. Ulyanov, G. M. Shin, S. Y. Lee, D. G. Yoo, and S. I. Yoo, “Magnetotransport properties of c -axis oriented $\text{La}_{0.7}\text{Sr}_{0.3}\text{MnO}_3$ thin films on MgO-buffered SiO_2/Si substrates” *J. Appl. Phys.*, 105, 07D711 (2009)

Patents

1. Y. M. Kim, G. M. Shin, S. Y. Lee, and S. I. Yoo, “Sintered material for dielectric substance and process for preparing the same” *USA*, 12/617122 (2009)
2. Y. M. Kim, G. M. Shin, S. Y. Lee, and S. I. Yoo, “Sintered material for dielectric substance and process for preparing the same” *Europe*, EP09175940.7 (2009)
3. Y. M. Kim, G. M. Shin, S. Y. Lee, and S. I. Yoo, “Sintered material for dielectric substance and process for preparing the same” *Japan*, 2009-259283 (2009)
4. Y. M. Kim, G. M. Shin, S. Y. Lee, and S. I. Yoo, “유전체 제조용 소결 전구체 분말 및 이의 제조 방법”, 대한민국, 10-2009-0013346 (2009)
5. Y. M. Kim, G. M. Shin, S. Y. Lee, and S. I. Yoo, “유전 물질용 소결체 및 이의 제조 방법”, 대한민국, 10-2009-0052239 (2009)

초 록

$\text{CaCu}_3\text{Ti}_4\text{O}_{12}$ (CCTO) 세라믹스는 100~600K 의 광범위한 온도 범위에서 상대유전율이 (relative dielectric constant: ϵ_r) ~10,000을 넘는 초거대유전현상을 보임에 따라 크게 주목 받고 있다. 하지만 CCTO 세라믹스와 단결정(single crystal)에서 보이는 초거대유전현상의 원인은 아직까지 밝혀지지 않고 있다. 또한 CCTO의 높은 유전 손실(dielectric loss: $\tan\delta$)과 누설전류(leakage current) 및 낮은 파괴전압(breakdown voltage)은 커패시터 산업의 응용을 위해 반드시 개선되어야한다. 따라서 본 학위논문에서는 CCTO 세라믹스와 단결정에서 나타나는 초거대유전현상의 원인을 규명하고 CCTO 세라믹스의 높은 유전 손실 및 누설전류를 개선하기 위하여 $(\text{Ca}_{1-x}\text{Sr}_x)\text{Cu}_3\text{Ti}_4\text{O}_{12}$ ($\text{C}_{1-x}\text{S}_x\text{CTO}$, $0 \leq x \leq 1$) 세라믹스를 제조하여 그 유전 특성을 체계적으로 논의하였다. 또한 아직까지 문헌에 보고되지 않은 $\text{SrCu}_3\text{Ti}_4\text{O}_{12}$ (SCTO) 및 CCTO 세라믹스의 고용체의(solid solution) 존재 유무를 규명하기 위하여 SrO-CuO-TiO_2 및 CaO-CuO-TiO_2 삼성분계의 상평형에 대한 연구를 950°C 상압에서 체계적으로 실시하였다. 마지막으로 박막 소자로의 응용을 위하여 다결정 CCTO 박막 및 에피택시 CCTO 박막을 각각 Pt가 코팅된 실리콘 기판과 SrTiO_3 (STO) 단결정 기판위에 펄스레이저 증착법(pulsed laser deposition)으로 제조하여 공정변수에 따른 박막의 미세구조, 조성 및 유전 특성 변화를 다양한 분석법을 통하여 관찰하였다. 다결정 CCTO 박막의 높은 유전 손실과 누설전류 특성을 개선하기 위하여 CaTiO_3 (CTO) 버퍼층을 이용하여 다층박막 구조의 다결정 박막 및

에피택시 CCTO 박막을 제조하여 전기적 특성을 평가하였다. 본 연구의 주요 결과들은 다음과 같다.

첫째, CCTO 세라믹스의 상대유전율은 1 kHz 에서 소결조건과 미세구조에 크게 영향을 받는 것으로 밝혀졌다. 즉 12 h 의 고정된 소결 시간에서 소결온도가 980°C 에서 1000°C 로 증가함에 따라 상대유전율은 ~3,000 에서 ~170,000으로 크게 증가하고 동시에 결정립들의 평균 사이즈역시 ~5 μm 에서 ~300 μm 으로 증가하였다. 하지만 소결온도가 1080°C로 증가하면 상대유전율이 ~69,000으로 감소하고 결정립들의 평균사이즈 역시 ~150 μm 으로 감소하였다. 반면 980°C 에서 소결된 CCTO 세라믹스의 상대유전율은 소결시간을 24h까지 증가시켜도 ~4,000 이하의 값을 나타내며 초거대 유전상수는 1000°C 이상의 소결온도에서 특정 소결 시간 이상에서만 발생하는 비정상 입자 성장이 일어난 경우에만 관찰되었다. 복소 임피던스(Z^*) 및 모듈러스(M^*) 분광학을 통해 CCTO 세라믹스의 상대유전율은 입계의 정전용량(C_{gb}) 값에 크게 영향을 받는 것을 확인하였다. 이에 반해 CCTO 단결정의 상대유전율은 전극의 종류에 따라 크게 영향을 받는 것을 확인하였다. 실버전극의 경우 CCTO 단결정과 전극계면에 발생하는 접촉저항(contact resistance)은 약 80k Ω 임을 알 수 있었고 이는 골드(Au) 및 인듐-갈륨 합금 전극 (InGa) 이 나타내는 접촉 저항보다 월등히 큼을 확인할 수 있었다. 결과적으로 CCTO 세라믹스와 단결정에서 보이는 초거대 유전 현상의 발현기구는 각각 다른 것을 알 수 있었고 높은 입계 정전용량 및 접촉 저항이 CCTO 세라믹스와 단결정의 높은 유전 상수의 원인으로 각각 밝혀졌다.

둘째, Ca^{2+} 이온 자리에 치환된 Sr^{2+} 이온의 양이 증가할수록 $\text{C}_{1-x}\text{S}_x\text{CTO}$ ($0 \leq x \leq 1$) 세라믹스가 보이는 구조적 특성 변화 및 전기적 특성 변화를 체계적으로 분석하였다. 모든 시편에서 비정상적으로 성장된 결정립들을 관찰 할 수 있었고 1 kHz 의 주파수에서 ~40,000이 넘는 초거대 유전 상수를 가지는 것을 확인하였다. 즉 각각의 시편의 1 kHz 에서의 상대유전율은 Sr^{2+} 이온의 치환량이 증가함에 따라 ~120,000 (CCTO) 에서 ~50,000 ($\text{C}_{0.6}\text{S}_{0.4}\text{CTO}$ 및 $\text{C}_{0.4}\text{S}_{0.6}\text{CTO}$)으로 감소하고 다시 ~170,000 (SCTO) 으로 증가하였다. 각 시편의 평균 결정립 사이즈 변화양상도 상대유전율과 같이 CCTO를 기준으로 Sr^{2+} 이온의 치환량이 증가함에 따라 점차 감소하다가 $\text{C}_{0.6}\text{S}_{0.4}\text{CTO}$ 부터 점진적으로 증가하였으며 결국 SCTO 시편은 CCTO에 비해 월등히 큰 결정립 크기를 보였다. 복소 임피던스 및 모듈러스 분광학을 통해 각 시편의 입계 정전용량 변화 양상 역시 상대유전율과 평균 결정립 사이즈의 변화 양상과 정확히 일치하는 것을 확인하였다. 하지만 결정립의 정전용량 (C_g)은 Sr 의 치환량에 상관없이 일정한 값을 보이는 것을 확인하였다. 이는 $\text{C}_{1-x}\text{S}_x\text{CTO}$ ($0 \leq x \leq 1$) 세라믹스가 보이는 초거대 유전현상이 각 시편의 높은 입계 정전용량에서 기인된 결과라 사료된다. 비록 X-선 회절분석 (XRD)을 통해 각 시편의 격자상수는 Sr^{2+} 이온의 치환량이 증가할수록 $0 \leq x \leq 1$ 인 구간에서 직선적으로 증가하는 경향이 관찰되었지만 $x > 0.8$ 인 구간에서는 STO 및 CuO으로 추정되는 이차상이 나타나기 시작하였고 이는 Sr^{2+} 이온의 고용한계는 $x=0.6$ 과 $x=0.8$ 인 조성 사이에 존재하는 것을 보여주는 결과이다.

셋째, SrO-CuO-TiO_2 및 CaO-CuO-TiO_2 삼성분계의 상평형 연구를 950°C 상압에서 실시하였고 이를 통하여 이차상이 존재하지 않는

순수한 SCTO 화합물을 성공적으로 제조할 수 있었다. 또한 아직 문헌에 보고된 적이 없는 SCTO 및 CCTO의 고용 영역(solubility limit)을 체계적으로 규명할 수 있었다. 우선 SrO-CuO-TiO₂ 삼성분계에서 단일상의 SCTO 화합물을 Sr_{1-x}Cu_{3+x}Ti₄O₁₂ (x=0.036)의 조성에서 최초로 합성할 수 있었고 Sr_{0.9639(1-y)}Cu_{3.0361(1-3y)}Ti_{4+2y}O₁₂ 형태의 새로운 고용체가 0≤y≤0.0235의 고용 영역에서 존재함을 성공적으로 규명하였다. 고용영역에 존재하는 화합물들은 모두 비정상 성장된 결정립들로 구성되었고 상대유전율은 1 kHz에서 모두 ~70,000 이상의 값을 나타내었다. 하지만 고용영역에 존재하는 화합물들의 격자상수는 큰 변화없이 일정하게 유지되는 것이 관찰되었는데 이는 고용역역의 범위가 매우 작은데서 오는 것으로 판단된다. CaO-CuO-TiO₂ 삼성분계에선 Ca_{1-x}Cu_{3+x}Ti₄O₁₂ (-0.0191≤x≤0.0476) 형태의 고용체가 존재하는 것을 최초로 규명하였다. 한편 기 출판된 다양한 연구보고에 의하면 CCTO 세라믹스의 결정립이 1000°C 이상의 소결온도에서 비정상 입자 성장을 하는 것을 자주 관찰할 수 있는데 이는 소결시 발생한 CuO 액상에 의해 기인된 결과라 사료된다. 따라서 Ca_{1-x}Cu_{3+x}Ti₄O₁₂ (-0.0191≤x≤0.0476) 고용체를 본 연구의 CCTO 세라믹스의 소결온도와 유사한 1050°C 에서 24 h 열처리 한 뒤 분말 X-선 회절법을 통하여 상분석을 실시하였다. 하지만 고용영역 전반에 걸쳐 단일상으로 구성된 X-선 회절패턴을 확인하였고 CuO와 연관된 불순물이라 판단되는 이차상은 관찰되지 않았다. 따라서 CCTO 세라믹스의 비정상 입자 성장은 소결과정시 발생하는 CuO와 연관된 액상에 기인된 액상소결의 결과라 사료되며 CuO와 TiO₂상 사이에 존재하는 공정온도(eutectic temperature)인 1020°C 이상에서

주로 발생하는 것으로 판단된다.

마지막으로 Pt가 코팅된 실리콘 기판 위에서 700~800°C 의 다양한 증착온도가 다결정 CCTO 박막의 미세구조, 조성 및 유전특성에 미치는 영향을 체계적으로 규명하였다. 또한 CTO 층을 이용한 다층 박막 구조를 통하여 다결정 CCTO 박막의 높은 유전 손실 및 누설 전류를 획기적으로 감소시킬 수 있었다. 우선 다결정 CCTO 박막은 증착온도가 700°C 에서 750°C로 증가함에 따라 1 kHz 에서의 상대유전율도 ~300 에서 ~2,000으로 증가한다. 하지만 750°C 이상의 증착온도에서는 상대유전율이 급격히 감소하는데 이는 CCTO 박막과 Pt 하부전극의 계면에서 발생한 TiO₂ 층에 의한 결과라 사료된다. AES(Auger electron spectroscopy), EDS(Energy dispersive spectroscopy), 및 EELS(electron energy loss spectroscopy) 분석을 통하여 다결정 CCTO 박막에서 Pt 하부 전극으로 Cu 확산 현상이 발생한 것을 확인하였고 증착 온도가 높아질수록 확산되는 Cu 양은 증가하였다. 이를 통해 CCTO 박막과 Pt 하부 계면에 존재하는 TiO₂ 층의 두께는 750°C 이상의 증착온도에서 급격히 증가하고 이는 상대유전율의 심각한 감소 원인으로 판단된다. 다결정 CCTO 박막은 증착온도에 상관없이 모두 PF conduction 거동을 보이며 앞서 언급한 TiO₂ 층과 결정립계에 존재하는 나노 사이즈의 TiO₂ 석출들이 CCTO 박막 내부에서 전하이동을 막는 역할을 하는 것으로 사료된다. 단일층의 다결정 CCTO (500nm) 박막의 높은 유전 손실 및 누설전류 특성을 개선하기 위하여 60nm 두께의 CTO 버퍼층을 CCTO 박막과 Pt 하부전극 사이에 삽입하여 Pt/CTO-60nm/CCTO-500nm, Pt/CCTO-500nm/CTO-60nm, 및 Pt/CTO-60nm/CCTO-500nm/CTO-60nm 구조의 다층 박막을 제조하고 그 유전

특성을 평가하였다. 단일층의 CCTO 박막이 1 kHz 에서 ~ 0.1 이 넘는 유전손실 값을 보이는데 반하여 Pt/CCTO/CCTO 및 Pt/CCTO/CCTO/CTO 구조의 다층 박막은 같은 주파수에서 각각 ~ 0.05 and ~ 0.04 의 우수한 유전손실 특성을 나타내는 것을 확인하였다. 이는 Pt 하부전극에서 CCTO 박막을 통해 이동하는 전하의 움직임이 CTO 박막에 의해 방해를 받는 정도를 나타낼 수 있는 포획 이온화 에너지 (trap ionization energy)의 증가에 기인하는 것으로 사료된다. 하지만 모든 구조의 다층 박막에서 단일층의 CCTO 박막 ($\epsilon_r \sim 2,000$ at 1 kHz) 에 비하여 다소 낮은 상대유전율 ($\epsilon_r \sim 1,150$ in Pt/CCTO/CCTO, $\sim 1,020$ in Pt/CCTO/CTO, and ~ 750 in Pt/CCTO/CCTO/CTO)이 관찰되었다. 단일층 및 다층 박막 구조의 Pt/CCTO/CCTO 박막에서 CCTO 박막의 두께를 ~ 200 nm 에서 $\sim 1.2 \mu\text{m}$ 까지 증가시킨 결과 1 kHz 의 상대유전율은 각각 ~ 280 에서 $\sim 7,400$, ~ 640 에서 $\sim 3,800$ 으로 증가하는 것을 확인하였고 모든 다층 박막 샘플은 0.1 이하 (at 1 kHz) 의 우수한 유전손실 값을 가지는 것을 확인하였다. 하지만 단일층 및 다층 박막 구조의 에피택시 CCTO 박막은 두께가 증가함에 따라 상대 유전율 값이 증가하지 않는 것을 알 수 있었고 CTO층의 존재 유무에 상관없이 다결정 박막에 비하여 상대적으로 높은 유전 손실 값을 보이는 것이 확인되었다. 이는 CCTO 박막과 SRO 하부 전극 사이의 큰 격자 불일치도에 의해 CCTO 박막 표면에 많은 양의 핀홀(pin hole)들이 생성된 것에 의한 것으로 사료된다. 따라서 보다 다양한 버퍼층을 통해 에피택시 CCTO 박막의 유전 특성을 향상시킬 수 있는 추가적인 연구가 필요할 것이다.

주요어: $\text{CaCu}_3\text{Ti}_4\text{O}_{12}$ (CCTO), 초거대 유전 현상, 상대유전율, 유전손실, 누설전류, 비정상 입자 성장, 복소 임피던스 및 모듈러스 분광학, $(\text{Ca}_{1-x}\text{Sr}_x)\text{Cu}_3\text{Ti}_4\text{O}_{12}$ ($0 \leq x \leq 1$) 세라믹스, 상평형, 펄스레이저 증착법, Cu 확산, 다결정 및 에피택시 CCTO 박막, 단일층 및 다층 CCTO 박막, 버퍼층, CaTiO_3 (CTO), SrRuO_3 (SRO), SrTiO_3 (STO)

학 번 : 2006-20868